STRUT-AND-TIE MODELLING OF DEEP BEAMS

ZHANG NING

SCHOOL OF CIVIL AND ENVIROMENTAL ENGINEERING

2009

STRUT-AND-TIE MODELLING OF DEEP BEAMS

ZHANG NING

School of Civil and Environmental Engineering

A thesis submitted to the Nanyang Technological University
in fulfillment of the requirement for the degree of
Doctor of Philosophy

2009

ACKNOWLEDGEMENTS

The work described in this thesis was carried out in the school of civil & environmental engineering, Nanyang Technological University.

The author wishes to express his deepest gratitude and appreciation to Associate Professor Tan Kang Hai, Deputy Director of Protective Technology Research Centre, the author's supervisor, for his warm encouragement, constant guidance and valuable advice during the study. In addition, he was always accessible and willing to help his students with their research. As a result, research life became smooth and rewarding for me. It is the author's honour and pleasure to work with him.

The author would also like to acknowledge the technical staff from the Construction Technology Lab, in particular, Mr. Tui Cheng Hoon, Mr. Chelladurai Subasanran and Ms. Wee-Woo May Sim for their assistance in the course of the experimental work.

Special thanks are given to the author's wife Dr. Sheng Xiaoxia for her lovely company and helpful suggestions during the course of my study. The author also wishes to express his utmost gratitude to his parents for their unflagging love, support and encouragement during the study.

Finally, the author is grateful to the University for providing the research scholarship.

TABLE OF CONTENTS

SUMMARY

A modified strut-and-tie model (STM) for RC simply supported deep beams (SSDBs) was proposed. Several significant improvements were made to the original model (Tan et al. 2001) and gave rise to better prediction performance. The influence of stress distribution factor *k* on the model prediction was studied. It was shown the *k* value derived from linear stress assumption was sufficiently accurate for predicting the ultimate beam strength. The use of the interactive failure criterion (Kupfer's failure equation) implied that no empirical stress limit was required for calculating the beam shear strength, and that the softening effect of concrete compressive strength due to transverse tensile strain was taken into consideration. The softening effect was comparable to MCFT (1986) and Belarbi and Hsu's (1994) equations. The modified STM for SSDBs was evaluated by 233 test results from literature and exhibited better agreement than ACI 318-99 shear provisions and the original model (Tan et al. 2001). The STM was further extended to RC continuous deep beams (CDBs) validated by 54 experimental results.

The effects of differential support settlement on the strength and behaviour of CDBs was investigated through an experimental programme of 6 specimens and the proposed Strut-and-Tie Model. The influence of support settlement on deep beam behaviour was studied. The middle support settlement significantly affected the serviceability load, crack pattern and failure mode. However, the specimens exhibited considerable capacity in accommodating the effects of differential support settlement in terms of ultimate load, particularly for those beams with web reinforcement. The modified STM was developed further to calculate the ultimate strengths of deep beams subjected to support settlement. Good agreement was found between the test results and STM predictions on support reactions and ultimate loads. The proposed

STM was very accurate in the prediction of failure zones of tested specimens.

Fourteen specimens were tested to investigate the effects of asymmetrical loadings on SSDBs. Conclusions were drawn on the effects of Load Inequality (LI) and Load Asymmetry (LA) on deep beam behaviour. The ACI 318-05 Strut-and-Tie method was found to slightly overestimate the beam shear capacity. The author extended the STM further to include asymmetrically-loaded deep beams. A load parameter Π was introduced such that the proposed STM can simulate both the effects of LI and LA. The extended STM was a generalized form for SSDBs. It contained both single-point and two-point symmetric load conditions. The method was also used to predict the failure modes of tested deep beams, and the results were promising.

Deep beams behave very differently from shallow beams as arch action rather than flexure dominates the behaviour after diagonal cracking has occurred. It was postulated that the factors influencing the strength of a compression member, i.e. the strut geometry and boundary conditions, governed the size effect. The modified STM was accordingly derived incorporating the causes of size effect. To verify the model, a test programme of 11 geometrically-similar specimens was conducted. By properly configuring the loading and support plate dimensions, size effect in ultimate shear strength was significantly mitigated, even for beams with high h/b ratios and plain concrete web. The experimental programme provided experimental evidence to the hypotheses from strut-and-tie models. Effects of out-of-plane actions on beam strength were also investigated and discussed. The proposed STM outperformed several other methods in predicting the ultimate shear strengths.

The STM proposed in this work can be easily implemented through excel spreadsheet, thus making it an attractive tool for engineers.

LIST OF FIGURES

LIST OF TABLES

LIST OF SYMBOLS

a, c	Left and right shear span, measured between concentrated load and the support, respectively,
A_c	Beam effective cross-sectional area, equals to $b_w d_c$
A_s	Area of bottom longitudinal reinforcement
A_{s1}, A_{s2}	Area of top and bottom longitudinal reinforcement, respectively
A_{str}	Cross-sectional area of the concrete diagonal strut at nodal zone
A_{str1}, A_{str2}, A_{str3}	Cross-sectional areas of the concrete diagonal struts at node A, B, C, respectively
A_{str3}, A_{str4}	Average cross-sectional areas of the exterior and interior concrete struts, respectively
A_{sw}	Total area of web reinforcement that criss-crosses the diagonal strut
A_{sw1}	Area of single web steel bar that criss-crosses the diagonal strut
A_{sh}, A_{sv}	Total areas of vertical and horizontal steel reinforcement that criss-cross the strut, respectively
b	Horizontal distance between the two top loads
b_w	Width of the RC deep beam
c_1, c_2	Distances from the centroid of the top and bottom longitudinal steel to the beam top and beam soffit, respectively
d_1	Distance from beam top to the centroid of nodal zone A
d_2	Distance from beam top to the centroid of nodal zone B
d_3	Distance from beam soffit to the centroid of bottom longitudinal

	reinforcement
d_c	Distance from the centroid of the bottom longitudinal reinforcement to the centroid of the top nodal zone A
d_w	Distance from the beam top to the intersection of web reinforcement with the line connecting the support centre and the load centre.
E_c, E_s	Elastic modulus of concrete and steel, respectively
f_1, f_2	Principal tensile and compressive stresses, respectively
f_c'	Concrete compressive strength
f_{ct}	Tensile contribution of concrete to the composite tensile capacity
f_{st}	Tensile contribution of reinforcement to the composite tensile capacity
f_t	Combined tensile strength of reinforcement and concrete
f_y	Yield strength of bottom longitudinal reinforcement
f_{y1}, f_{y2}	Yield strength of top and bottom longitudinal reinforcement, respectively
f_{yh}, f_{yv}	Yield strength of horizontal and vertical web reinforcement, respectively
f_{yw}	Yield strength of web reinforcement
F_c	Compressive force in the diagonal strut of a SSDB
F_{c1}, F_{c2}	Compressive force in the exterior and interior diagonal strut of a CDB,
h	Overall height of deep beam

h_e	Width of top concrete strut
k	Stress distribution factor at the bottom nodal zone
k'	Stress distribution factor at top nodal zone
l, s	Length and width of the diagonal strut
l_0	Effective beam span, taken as the distance between the centres of two supports
l_a, l_b, l_f	Widths of the load bearing, end support and middle support plates, respectively
l_c, l_d	Effective depths of the bottom and top nodal zones, respectively
m_L	Load asymmetry index, equals to c/a
n_L	Load inequality index, equals to P_1/P_2
m, n, p	Ratios of axial stiffness of truss members in STM
n_s	Nos. of web steel bars evenly distributed along the strut
p_t	Average equivalent tensile stress across the diagonal strut
P	Load applied on the CDBs
P_1, P_2	Left and right loads acting on the beam top, respectively
P_exp	Experimental ultimate load of CDBs
P_n	Predicted ultimate load of CDBs
T	Tensile force in the reinforcement
T_1, T_2	Tension force in the top and bottom steel, respectively
$T_{1\mathrm{max}}$, $T_{2\mathrm{max}}$	Yield strength of top and bottom steel, respectively
$T_{1\mathrm{a}}$, $T_{2\mathrm{a}}$	Corresponding tension force in the top and bottom steel at the

	yielding of bottom and top steel, respectively. They are limited by the respective top and bottom steel yield strength.
U_c	Total complementary energy in the truss
V_{exp}	Experimental shear strength of SSDBs
V_1, V_2	Reaction force of the left and right supports, respectively
V_n	Predicted shear strength of SSDBs
α, β	Inclination angles of left and right diagonal struts, respectively
Δ	Vertical distance between the two ends of the centre line of the top strut, negative when the top strut inclines anticlockwise
v	Concrete softening coefficient
X	Reaction force of the middle support of CDBs
ε_1, ε_2	Principal tensile and compressive stress at the tension-compression nodal zone, respectively
ε_s	The strain in the reinforcement
θ	Inclination angle of top strut of the STM, clockwise is positive
θ_w	Angle between the web reinforcement and the horizontal axis of beams at the intersection of the reinforcement and the diagonal strut
θ_s	Angle between the longitudinal tension reinforcement and the diagonal Strut
ρ_a	Total reinforcement ratio of beams, equal to $(A_{s1}+A_{s2})/A_c$
ρ_s	Effective longitudinal reinforcement ratio of the beam, equal to A_s/A_c.

CHAPTER 1 INTRODUCTION

In engineering practice, nearly all reinforced concrete members have to be designed to resist shearing forces. Although shearing forces rarely exist alone and often act in combination with other forces including axial load, bending and torsion, if not properly considered, they may lead to engineering accidents due to the abrupt nature of shear failure. On the other hand, some commonly used structural members do experience predominantly shearing forces. In members such as deep beams, corbels, beam-column joints, shear walls, pile caps, etc, shear failure usually dominates design. Owing to above reasons, researchers have been investigating the behaviour of structural concrete subjected non-flexural actions for a long time. The collapse of the Wilkins Air Force Depot warehouse in Shelby, Ohio (1955) caused by the brittle shear failure of deep beams, further attached importance to extensive research works on shear behaviour of structural concrete.

However, due to the complicated shear mechanisms, researchers had proposed various complex models and come up with various complex empirical equations for shear design. Not only are the applications of these equations complex in themselves, but the prediction accuracy is less than desirable.

1.1 Shear in Structural Concrete

The 1973 ASCE-ACI Committee 426 Report identified the following four mechanisms of shear transfer: shear stresses in uncracked concrete; interface shear transfer, often called “aggregate interlock” or “crack friction”; the dowel action of the longitudinal reinforcing bars; and arch action. The 1998 ASCE-ACI Committee 445 Report highlighted a new mechanism consisting of residual tensile stresses, which are transmitted directly across cracks. Opinions vary about the importance of each mechanism in the total shear resistance mechanism, resulting in different models for members without transverse reinforcement.

The shear stresses in uncracked concrete are not a very important mechanism for slender beams because arch action is not effectively established in the member. Dowel action is not very significant as the maximum shear in a dowel is limited by the tensile strength of the concrete cover supporting the dowel. On the other hand, at locations of maximum moment for deep beams, much of shear force is resisted in the compression zones, particularly after significant yielding of longitudinal reinforcement has occurred. Shear transfer in the interface was primarily because of ‘aggregate interlock’, and caused by those aggregates that protruded from the cracked surfaces and provided resistance against slip. **Figure 1.1** shows a case where the tension force in the longitudinal reinforcement remains constant but the lever arm Z varies along the length. This occurs if the transfer of shear flow is prevented by an inclined crack extending from the load point to the support. In such a case the shear force is transferred by arch action. The arch action is directly related to the shear span-to-depth a/d ratio. Beams without stirrups and with an a/d ratio of less than 2.5, develop inclined cracks and, after a redistribution of internal forces, are able to carry an additional load due to arch action.

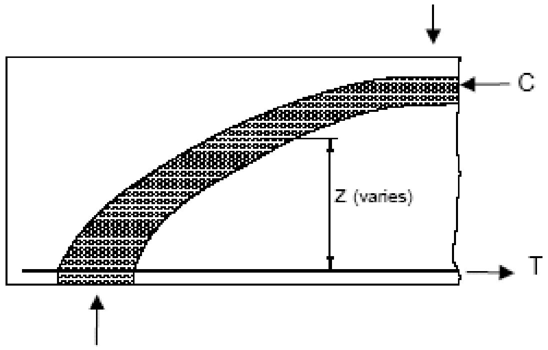

Figure 1.1 Arch action in a beam

As shown in **Figure 1.2**, for these series of beams, tested by Kani (1979), the ultimate shear strength was reduced by a factor of about 6 as the *a*/*d* ratio increased from 1 to 7. As the beams were designed with a large amount of longitudinal reinforcement, flexural failure at mid-span was not critical until a shear span-to-depth ratio of about 7.

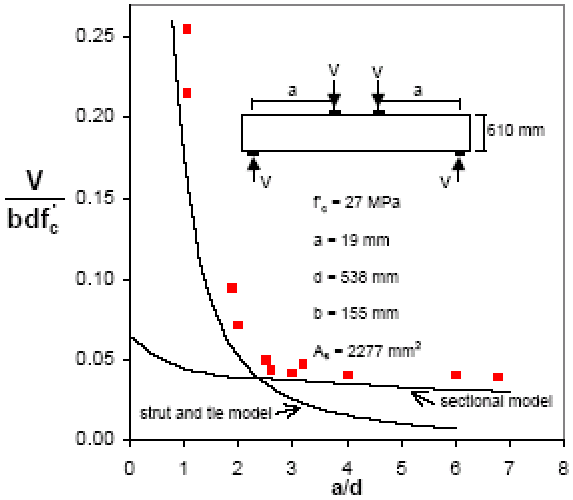

Figure 1.2 Beam shear strength reduces as *a*/*d* ratio increases (Kani, 1979)

1.2 Cracked Reinforced Concrete

After the development of Compression Field Theory (CFT), a large amount of experimental research aimed at determining the stress-strain characteristics of diagonally cracked concrete has been conducted. These works typically involved subjecting reinforced concrete elements to uniform membrane stresses in a special-purpose test rig. A summary of the test results from various studies was given by Vecchio and Collins (1993). These experimental studies provide strong evidence that the ability of diagonally cracked concrete to resist compression decreases as the amount of tensile straining increases. Vecchio and Collins (1986) suggested that the maximum compressive stress, $f_{2\max}$, which the concrete can resist, reduces as the average principal tensile strain, ε_1, increases in the following manner:

$$f_{2\max} = \frac{f_c^{'}}{0.8 + 170\varepsilon_1} \leq f_c^{'} \tag{1.1}$$

Belarbi and Hsu (1995) suggested more complex expressions

$$f_{2\max} = \frac{0.9 f_c^{'}}{\sqrt{1 + 400\varepsilon_1}} \quad \text{(For proportional loading)} \tag{1.2}$$

$$f_{2\max} = \frac{0.9 f_c^{'}}{\sqrt{1 + 250\varepsilon_1}} \quad \text{(For sequential loading)} \tag{1.3}$$

A comparison between various relationships for a reduction in concrete compressive strength was reported by ASCE-ACI Committee 445 (1998). According to which, Eq. (1.1) generally fits well with 73 element test results while Eq. (1.2) gives better predictions for specimens with larger strains up to 4%.

The CFT assumes that after cracking, there will be no tensile stresses in concrete. Realistically this is only true at the location of a crack, where the reinforcement resists all the stresses. In between cracks, the concrete does manage to carry some tensile stresses. This phenomenon was first observed by Considere, who carried out tests on reinforced tension members as early as 1899. It was found that the response curve of a reinforced mortar prism after the cracking load N_{cr} was above and parallel to that of an equivalent bare steel bar (**Figure 1.3**). Both samples were ultimately limited by the yield capacity of steel wire. Thus it was concluded that cracked mortar added stiffness to the embedded reinforcement.

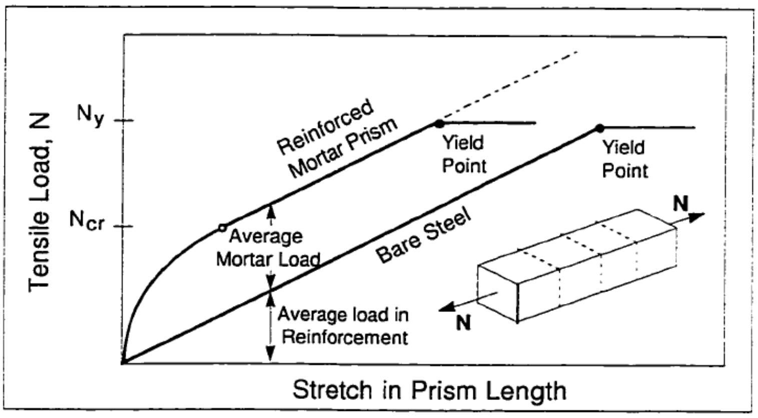

Figure 1.3 Typical tensile load versus stretch in length of a reinforced mortar prism and separate bare steel wire, as tested by Considere, 1899 (Fields, 1998)

Mörsch in 1908 similarly found that the concrete between two adjacent cracks could reduce the tensile strain of embedded steel bars as compared to bare ones. This effect was referred to as tension stiffening and was attributed to bonding between concrete and steel bar. Load sharing of concrete surrounding the reinforcement reduced the average reinforcement stress resulting in a lower overall member extension compared to bare rebars. Tests on reinforced concrete elements demonstrated that tensile stresses existing in the cracked concrete significantly increased the ability of cracked concrete to resist shear stresses. Collins and Mitchell (1991) proposed a relationship between the average principal tensile stress and the average principal tensile strain

$$f_1 = \frac{0.33\sqrt{f_c^{'}}}{1+\sqrt{500\varepsilon_1}} \quad \text{(MPa)} \qquad (1.4)$$

while Belarbi and Hsu (1994) suggested

$$f_1 = 0.31\sqrt{f_c^{'}}\left(\frac{\varepsilon_{cr}}{\varepsilon_1}\right)^{0.4} \text{ (MPa)} \tag{1.5}$$

where ε_{cr} is the strain of concrete at cracking. Eq. (1.5) predicts a faster decay for f_1 with increasing ε_1 when compared with Eq. (1.4).

1.3 Strut-and-Tie Method

Many new design approaches for shear failure have evolved since 1970's, among which the truss model approach seems promising. This methodology is the most effective because it is based on a relatively simple concept rather than on complex empirical equations. In addition, it imparts physical motions to its application. This methodology is also termed the Strut-and-Tie Method (STM). The strut-and-tie method has been improved and validated considerably during the last few decades with increasing availability of experimental results and the development of limit analysis in plasticity theory. However, the idea of STM is not new. The truss analogy method was first introduced by Ritter and Mörsch in the early 1900s for shear design of reinforced concrete beams. The truss model has also been used as the design basis for torsion. The contribution of concrete in tension was neglected for simplicity. Marti (1985) and Schlaich et al. (1987) extended the use of truss model to D-Regions where the strain distribution is significantly nonlinear. This model is justified by the fact that reinforced concrete structures carry loads through compressive stress fields which are criss-crossed by tensile ties. The ties can be reinforcing bars, prestressing tendons, or concrete tensile stress fields. For analytical purpose, the strut and tie models simplify compressive and tensile stresses into compression struts and tension ties, respectively. The intersection region between a compression member (strut) and a tension member (tie) is referred to as the nodal zone or region.

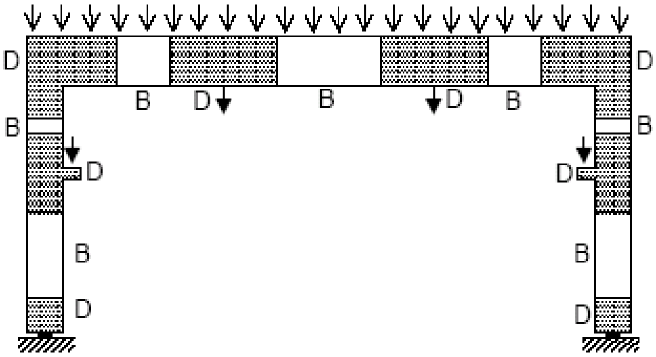

Figure 1.4 B-regions and D-regions (Schlaich et al. 1987)

Figure 1.4 shows the distribution of D and B regions, where D stands for ‘discontinuity’ or ‘disturbed’, and B stands for ‘beam’ or ‘Bernoulli’. In the D regions, the distribution of strain is significantly nonlinear across the section and strut-and-tie models are particularly relevant. In the B regions the strain distribution is linear and the response of concrete member will principally be due to beam action which implies that the lever arm (z) is constant. In the D regions, plane sections before bending are no longer plane after bending. Therefore, the principles of stress analysis used for shallow members are neither suitable nor adequate to determine the strength of D regions. An important characteristic of D regions is their considerably higher shear capacity than is predicted based on shallow beam theory. The greater shear strength of the D regions is due to arch action, which is the mechanism that transfers the load directly to a support through the development of inclined struts. Steel reinforcement acts as ties and, therefore, D regions can be modelled as an analogous truss, or the strut-and-tie method.

The Strut-and-Tie method is based on the lower-bound theory of limit analysis. It involves conceptualising an internal truss, which consists of concrete struts and tension ties connected in the nodal zones; the truss carries the load through the D-Region to its supports or boundaries. It is a rational tool and gives accurate and consistent predictions of the shearing behaviour of the D-Regions in structural concrete. This is of great significance as most structural problems occur in the D-Regions due to the inadequacy of empirical design provisions and detailing practices. D-Regions are those parts of structures in which concentrated forces or geometrical discontinuities induce significant nonlinear strain distribution. Quite a few types of structures, including joints, corbels, deep beams and pile caps, are D-Regions.

The general procedure for calculation of structural concrete using STM is briefly summarised as below:

(i) Determine the imposed loads (location and magnitude) and support conditions of the structure.

(ii) Determine the geometry of STM as well as the dimensions, stiffness and strength characteristics of components (struts and ties).

(iii) Determine the capacity of STM components.

(iv) Solve the truss member forces and check the preset capacity limits of STM components to ensure adequate factor of safety from failure.

(v) Predict the behaviour (failure load, failure mode, location of failure zone etc) of concrete member concerned.

The design procedure is a reverse process of the above steps supplemented with safety factors and the necessary detailing around the joint or nodal regions.

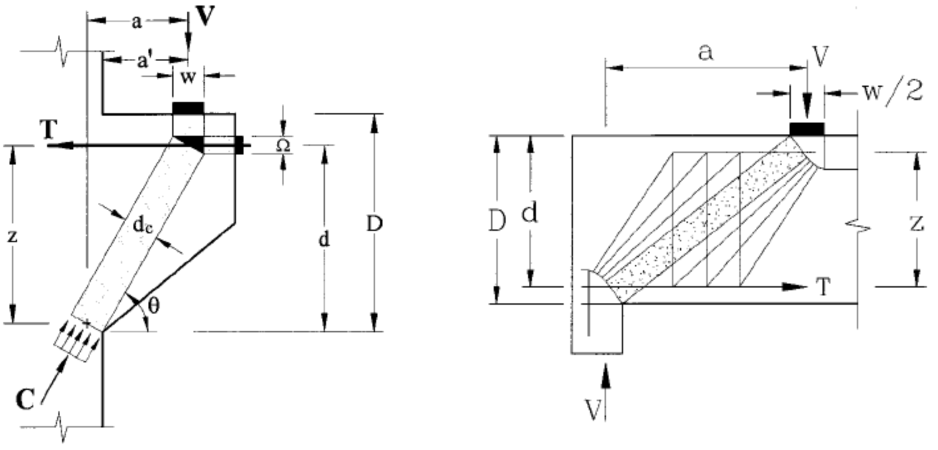

(a) Corbel without stirrups (b) Deep beam with stirrups

Figure 1.5 Plastic truss models (Adapted from Foster and Malik 2002)

Truss models provide an excellent conceptual model for calculating the forces that exist in a cracked concrete member. The 45° Mörsch model can be made more accurate by noting that the angle is typically less than 45° . Modified truss models are used in more recent design codes. For example, the ACI Building Code 318-99 still adds a concrete contribution term to the shear reinforcement capacity obtained, assuming a 45° truss. Nielsen et al. (1978) were among the earliest to propose the plastic truss model for beams and corbels in shear (**Figure 1.5**). In the model, all members enter the nodal zones at 90° and thus the nodes are in a state of hydrostatic compression and do not require checking for shear. There are two possible modes of failure in the plastic truss model, namely, failure by crushing of concrete in the strut and by yielding of ties. Plastic truss model considers steel reinforcement as ties. However, it does not include the failure mode of diagonal splitting of the strut. The basic equations relating to equilibrium and strength for the plastic truss model are given below:

$$T = A_s f_{sy} \tag{1.6}$$

$$C = f_c * bd_c \tag{1.7}$$

$$V = \min(A_s f_{sy} z / a, f_c * bw) \tag{1.8}$$

where A_s is the area of tension reinforcement, f_{sy} is the yield strength of the reinforcement, f_c* is the effective concrete strength and is given by $f_c*=vf_c'$, v is an efficiency factor in the concrete strut. The dimensions are shown in **Figure 1.5**. However, there are other strut-and-tie models. The plastic truss model is still used nowadays because of its simplicity.

Schlaich et al. (1987) suggested that a strut-and-tie model be chosen after performing an elastic analysis. The angles of the compression diagonals should be within ±15° of the resultant of the compressive stresses obtained from an elastic analysis. Hsu and his colleagues from the University of Houston (Belarbi and Hsu 1994, 1995) presented the Rotating-Angle Softened-Truss Model (RA-STM). Like the MCFT, this method assumes that the inclination of the principal stress direction θ, coincides with the principal strain direction. For typical elements, θ will decrease as the shear force is increased, hence the name 'rotating angle'. (Pang and Hsu, 1995) limited the applicability of the rotating-angle model to situations in which the rotating angle does not deviate from the fixed angle by more than 12° . Outside this range they recommend the use of a fixed angle model where it is assumed (Pang and Hsu, 1996) that shear cracks are parallel to the principal direction of compressive stress as defined by the applied loads.

Mau and Hsu (1989) proposed the softened truss model for deep beams extended from the theory for low-rise shear walls. They proposed the following equation for the shear strength of deep beams.

$$\frac{v}{f_c'} = \frac{1}{2}\left[K(\omega_h + 0.03) + \sqrt{K^2(\omega_h + 0.03)^2 + 4(\omega_h + 0.03)(\omega_v + 0.03)}\right] \qquad (1.9)$$

where $\omega_h = \rho_h f_y / f_c' \leq 0.26$ and $\omega_v = \rho_v f_y / f_c' \leq 0.12$; K is a coefficient representing the shear span effect and determined by

$$K = \begin{cases} \dfrac{2d_v}{h} & \text{for } 0 < a/h \leq 0.5 \\ \dfrac{d_v}{h}\left[\dfrac{h}{a}\left(\dfrac{4}{3} - \dfrac{2}{3}\dfrac{a}{h}\right)\right] & \text{for } 0.5 < a/h \leq 2 \\ 0 & \text{for } a/h > 2 \end{cases}$$

The proposed formula Eq. (1.9) is based on the equilibrium conditions of the shear element within a deep beam. The stresses in the theoretical shear element model are assumed to be uniform so that the stresses obtained are the average stresses.

Siao (1993, 1994, and 1995) used a refined strut-and-tie system as advocated by Schlaich et al. to derive the shear capacity of a deep beam (**Figure 1.6**). He later extended the model to include four-pile caps, corbels and squat shear walls.

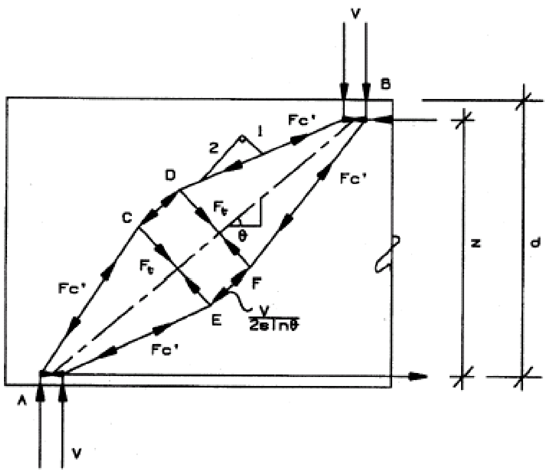

Figure 1.6 Refined model for compression strut (Siao 1995)

Siao proposed in his model using diagonal splitting strength $f_{sp} = 0.52\sqrt{f_{cu}}$. However, the model only accounted for the failure mode of diagonal splitting.

Hwang et al. (2000) proposed a softened strut-and-tie model based on the following assumptions:

1) Stress and strain in the concrete were taken as the average values. Therefore, equations derived from the Mohr's circle of strains and stresses can be used as compatibility equations.

2) All web reinforcement is assumed to be perfectly embedded in concrete so that the steel strains may be assumed to have the same value as the concrete strains in the respective direction, i.e.

$$\varepsilon_s=\varepsilon_h \text{ or } \varepsilon_s=\varepsilon_v$$

3) The angles of inclination of the principal stresses coincide with those of their corresponding strains.

4) Failure is assumed to be caused by the crushing of strut or by the yielding of web reinforcement.

5) The bearing plates are assumed to be adequate such that the beam does not fail in nodal zone. Therefore, the intersection of force path at the nodes is ignored.

Hwang's model adopts three shear resisting mechanisms: diagonal, vertical and horizontal mechanism. The model also adopts softening curve of concrete strut from softened truss model.

In reality, there are a number of uncertainties and complications that can hinder the calculation procedure. These include strut and nodal capacity, geometry of struts and nodal zones and statically indeterminate trusses. Consequently, the designer has little guidance for determining the distributions of loads in statically indeterminate strut-and-tie (truss) models.

While STM is a conceptually simple design tool, common practices of STM nowadays involve assuming different levels of stress limits under different stress conditions on the components. As one can see, the definition of stress limits is of vital importance. There has been considerable debate about the value of the concrete efficiency factor. **Tables 1.1** and **1.2** summarise different stress limits in concrete struts and nodal zones proposed by different researchers. Various limits are placed on the magnitude of allowable stress in the nodal zone and compressive strut. ACI 318 code, CSA concrete code and CEB-FIP Model code (1990) give different values on the stress limits according to their respective investigations.

Another school of researchers (Mau and Hsu 1989, Hwang et al. 2000) relate the stress limits with the transverse strain perpendicular to the stress direction so as to consider the softening effect of concrete compressive strength. However, it may not be appropriate to apply the smeared crack model concept to the D-Region, that is, disturbed region where the conventional plane-section-remains-plane principle is not valid (Schlaich et al., 1987).

Table 1.1 Stress limits in concrete struts

Researcher (1)	Condition of concrete struts (2)	Proposed stress limits (3)
Marti (1985)	all	$0.60f_c'$
Schlaich et al (1987)	Undisturbed and uniaxial state of compressive stress that may exist for prismatic struts	$0.85f_c'$
	Tensile strains and/or reinforcement perpendicular to the axis of the strut may cause cracking parallel to the strut with normal crack width	$0.68f_c'$
	Tensile strains causing skew cracks and/or reinforcement at skew angles to the strut's axis	$0.51f_c'$
	Skew cracks with extraordinary crack width. Skew cracks would be expected if modelling of the struts departs significantly from the theory of elasticity's flow of internal forces	$0.34f_c'$
MacGregor (1988)	Isolated compression struts in deep beams or D-regions	$0.50f_c'$
	Severely cracked webs of slender beams with strut angle of 30°	$0.25f_c'$
	Severely cracked webs of slender beams with strut angle of 45°	$0.45f_c'$
Bergmeister et al (1991)	20 MPa $\le f_c' \le$ 80 MPa	$f_c = (0.5 + \frac{1.25}{\sqrt{f_c'}})f_c'$
Alshegeir (1992)	Moderately confined diagonal struts going directly from point load to support with shear span to depth ratio less than 2.0	$0.85f_c'$
	Struts forming arch mechanism	$0.75f_c'$
	Arch members in prestressed beams and fan compression members	$0.50f_c'$
	Undisturbed and highly stressed compression struts	$0.95f_c'$

Table 1.2 Stress limits in nodal zones

Researcher (1)	**Condition of nodal zones (2)**	**Proposed stress limits (3)**
Schlaich et al (1987)	Compression-compression-compression nodes	$0.85f_c'$
	Nodes where reinforcement is anchored in or crossing the node	$0.68f_c'$
MacGregor (1988)	Nodes bounded by compressive struts and bearing areas	$0.85f_c'$
	Nodes anchoring one tension tie	$0.65f_c'$
	Nodes anchoring tension ties in more than one direction	$0.50f_c'$
Bergmeister et al (1991)	Unconfined nodes without bearing plates	$0.8f_c'$ $(f_c' \leq 27.6$ MPa$)$ $(0.9-0.25f_c'/69)f_c'$ $(27.6 \leq f_c' \leq 69$ MPa$)$ $0.65f_c'$ $(f_c' \geq 69$ MPa$)$
	Unconfined nodes with bearing plates	$(0.5+1.25/\sqrt{f_c'})f_c'(A/A_b)^{0.5}$
	Confined nodes	$(0.5+1.25/\sqrt{f_c'})f_c'(A/A_b)^{0.5}+$ $a(A_{core}/A_b)f_{lat}(1-s/d)^2$
	Triaxially confined nodes	$2.5f_c'$

Note: A, A_b and A_{core}= area of confined concrete, bearing plate and the confined strut, respectively; f_{lat}= lateral pressure $2f_yA_s/ds$ for f_c'<48.3 MPa; $2f_yA_s$/ds for fc'>48.3 MPa; s= spacing of confining reinforcement; d=diameter of confined core; a=4.0 for spiral confinement, 2.0 for square closed hoop confinement anchored with longitudinal reinforcement, and 1.0 for square closed hoop confinement without longitudinal reinforcement anchorage.

Quite a number of tests (Kong et al., 1970, 1972; Smith and Vantsiotis, 1982; Tan et al., 1995, 1997) have demonstrated that web reinforcement, especially inclined ones, greatly enhanced the shear strength of deep beams. However, most of the current strut-and-tie methods have not quantitatively incorporated the beneficial effect of web reinforcement. Tan et al (2001) developed a direct strut-and-tie model for simply supported deep beams, which considers the effect of different web reinforcement configurations (**Figure 1.7**). The model was verified against three case studies of a total of 116 beams (Tan et al 2003a). Tan et al (2001) contended that the effectiveness of web steel is governed by its lever arm to the top loading point; the greater the lever arm, the more effective is the web steel. It was accordingly argued that vertical web steel is more effective in restraining the diagonal crack width than horizontal web steel for deep beams with $a/d \geq 1.0$, and vice versa for deep beams with $a/d < 1.0$.

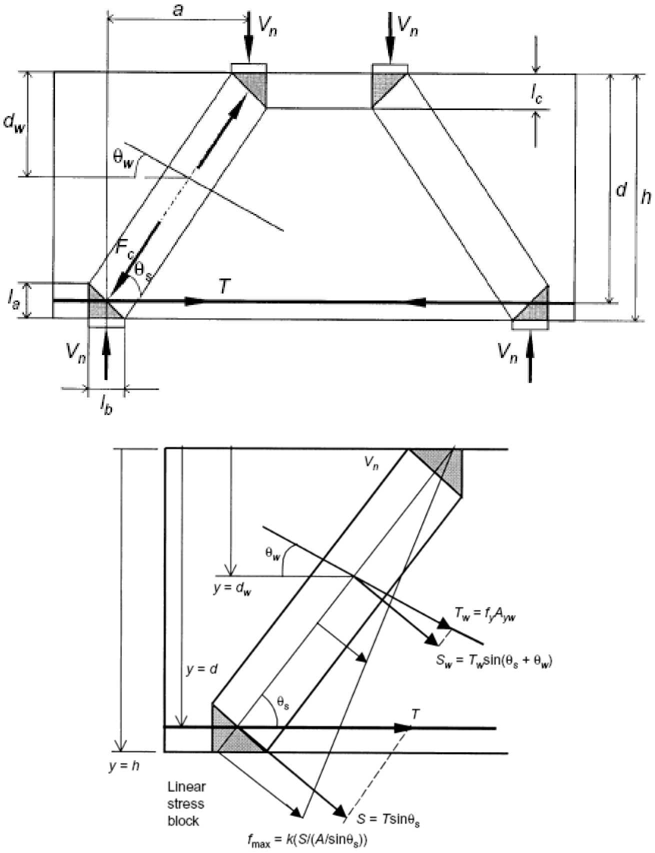

Figure 1.7 STM for Simply Supported Deep Beams (Tan et al 2001)

In the model, Tan et al (2001) used a failure criterion modified from the Mohr-Columb theory for bottom nodal zones (tension-compression stress state) as below:

$$\frac{f_1}{f_t}+\frac{f_2}{f_c'}=1 \tag{1.10}$$

where f_1 and f_2 are principal tensile and compressive stresses at the nodal zone respectively; f_c' is cylinder compressive strength representing the maximum compressive capacity in the f_2 direction; and f_t represents the maximum tensile capacity in the f_1 direction. It is worth noting that the term f_t here is the combined tensile strength comprising contributions from both concrete and reinforcement (web and main). This failure criterion is adopted because it offers a simple linear interactive relationship between two limit failure modes, namely, brittle concrete crushing and ductile reinforcement yielding. The failure criterion also implies a softening effect in the concrete due to transverse tension strain. The author will discuss it in greater detail in Chapter 2.

The principal tensile stress f_1 at the nodal zone is due to component force of longitudinal reinforcement in the direction perpendicular to the diagonal strut, namely, $T\sin\theta_s$. To determine the magnitude of f_1, it was assumed that the tensile stress distribution along the diagonal strut due to $T\sin\theta_s$ is triangular. Thus, f_1 is approximated by

$$f_1 = \frac{kT\sin\theta_s}{A_c/\sin\theta_s} \tag{1.11}$$

where $T\sin\theta_s/(A_c/\sin\theta_s)$ is the average tensile stress across the diagonal strut; and k in the numerator is a factor taking account of the non-uniformity of the stress distribution. Tan et al (2001) proposed $k = 2$ based on the assumption of triangular stress distribution, derived from force equilibrium, namely, by equating $T\sin\theta_s$ to the force represented by the assumed triangular stress block (**Figure 1.7**). Although by adopting $k = 2$ the moment equilibrium is actually not satisfied (it will be discussed in detail in chapter 2), it was argued that the model is not sensitive to the actual values of k. It is difficult to determine the exact magnitude of the principal tensile f_1 as its actual distribution is complicated. Tan and Cheng (2006) utilised the FEM program

WCOMD to simulate the transverse tensile strain along the diagonal strut in the deep beams (**Figure 1.8**). It gave a picture that the stress distribution along diagonal strut was highly nonlinear and an assumption of its distribution was necessary. It was argued (Tan et al. 2001) that the triangular assumption on the stress distribution is reasonable and a *k*-value of 2 yields the best agreement with test results.

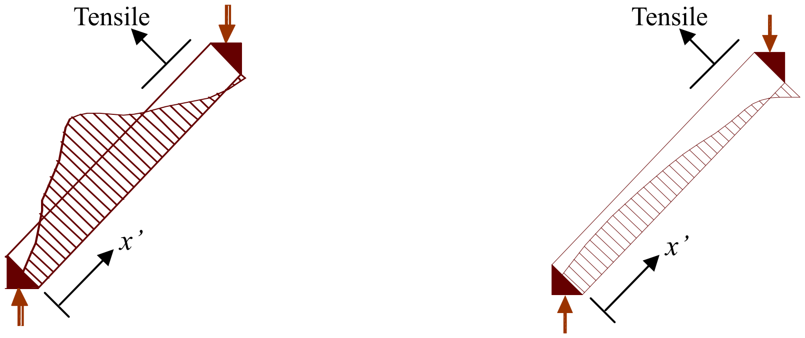

a) without web reinforcement b) with web reinforcement

Figure 1.8 Transverse strain along strut at ultimate state (Tan and Cheng 2006)

The term f_t in Eq. (1.10) was given by

$$f_t = \frac{2A_s f_y \sin\theta_s}{A_c / \sin\theta_s} + \frac{2A_w f_{yw} \sin(\theta_s + \theta_w)}{A_c / \sin\theta_s} \cdot \frac{d_w}{d} + f_{ct} \tag{1.12}$$

The first term in Eq. (1.12) represented the tensile capacity of longitudinal steel and was obtained in a similar fashion as f_1 in Eq. (1.11); the second term represents the tensile capacity of web reinforcement, which inclines at an angle θ_w to the horizontal axis; $A_w f_{yw} \sin(\theta_s + \theta_w)$ is the component force of web reinforcement in the f_t direction. The further away the web reinforcement is from the beam soffit the less efficient it is to resist the diagonal splitting. Thus, a positional influence factor d_w/d was applied to the second term. The third term represents the tensile contribution from concrete and was taken as concrete tensile strength $0.5\sqrt{f_c'}$ (MacGregor 1988).

Following expression was proposed by Tan et al. (2001) for the shear strength V_n

of simply supported deep beams:

$$V_n = \frac{1}{\dfrac{\sin 2\theta_s}{f_t A_c} + \dfrac{1}{f_c' A_{str} \sin \theta_s}} \tag{1.13}$$

The above shear strength was determined from the capacity of bottom tension-compression nodal zone. It was demonstrated that if the width of the top nodal zone is comparable to that of the bottom nodal zone, Eq. (1.13) is sufficient to safeguard failure of the top nodal zone. However, there are some limitations in Tan's model. For example, the factor *k* does not satisfy moment equilibrium; the model was highly sensitive to concrete tensile strength, etc. These would affect the model's performance in predicting beam shear strength. Besides, Tan's model was not able to predict failure modes as well as failure locations. The author will discuss it in greater detail in Chapter 2.

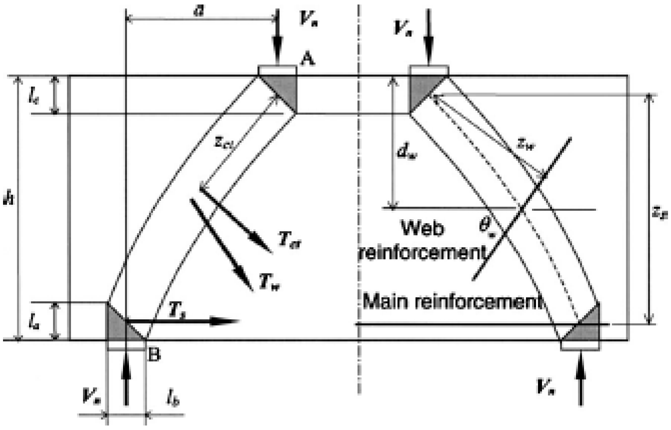

Figure 1.9 STM for simply supported deep beams (Tang et al 2004)

Tang et al (2004) proposed a different approach to account for the effect of transverse stresses to the load-carrying capacity of concrete in the diagonal strut, based on the strut-and-tie concept (**Figure 1.9**). Tang argued that by applying the top load V_n two effects on the diagonal strut are resulted, namely, failure by crushing of concrete diagonal strut and failure by splitting of diagonal strut. Tang adopted Mohr-Columb failure criterion to include these two common failure modes interactively in his model,

$$\frac{f_1}{f_{ct}}+\frac{f_2}{f_c'}=1 \tag{1.14}$$

or

$$\upsilon_1+\upsilon_2=1 \tag{1.15}$$

where υ_1 and υ_2 are defined by

$$\upsilon_1=\frac{f_1}{f_{ct}}=\frac{V_n}{V_{ds}}\le 1 \tag{1.16}$$

and

$$\upsilon_2=\frac{f_2}{f_c'}=\frac{V_n}{V_{dc}}\le 1 \tag{1.17}$$

where V_{ds} and V_{dc} are respective capacities to resist the diagonal splitting and diagonal crushing.

Through moment equilibrium about the top Node A (**Figure 1.9**), and assuming that the capacities provided by the concrete section, the web reinforcement, and the main reinforcement to the diagonal splitting are mobilised at about the same rate, Tang proposed the following expression for the capacity to resist diagonal splitting:

$$V_{ds}=\frac{f_{ct}A_{ct}+f_{yw}A_w\sin(\theta_w+\theta_s)+2f_yA_s\sin\theta_s}{2\cos\theta_s} \tag{1.18}$$

where f_{ct} is the concrete tensile stress given by $0.5\sqrt{f_c'}$; $A_{\mathrm{ct}} = A_{\mathrm{c}}/\sin\theta_{\mathrm{s}}$ is the concrete section area along diagonal strut.

On the other hand, the expression for the capacity to resist diagonal crushing is given by

$$V_{dc}=f_c'A_{str}\sin\theta_s \tag{1.19}$$

It was obtained by assuming that the transverse tensile stress f_1 does not exist so that υ_2=1 and V_{dc}=V_n.

Combining Eqs. (1.15) – (1.19), Tang and Tan (2004) proposed the following reciprocal form for the ultimate shear strength of deep beams:

$$\frac{1}{V_n}=\frac{1}{V_{dc}}+\frac{1}{V_{ds}} \tag{1.20}$$

Eq. (1.20) exhibited a strong interaction relationship between two failure modes, namely, diagonal splitting and diagonal crushing, which are common in the literature. It is shown that Eq. (1.20) is mathematically equivalent to Eq. (1.13).

From Eq. (1.20)

$$V_n=\frac{1}{\dfrac{1}{V_{dc}}+\dfrac{1}{V_{ds}}}=\frac{1}{\dfrac{2\cos\theta_s}{f_{ct}A_{ct}+f_{yw}A_w\sin(\theta_w+\theta_s)+2f_yA_s\sin\theta_s}+\dfrac{1}{f_c{}'A_{str}\sin\theta_s}}$$

Noting that A_{ct}=A_c/sinθ_s, the first term in the denominator is simplified to $\dfrac{\sin 2\theta_s}{A_cf_t}$, where f_t is given by Eq. (1.12). Thus, the equation is simplified to Eq. (1.13)

$$V_n=\frac{1}{\dfrac{\sin 2\theta_s}{A_cf_t}+\dfrac{1}{f_c{}'A_{str}\sin\theta_s}}$$

Kotsovos (1983) proposed the concept of Compressive Force Path (CFP) based on experimental evidence obtained from tests on RC beams. He argued that the shear resistance of an RC beam without shear reinforcement is provided by the concrete region that transmits compressive force path to the supports. The aggregate interlock action is not considered a major mechanism that leads to the beam shear resistance. Kotsovos suggested that for an RC beam at its ultimate limit state, the compressive force is transmitted to the supports by a bilinear path. The proposed compressive force path concept stipulates that shear failure is associated with the presence of tensile stresses developing in the region of the compressive force path. Tensile stresses may develop perpendicular to the path due to the following reasons (Kotsovos, 1988):

a. Changes in the path direction. A tensile stress resultant develops at the location.

b. Varying intensity of the compressive stress field along the path. The material dilation due to high compressive stress intensity induces tensile stresses in the surrounding concrete.

c. Tip of inclined cracks. From fracture mechanics, large tensile stresses develop perpendicular to the direction of the maximum principal compressive stress in the region of the crack tip.

d. Bond failure. It increases locally the intensity of the compressive stress block and gives rise to tensile stresses in the manner described in item b.

According to the compressive force path concept, for a beam under two-point loading with $a/d < 2.0$, the critical tensile stresses occur adjacent to the load point within the middle span. For a beam with $a/d > 2.0$, the critical stresses occur beyond approximately $2d$ from the support where the path direction changes.

Kotsovos contended that by using stirrups to sustain the critical tensile stresses within the compressive force path would prevent shear failure and allow the beam to fail in ductile mode, which was supported by his experimental programme. The key differences between compressive force path method and the strut-and-tie model are:

1. The location of critical tensile stresses is fixed for STM (bottom nodal zone) but

not fixed for CFP (within the region of path).

2. The failure criterion of CFP does not consider tensile stress perpendicular to the compressive stresses. This effect is however considered in the STM (Tan et al 2001).

1.3 STM in Code Provisions

CSA (A23.3-94)

The Canadian standard (CSA A23.3, 1984) is believed to be the earliest code to include strut-and-tie model as a design method for deep beams. CSA A23.3 (1994) extends STM to regions where engineering beam theory does not apply. Strut-and-tie models are used to determine the internal force effect, proportion the reinforcement, and confirm the concrete dimensions. It uses a compressive stress limit based on the work of Vecchio and Collins (1986), which considers the strain compatibility of struts and the strain softening of diagonally cracked concrete as Eq. (1.1). The transverse strain ε_1 is determined from

$$\varepsilon_1 = \varepsilon_s + (\varepsilon_s + 0.002)\cot^2 a_s$$

where ε_s is the strain in the tension tie and is usually taken as ε_y; 0.002 is the assumed strain in the compressive strut at crushing, and a_s is the angle between the strut and the tension tie. After determining $f_{2\max}$ from Eq. (1.1), the capacity of the compressive strut, N_u, can be expressed as

$$\phi_c A_{cs} f_{2\max} \geq N_u \tag{1.21}$$

where A_{cs} is the cross-sectional area of the strut, and ϕ_c is the reduction factor for axial compression which is equal to 0.70. CSA (1994) limits the concrete stress in nodal regions as follows:

- $0.85\phi f_c'$ in nodal regions bounded by compressive struts and bearing areas;
- $0.75\phi f_c'$ in nodal regions anchoring a tension tie in only one direction;
- $0.65\phi f_c'$ in nodal regions anchoring tension ties in more than one direction.

The code demands an orthogonal grid of reinforcing bars near each face of the members or regions designed by the strut-and-tie model; the ratio shall not be less than 0.002 in each direction for the purpose of crack control.

ACI 318-02

Although ACI 318-02 still allows previous shear equations to be used for deep beam design, the code encourages engineers to use strut-and-tie model to design D-regions such as deep beams, corbels, etc. The design of struts, ties and nodal zones is based on the following equation:

$$\phi F_n \geq F_u \tag{1.22}$$

where F_u is the force in a strut or tie, or the force acting on one face of a nodal zone; F_n is the nominal strength of the strut, tie, or nodal zone; and ϕ is the strength reduction factor taken as 0.75. The nominal compressive strength of a strut without longitudinal reinforcement is taken as follows:

$$F_{ns} = f_{cu} A_c \tag{1.23}$$

where A_c is the cross-sectional area at the end of the strut; $f_{cu}=0.85\beta_s f_c'$ is the effective compressive strength of concrete in a strut. Here, a factor β_s is adopted to account for the effect of cracking and confining reinforcement on f_{cu} as follows:

- $\beta_s=1.0$ for a strut of uniform cross-sectional area over its length;
- $\beta_s=0.75$ for a strut with reinforcement ratio satisfying

$$\sum \frac{A_{si}}{bs_i} \sin \gamma_i \geq 0.003 \tag{1.24}$$

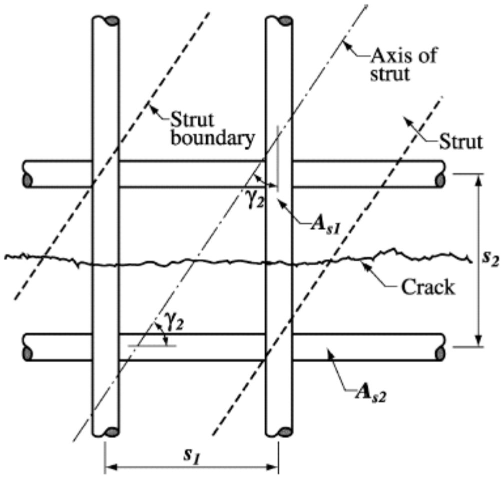

Figure 1.10 Reinforcement crossing a strut (ACI 318-02R)

- β_s=0.60λ for a strut without reinforcement satisfying Eq. (1.24);

where λ is a correction factor for lightweight concrete.

- β_s=0.40 for a strut in a tension member or the tension flanges of a member;
- β_s=0.60 for all other struts.

ACI 318-02 classifies nodal zones into four categories as shown in **Figure 1.11**; the compression strength of nodal zone is given by:

$$F_{nn} = f_{cu} A_n \tag{1.25}$$

where A_n is the area of one face of the nodal zone that F_u perpendicularly acts on. A similar factor β_n is applied on f_{cu} to account for the effect of anchorage of ties on the effective compressive strength of a nodal zone as follows:

- β_n=1.0 for nodal zones bounded by struts or bearing areas, or both;
- β_s=0.80 for nodal zones anchoring one tie;
- β_s=0.60 for nodal zones anchoring two or more ties;

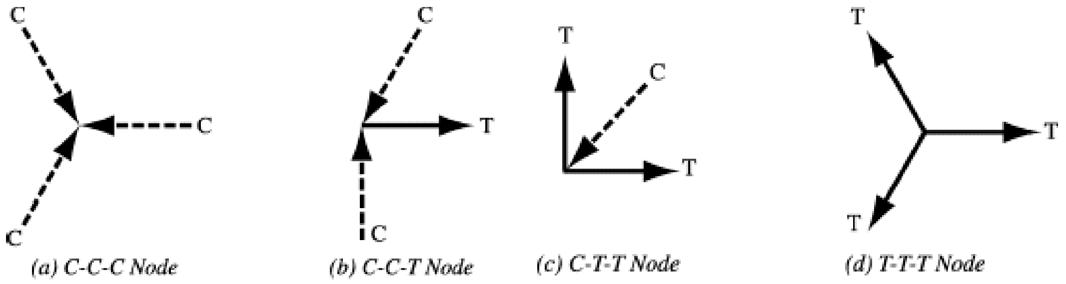

Figure 1.11 Classification of nodes (adapted from ACI 318-02R)

The ACI code permits ties to criss-cross struts but only at nodes. The angle between the axes of any strut and any tie entering a single node should be larger than 25 degrees.

CEB-FIP Model Code 1990

Strut-and-tie method is recommended for the design of deep beams, corbels and other discontinuity regions in CEB-FIP Model Code, ‘without previous knowledge of an elastic solution of stress-pattern’. The code prescribes that the compatibility of deformations be considered under linear elastic analysis of uncracked members and connections. Besides, the code suggests appropriate verifications be carried out within the D-regions, on the following aspects:

- Web reinforcement
- Diagonal web forces (only when the web thickness is smaller than the thickness of the nodes where concentrated forces are acting)
- Strut forces acting on the nodes
- Anchorage of reinforcement in the nodal regions.

A node is defined as a volume of concrete contained within the intersections between compression fields of struts, in combination with anchorage forces and/or external compressive force, i.e. imposed loads or support reactions. The forces of the struts and ties should be balanced in the node region. The strength criteria for nodes are given below:

$$f_{node} \leq 0.85\left[1-\frac{f_{ck}}{250}\right]f_{cd} \text{ (For nodes with only compressive forces)} \qquad (1.26)$$

$$f_{cd2} = 0.60\left[1-\frac{f_{ck}}{250}\right]f_{cd} \qquad \text{(For nodes with main tensile bars)} \qquad (1.27)$$

where f_{node} is average design stresses in any surface or section through a singular node; f_{ck} is the characteristic compressive strength of concrete in MPa; f_{cd} is the design compressive strength of concrete.

For ties, the value should not exceed the design stress of steel in tension. The idealised behaviour of a reinforced tension tie is shown in **Figure 1.12**. As can be seen from the figure, even after cracking has occurred, the reinforced concrete tie still maintains stiffness greater than bare steel reinforcement, showing the tension stiffening effect. However, the code does not recommend the use of tensile resistance of cracked concrete in any tie.

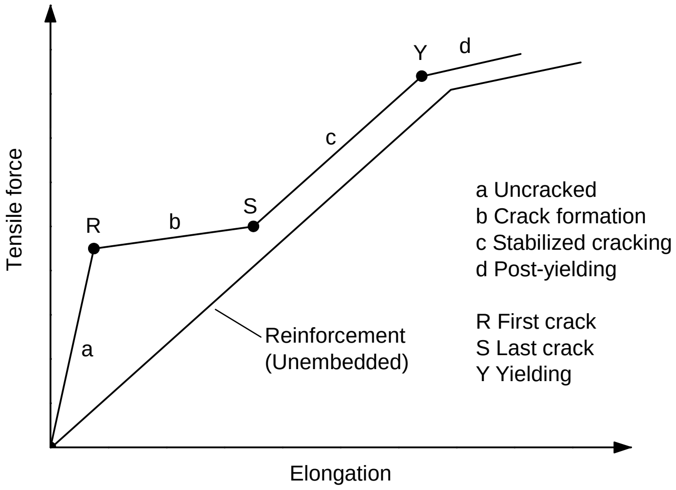

Figure 1.12 Idealized behaviour of reinforced concrete tie (Adapted from CEB-FIP Model Code 1990)

For concrete struts, the strength criteria are the same as Eqs. (1.26) and (1.27), where the former applies to uncracked concrete zones and the latter to cracked zones. The code prescribes that transverse reinforcement is needed for transverse tension due to the bulging compression stress trajectories within a strut unless the concrete tensile strength is sufficient for carrying the tension. A simplified model for estimating the bursting force is shown in **Figure 1.13**. The tensile forces may be estimated as

$$F_{1,x} = 0.3N\left(1 - b_1 / b_2\right) \tag{1.28}$$

$$F_{1,y} = 0.3N\left(1 - h_1 / h_2\right) \tag{1.29}$$

where N is the total load.

The tensile forces must be less than:

$$F_{1,x} < f_{ct} 0.6 b_2 h_1 \ \text{ or } \ A_{sx} f_{yk} \tag{1.30}$$

$$F_{1,y} < f_{ct} 0.6 h_2 b_1 \ \text{ or } \ A_{sy} f_{yk} \tag{1.31}$$

where A_{sx} and A_{sy} are the corresponding cross-sections of well-anchored reinforcement transversely arranged within the tension region; f_{ct} is the axial tensile strength of concrete.

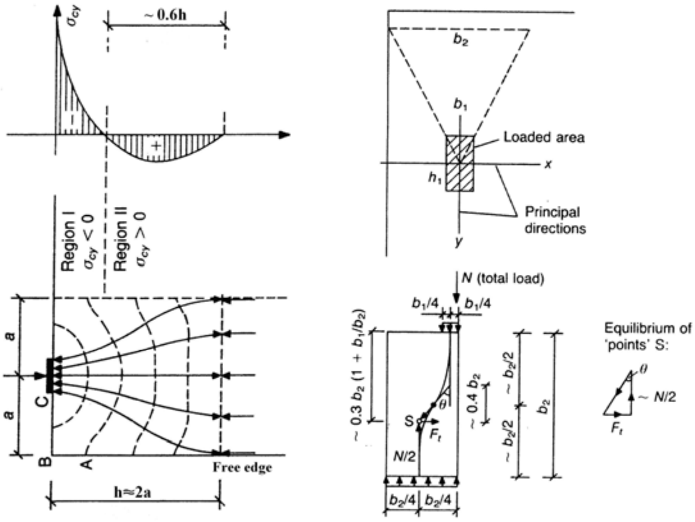

Figure 1.13 Model for estimation of bursting forces across each direction (CEB-FIP Model Code 1990)

1.4 Objectives and Scope of This Work

Although Strut-and-Tie Model (STM) is a rational design tool, common practices of STM involve assuming different levels of stress limits under different stress conditions on the STM components, i.e. nodal zones and struts. However, although stress limits are set in such a way as to include all the stress conditions, they are empirically defined and may be over- or under-conservative for some special conditions. There has been considerable debate about the value of concrete efficiency factors. Researchers in the past have tried to postulate various stress criteria for the concrete strut and nodal zones in the STM (Marti 1985, Schlaich et al. 1987, MacGregor 1988, Bergmeister et al. 1991, Foster and Malik 2002). It should be noted that ACI 318-02, CSA and CEB-FIP model code 1990 give different values on the stress limits according to their respective investigations.

The strut-and-tie model proposed by Tan et al (2001) was shown promising at predicting the ultimate strength of Simply Supported Deep Beams (SSDBs), and it did not rely on empirical stress limits. However, there are several limitations in the derivation of Tan's model, which needs to be further improved for optimal performance. This will be discussed in greater detail in Chapter 2. Besides, the application of the model was limited to single-span deep beams subjected to equal and symmetrical loads. It is not applicable to unsymmetrical and unequal loads which are more common in practice. The test results on deep beams subject to asymmetrical loads is also scarce. On the other hand, continuous deep beams are more often encountered in practice than single span deep beams, however, there is scarcity of rational models for predicting the shear strength of Continuous Deep Beams (CDBs). And it is rare for researchers to take account of support settlement when analysis CDBs, which would significantly affect the beam behaviour. Test result in this regard is also hardly reported in literature, if at all found. The phenomenon of a reduction in shear strength due to an increase in beam size has been known as the ‘size effect’. Nevertheless, the cause of the size effect has long been debated among researchers. Some suggested (Bazant and Kim 1984) it may be explained by fracture-mechanics. Some argued (Kotsovos and Pavlovic 1994) that out of plane actions may be the main cause. However, no convincing experimental evidence had been reported so far. Besides, whether the size effect occurs in deep beams itself remains a question, as the deep beams behave fundamentally different from shallow beams due to mobilization of the arch actions. Interestingly, the use of rational tools such as strut-and-tie model to account for the cause of size effect had rarely been attempted by researchers; however it may turn out to be a worthwhile effort.

The main objectives of this research are to investigate in depth the behaviour and strength of RC deep beams under different loading and support conditions with different member sizes, to improve the original Strut-and-Tie method, and extend the modified STM to a wider range of applications. The specific objectives of the thesis are as follows:

i. To identify the limitations of original STM for SSDBs and to develop a modified STM. Furthermore, the modified STM is to be extended to continuous deep beams and validated with published test results.

ii. To investigate the effects of differential support settlement on the behaviour and strength of CDBs, including crack patterns, load-deflection curves, strains in steel, serviceability loads, and ultimate loads. An experimental programme consisting of six specimens is to be carried out with different middle support conditions. The influence of web reinforcement on beams' behaviour is to be studied in accommodating differential settlements. Based on the modified STM, it will be further developed to include CDBs subjected to support settlement and verified with test results. The robustness of the STM is also to be tested.

iii. To examine the strength and behaviour of SSDBs subjected to asymmetrical loadings. An experimental programme consisting of fourteen specimens is to be conducted. The crack patterns, load-deflection responses, steel and concrete strains, and failure loads will be examined with the effects of load inequality (LI) and load asymmetry (LA). Strut-and-Tie model for predicting the failure loads and failure modes of asymmetrically-loaded deep beams will be derived and the model performance will be compared with ACI 318-05 strut-and-tie method and WCOMD finite element analysis results.

iv. To explore the possible causes of size effect in deep beams and the effects of out-of-plane actions on beam strength. An experimental programme consisting of three groups of eleven specimens with beam size varying from 350mm to 1000mm is to be carried out. Efforts will be made to identify the possible factors governing the size effect in deep beams and to incorporate the factors into the modified STM and to predict test results. Finite element analysis, ACI and CSA code provisions will be used To supplement the study.

Normal strength concrete members are included in the investigation. With regard to loading condition, only concentrated load is considered; uniformly distributed load is excluded. However, it is noted that in design practice uniformly distributed load can always be replaced by a set of equivalent concentrated loads (MacGregor, 1992). Besides, only static loading is considered; dynamic loading is outside the scope of present study. As shear failure is often associated with deep beams, all the test specimens were designed with greater-than-normal longitudinal reinforcement to prevent flexural failure from taking place.

The thesis is organised into three parts as follows: firstly, all the theory work on the proposed modified strut-and-tie models will be presented in Chapter 2, including STM for SSDBs and CDBs under different loading and support conditions, and the application of proposed STM to account for size effect in deep beams. Secondly, the details and results of the test programmes conducted by the author to investigate the behaviour of SSDBs and CDBs will be introduced in Chapter 3 to 5, discussing major experimental findings and strut-and-tie model verifications supplemented with FEM analysis. Lastly, the findings and results of this work is summarised and the recommendations for the future work is proposed in Chapter 6.

CHAPTER 2 MODIFIED STM FOR DEEP BEAMS

2.1 Background

Tan et al. (2001, 2003) have developed a direct STM for Simply Supported Deep Beams (SSDBs), which can consider the effects of different web reinforcement configurations (vertical, horizontal, or inclined), and prestressing tendons. Other than defining the stress limits for the STM components, the model utilizes a failure criterion from the Mohr-Columb theory for nodal zones (tension-compression stress state) as below:

$$\frac{f_1}{f_\mathrm{t}} + \frac{f_2}{f_\mathrm{c}'} = 1 \qquad (2.1a)$$

where f_1 and f_2 are principal tensile and compressive stresses at the nodal zone respectively; f_c' is cylinder compressive strength representing the maximum compressive strength in the f_2 direction; and f_t represents the maximum tensile capacity in the f_1 direction. It is worth noting that the term f_t is the combined tensile strength comprising contributions from concrete and reinforcement (web and main). Case studies have been carried out and the model gives good predictions of the ultimate strengths of normal and high strength concrete deep beams (Tan et al. 2001, Tan et al. 2003).

Kupfer and Gerstle (1973) proposed another biaxial tension-compression stress relationship through successful experiment, as below:

$$\frac{f_1}{f_t} + 0.8\frac{f_2}{f_c'} = 1 \qquad (2.1)$$

It was shown that Eq. 2.1 is in better agreement with the test results than the Mohr-Columb theory. Similarly, this failure criterion offers a simple linear interactive relationship between two limit failure modes, namely, brittle concrete crushing and ductile reinforcement yielding. By adopting this interactive stress-based failure criterion, no other empirically set stress limit is needed in the model for calculating the ultimate strength.

Besides, there are several limitations in Tan's model as follows. Firstly, when deriving the stress distribution factor k, only the force equilibrium was satisfied. Secondly, the model was highly sensitive to the value of concrete tensile strength, which is difficult to be determined accurately in practice. Thirdly, the softening factor which is implicit in the model was not derived explicitly.

The author has re-examined Tan's model (2001 and 2003) and its shortcomings and proposes a modified STM. A new failure criterion is used in the model. The stress distribution factor k is newly derived from the consideration of both force and moment equilibrium, and its influence on model prediction of beam shear strength is discussed through a parametric study. Concrete tension-stiffening properties are used instead of concrete tensile strength to improve model prediction consistency.

The author also illustrates that, by the use of interactive failure criterion (such as Kupfer's failure criterion), the softening effect of concrete strength due to the presence of transverse tensile strain is implicitly taken into consideration. The softening effect in the author's model is comparable to MCFT (Vecchio and Collins, 1986) and Belarbi and Hsu' (1994) equations. The modified model is verified against 233 test results of normal and high strength concrete simply supported deep beams (SSDBs). Comparison results show that the modified STM yields more accurate and consistent predictions of beam ultimate shear strength compared with the original one (Tan et al., 2001; Tan et al., 2003).

The modified STM is further extended to concrete continuous deep beams (CDBs) for the first time and is shown to be in good agreement with 54 published test results. It is also interesting to see the distribution of reaction forces among the 3 supports can be reasonably well predicted by the proposed strut-and-tie model.

2.2 Modified STM for SSDB

From the equilibrium of forces at the bottom nodal zone of inclined strut (**Figure 2.1**)

$$F_{\mathrm{c}} = \frac{V_{\mathrm{n}}}{\sin\theta_s} \tag{2.2}$$

$$T_{\mathrm{s}} = \frac{V_{\mathrm{n}}}{\tan\theta_s} \tag{2.3}$$

where F_{c} and T_{s} are the forces in the concrete strut and bottom reinforcement (tension tie), respectively. V_{n} is the shear strength of the beam. The inclined angle of the diagonal strut θ_s can be computed from

$$\tan\theta_s = \frac{h - \frac{l_{\mathrm{c}}}{2} - \frac{l_{\mathrm{d}}}{2}}{a} \tag{2.4}$$

where h is the beam depth, l_{c} and l_{d} are the respective depth of bottom and top nodal zones, and a is the shear span measured from centre lines between the load and support bearing plates.

The principal tensile stress f_1 at the tension-compression nodal zone arises from the component force of longitudinal reinforcement in the direction perpendicular to the diagonal strut, namely, $T_s \sin\theta_s$. Thus, f_1 can be expressed by:

$$f_1 = \frac{kT_s \sin\theta_s}{A_c / \sin\theta_s} \tag{2.5}$$

where $T_s\sin\theta_s/(A_c/\sin\theta_s)$ is the average equivalent tensile stress across the diagonal strut and A_c is the effective beam cross-sectional area, k in the numerator is a factor taking account of the non-uniformity of the stress distribution. The original model assumed a triangular stress distribution along the diagonal strut due to the presence of bottom steel. According to force equilibrium, namely, by equating $T_s\sin\theta_s$ to the force represented by the triangular stress block, Tan et al. (2001) proposed $k = 2$. Although the original model satisfies force equilibrium, it is worth noting that the moment equilibrium is not observed. To satisfy both moment and force equilibrium, and use the linear stress assumption, the smeared stress distribution is shown in **Figure 2.2** and the factor k can be determined accordingly.

First, consider one reinforcing bar that criss-crosses the diagonal strut and inclines at an angle θ_w from the horizontal (**Figure 2.1**). The effect of single reinforcement T is “smeared” across the entire strut length. For simplicity, the tensile stress due to tension force T is assumed to distribute linearly along the diagonal strut. To achieve equivalence between the discrete force T and the assumed tensile stress distribution, the latter must satisfy both force and moment equilibrium. Applying force equilibrium in the f_1 direction to tensile force T of the steel bar and the idealized stress distribution along the diagonal strut (**Figure 2.1**), the following equation can be established:

$$\left(\frac{k+k'}{2}\right)p_{\mathrm{t}}\cdot b_{\mathrm{w}}d_{\mathrm{c}}/\sin\theta_s = T\sin\left(\theta_s+\theta_w\right) \qquad (2.6)$$

where k and k' are the stress distribution factors at the respective bottom and top nodal zones, θ_s is the diagonal strut angle, b_{w} is the beam width, and d_{c} is the beam effective depth taken as the vertical distance between the centroids of top and bottom nodal zones. It should be noted that $p_{\mathrm{t}} = T\sin(\theta_s+\theta_w)/(A_{\mathrm{c}}/\sin\theta_s)$ is the average equivalent tensile stress across the diagonal strut due to the component of T in the principal tensile direction of bottom nodal zone.

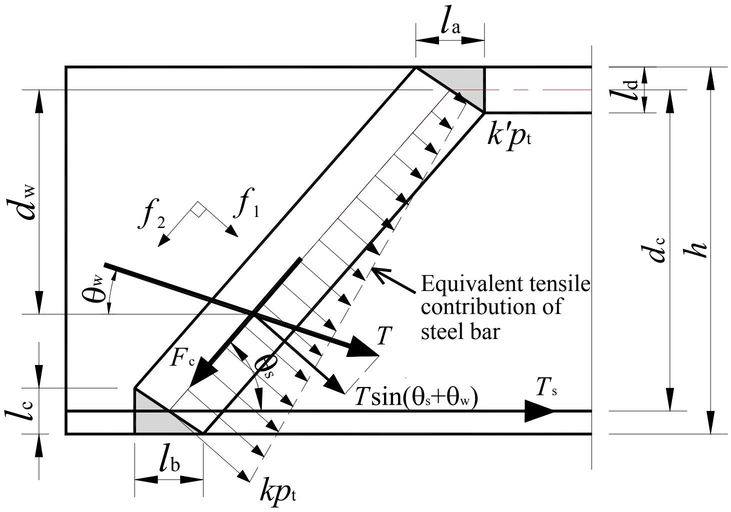

Figure 2.1 Determination of tensile stress factors at nodal zones

From moment equilibrium about the top node between T and the idealized tensile stress distribution:

$$\left(\frac{k'}{2}+\frac{k-k'}{3}\right)\left(d_{\mathrm{c}}/\sin\theta_{\mathrm{s}}\right)^2 b_{\mathrm{w}}p_{\mathrm{t}} = T\sin\left(\theta_{\mathrm{s}}+\theta_{\mathrm{w}}\right)\cdot\left(d_{\mathrm{w}}/\sin\theta_{\mathrm{s}}\right) \qquad (2.7)$$

Comparing Eqs. (2.6) and (2.7), the following factors for determining the principal tensile stress at the respective top and bottom nodal zones can be obtained

$$\begin{cases} k' = 4 - 6 \cdot \dfrac{d_{\mathrm{w}}}{d_{\mathrm{c}}} \\ k = 6 \cdot \dfrac{d_{\mathrm{w}}}{d_{\mathrm{c}}} - 2 \end{cases} \tag{2.8}$$

For the case of bottom longitudinal reinforcement (**Figure 2.2**), $d_{\mathrm{w}} = d_{\mathrm{c}}$ and $\theta_w = 0$, the stress distribution factor is:

$$\begin{cases} k' = -2 & \text{(compression)} \\ k = 4 & \text{(tension)} \end{cases} \tag{2.9}$$

Thus, the principal tensile stress f_1 in the model can be expressed as below:

$$f_1 = \frac{4T_{\mathrm{s}} \sin\theta_s}{A_{\mathrm{c}} / \sin\theta_s} \tag{2.10}$$

The maximum tensile capacity in the f_1 direction is a composite term and can be expressed by

$$f_{\mathrm{t}} = f_{\mathrm{ct}} + f_{\mathrm{st}} \tag{2.11}$$

The term f_{ct} represents the contribution from concrete tensile strength. The original model (Tan et al., 2001; Tan et al., 2003) used the concrete tensile strength $f_{\mathrm{ct}} = 0.5\sqrt{f_{\mathrm{c}}'}$. However, at the ultimate state, as concrete has cracked extensively, concrete tensile strength is significantly reduced. It would be un-conservative to use full concrete tensile strength as f_{ct}. Besides, the predictions of original model are highly dependent on the magnitude of concrete tensile strength, which is to some extent difficult to be determined accurately. This is one factor that has significant influence on the model accuracy and consistency. To improve on it, concrete tension stiffening term is used instead. The following equation for the tensile strength of cracked reinforced concrete proposed by Belarbi and Hsu (1994) is adopted in the modified model:

$$f_{\mathrm{ct}} = 0.31\sqrt{f_{\mathrm{c}}'}\left(\frac{\varepsilon_{\mathrm{cr}}}{\varepsilon_1}\right)^{0.4} \tag{2.12}$$

where ε_{cr} is the strain of concrete at cracking, taken as 0.00008 (Belarbi and Hsu, 1995). ε_1 is the principal tensile strain of concrete strut and can be calculated from

$$\varepsilon_1 = \varepsilon_{\mathrm{s}} + (\varepsilon_{\mathrm{s}} + \varepsilon_2)\cot^2\theta_s \tag{2.13}$$

where ε_s and ε_2 are the tensile strain of longitudinal steel and peak compressive strain of concrete strut at crushing, respectively. Usually ε_2 is taken as 0.002 for normal strength concrete. In the modified model, the term f_{ct} is much smaller compared to the tensile contribution from reinforcement f_{st} and can usually be neglected for conservatism. However, for improved accuracy in comparison, it is included in this proposed model. Thus, through incorporating Eq. (2.12) the modified model is much less dependent on the magnitude of concrete tensile strength and is more robust in prediction consistency.

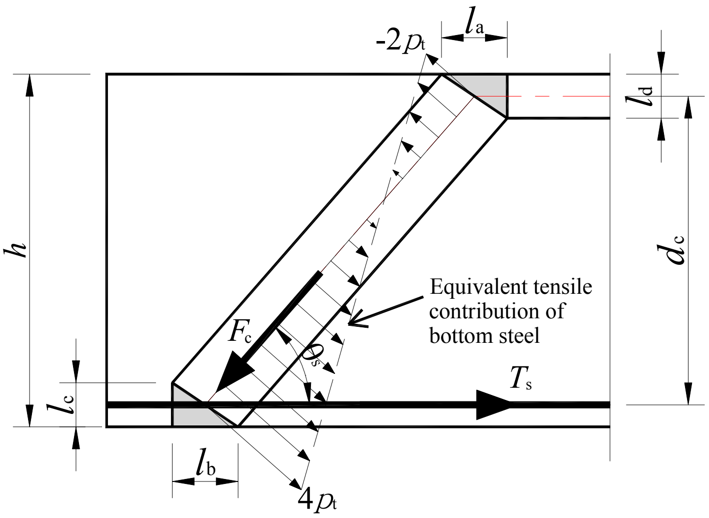

Figure 2.2 Assumed tensile stress distribution aroused by bottom steel

The term f_{st} represents the contribution from steel reinforcement. It consists of two parts: f_{sw} from the web reinforcement and f_{ss} from the longitudinal reinforcement.

$$f_{\mathrm{st}} = f_{\mathrm{sw}} + f_{\mathrm{ss}} \tag{2.14}$$

The presence of web reinforcement in the strut restricts the diagonal crack from quickly propagating to either end of strut. Although this "stitching" action only occurs at discrete locations of web reinforcement, the congregate sum effects are considered in the STM at the interface between the top-and-bottom nodal zones and the diagonal strut itself.

For web reinforcement, a composite factor can be obtained from the summation of k factors of all individual web steel bars. Assuming that there are n_{s} web steel bars evenly distributed along the strut, the stress distribution factors for web reinforcement can be written as follows:

$$\begin{cases} k' = \sum_{i=1}^{n_{\mathrm{s}}} \left(4 - 6\dfrac{d_{\mathrm{wi}}}{d_{\mathrm{c}}}\right) = 4n_{\mathrm{s}} - 3n_{\mathrm{s}} = n_{\mathrm{s}} \\ k = \sum_{i=1}^{n_{\mathrm{s}}} \left(6\dfrac{d_{\mathrm{wi}}}{d_{\mathrm{c}}} - 2\right) = 3n_{\mathrm{s}} - 2n_{\mathrm{s}} = n_{\mathrm{s}} \end{cases} \tag{2.15}$$

Thus, the tensile contribution of web reinforcement at the interface of nodal zone can be calculated as

$$f_{\mathrm{sw}} = \frac{A_{\mathrm{sw}} f_{\mathrm{yw}} \sin(\theta_s + \theta_w)}{A_{\mathrm{c}} / \sin\theta_s} \tag{2.16}$$

where $A_{\mathrm{sw}} = n_{\mathrm{s}} A_{\mathrm{sw1}}$ represents the total area of web reinforcement criss-crossing the concrete strut, where A_{sw1} is the area of an individual bar. For the common cases of vertical or horizontal web reinforcement, Eq. (2.16) reduces to $\dfrac{A_{\mathrm{sv}} f_{\mathrm{yv}} \sin 2\theta_s}{2A_{\mathrm{c}}}$ or $\dfrac{A_{\mathrm{sh}} f_{\mathrm{yh}} \sin^2\theta_s}{A_{\mathrm{c}}}$, respectively, where, A_{sv} and A_{sh} are the respective total areas of vertical and horizontal web reinforcement within the shear span.

The contribution of bottom longitudinal steel f_{ss} can be obtained in a similar fashion as Eq. (2.10):

$$f_{\mathrm{ss}} = \frac{4A_{\mathrm{s}}f_{\mathrm{y}}\sin\theta_s}{A_{\mathrm{c}}/\sin\theta_s} \tag{2.17}$$

The principal compressive stress f_2 in the direction of the left diagonal strut at the bottom nodal zone is computed from:

$$f_2 = \frac{F_c}{A_{\mathrm{str}}} \tag{2.18}$$

where A_{str} is the cross-sectional area at the bottom end of the diagonal strut.

Substituting Eqs. (2.2) and (2.3) into Eqs. (2.10) and (2.18), and combining with Eq. (2.1), the following expression for the nominal shear strength V_{n} is proposed:

$$V_{\mathrm{n}} = \frac{1}{\dfrac{4\sin\theta_s\cos\theta_s}{A_c f_t} + \dfrac{0.8}{A_{\mathrm{str}} f_c^{'}\sin\theta_s}} \tag{2.19}$$

It is noteworthy that the top nodal zone is subjected to a biaxial compression-compression stress state. The author suggests that the compressive stress along the diagonal strut at the interface of top nodal zone should not exceed f_{c}'. Therefore, due to the interactive nature between tension and compression stresses in the failure criterion, Eq. (2.19) safeguards the compression failure of the top nodal zone, given that the width of the top nodal zone is comparable to that of the bottom support region. Thus, no further consideration is given to the top node.

The accurate value of angle θ_s needs to be determined through an iterative procedure as documented in the original model (Tan et al. 2001; Tan et al., 2003), because l_{d} is initially unknown in Eq. (2.4). In practice, the iterative procedure can be simplified by assuming the depth of top nodal zone to be equal to that of the bottom nodal zone, i.e. $l_d = l_c$ in **Figure 2.1**. By doing so, it is found that the error introduced in V_n is generally less than 2%, which is in accordance with the finding of previous researchers (Tan et al., 2001; Tang and Tan, 2004). This is because l_d is typically ten times smaller than the beam height h. Therefore, even a rough estimate of l_d will have little effect on the accuracy of inclined strut angle θ_s. However, for better agreement with test results, the iterative procedure is adopted in this chapter for model verifications. Usually, the convergence is very rapid. An iteration of at most 3 or 4 rounds will be sufficient to obtain a convergent result for the nodal zone depth. The entire procedure can be easily implemented using a spreadsheet. The iterative procedure for calculating the ultimate strength of deep beams by the modified model is shown in **Figure 2.3** for purpose of implementation.

In summary, the major modifications made to the original STM (Tan et al., 2001; Tan et al., 2003) are listed below. First, the stress distribution factor k in the model is obtained considering both force and moment equilibrium. Second, the component of tension force of the reinforcement in the direction parallel to the concrete diagonal strut is included in the calculation of principal compressive stress f_2. Third, the modified STM incorporates the more realistic tension stiffening effect rather than the full concrete tensile strength when evaluating the composite concrete tensile strength.

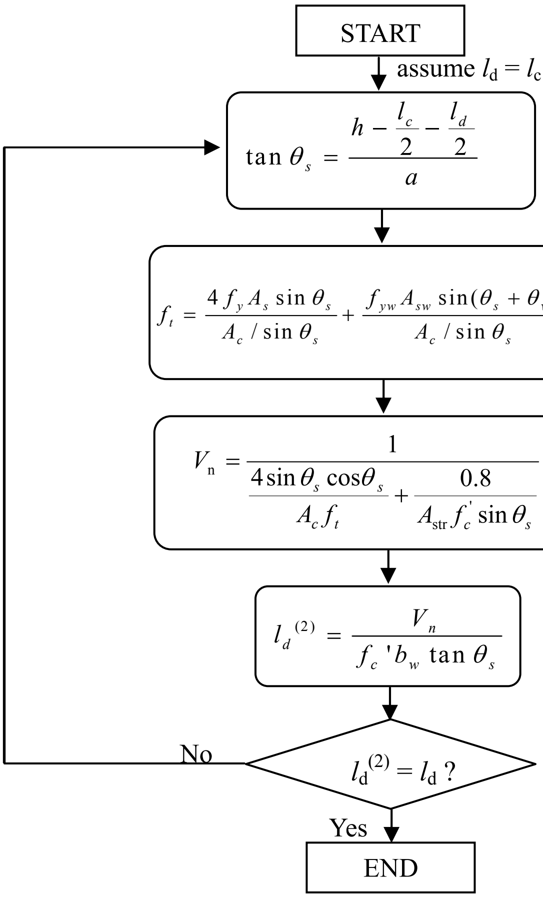

Figure 2.3 Iteration procedure for computing the ultimate strength of SSDBs

2.2.1 Verification of Proposed STM

The shear strength predictions of 233 simply supported deep beams, shown in **Table 2.1**, have been evaluated by the original and the proposed modified STM (Eq. (2.19)). The concrete strength of deep beams varied from 16 to 120 MPa, including normal and high strength concrete. The beams had an overall depth h ranging from 200 to 1750 mm, and an a/d ratio from 0.28 to 2.0. Longitudinal main reinforcement ratio ranged from 0.90 to 4.07%, and vertical and horizontal web reinforcement ratios ranged from zero to 2.86%, and zero to 3.17%, respectively. The predicted shear strengths V_n versus experimental shear strengths V_{exp} are plotted in **Figure 2.4b** and **2.4c** for both original and modified models. The average (AVG) and coefficient of variation (C.O.V.) V_n/V_{exp} ratios have also been reported in the figure. The modified STM predicts the ultimate shear strength more accurately and consistently than the original STM.

Table 2.1 SSDBs used for experimental comparison

Kong et al. (1972): S-30, S-25, S-20, S-15, S-10, D-30, D-25, D-20, D-15, D-10
Smith and Vantsiotis (1982): 0A0-44, 0A0-48, 1A1-10, 1A3-11, 1A4-12, 1A4-51, 1A6-37, 2A1-38, 2A3-39, 1A4-40, 2A6-41, 3A1-42, 3A3-43, 3A4-45, 3A6-46, 0B0-49, 1B1-01, 1B3-29, 1B4-30, 1B6-31, 2B1-05, 2B3-06, 2B4-07, 2B4-52, 2B6-32, 3B1-08, 3B1-36, 3B3-33, 3B4-34, 3B6-35, 4B1-09, 0C0-50, 1C1-14, 1C3-02, 1C4-15, 1C6-16, 2C1-17, 2C3-03, 2C3-27, 2C4-18, 2C6-19, 3C1-20, 3C3-21, 3C4-22, 3C6-23, 4C1-24, 4C3-04, 4C3-28, 4C4-25, 4C6-26, 0D0-47, 4D1-13
Subedi et al. (1986), Subedi (1988): 1A2, 1B1, 1B2, 1C2, 1D1, 1D2, 2A2, 2B2, 2D1, 2D2, 4G1, 4G2, 4G3, 4G4
Walraven and Lehwalter (1994): V711/4, V022/4, V511/4, V411/4, V711/3, V022/3, V511/3, V411/3, V711, V022, V511
Tan et al. (1995): A-0.27-2.15, A-027-3.23, A-0.27-4.30, A-0.27-5.38, B-0.54-2.15, B-0.54-3.23, B-0.54-4.30, B-0.54-5.38, C-0.81-2.15, C-0.81-3.23, D-1.08-2.15, D-1.08-3.23, D-1.08-4.30, D-1.08-5.35, E-1.62-3.23, E-1.62-4.30, E-1.62-5.38, E-2.16-4.30, G-2.70-5.38
Tan et al. (1997a): I-1/0.75, I-3/0.75, I-4/0.75, I-6S/0.75, II-2N/1.00, II-3/1.00, II-5/1.00, II-6N/1.00, III-2N/1.50, III-2S/1.50, III-6N/1.50
Tan et al. (1997b): 1-2.00/0.75, 1-2.00/1.00, 2-2.58/0.25, 2-2.58/0.50, 2-2.58/0.75, 3-4.08/0.25, 3-4.08/0.50, 3-4.08/0.75, 3-4.08/1.00
Foster and Gilbert (1998): B1.2-1, B1.2-2, B1.2-3, B1.2-4, B2.0-1, B2.0-2, B2.0-3, B2.0A-4, B2.0B-5, B2.0C-6, B2.0D-7, B3.0-1, B3.0-2, B3.0-3, B3.0A-4, B3.0B-5
Tan and Lu (1999): 1-500/0.50, 1-500/0.75, 1-500/1.00, 2-1000/0.50, 3-1400/0.50, 4-1750/0.50
Shin et al. (1999): MHB1.5-50, MHB1.5-75, MHB1.5-100, MHB2.0-50, MHB2.0-75, MHB2.0-100, MHB2.5-50, MHB2.5-75, MHB2.5-100, HB1.5-50, HB1.5-75, HB1.5-100, HB2.0-50, HB2.0-75, HB2.0-100, HB2.5-50, HB2.5-75, HB2.5-100
Oh and Shin (2001): N4200, N42A2, N42B2, N42C2, H4100, H41A2(1), H41B2, H41C2, H4200, H42A2(1), H42B2(1), H42C2(1), H4300, H43A2(1), H43B2, H43C2, H45A2, H45B2, H45C2, H41A0, H41A1, H41A2(2), H41A3, H42A2(2), H42B2(2), H42C2(2), H43A0, H43A1, H43A2(2), H43A3, H45A2(2), U41A0, U41A1, U41A2, U41A3, U42A2, U42B2, U42C2, U43A0, U43A1, U43A2, U43A3, U45A2, N33A2, N43A2, N53A2, H31A2, H32A2, H33A2, H51A2, H52A2, H53A2
Yang et al. (2003): L5-40, L5-60, L5-60R, L5-75, L5-100, L10-40R, L10-60, L10-100, UH5-40, UH5-60, UH5-75, UH5-100, UH10-40, UH10-40R, UH10-60, UH10-100

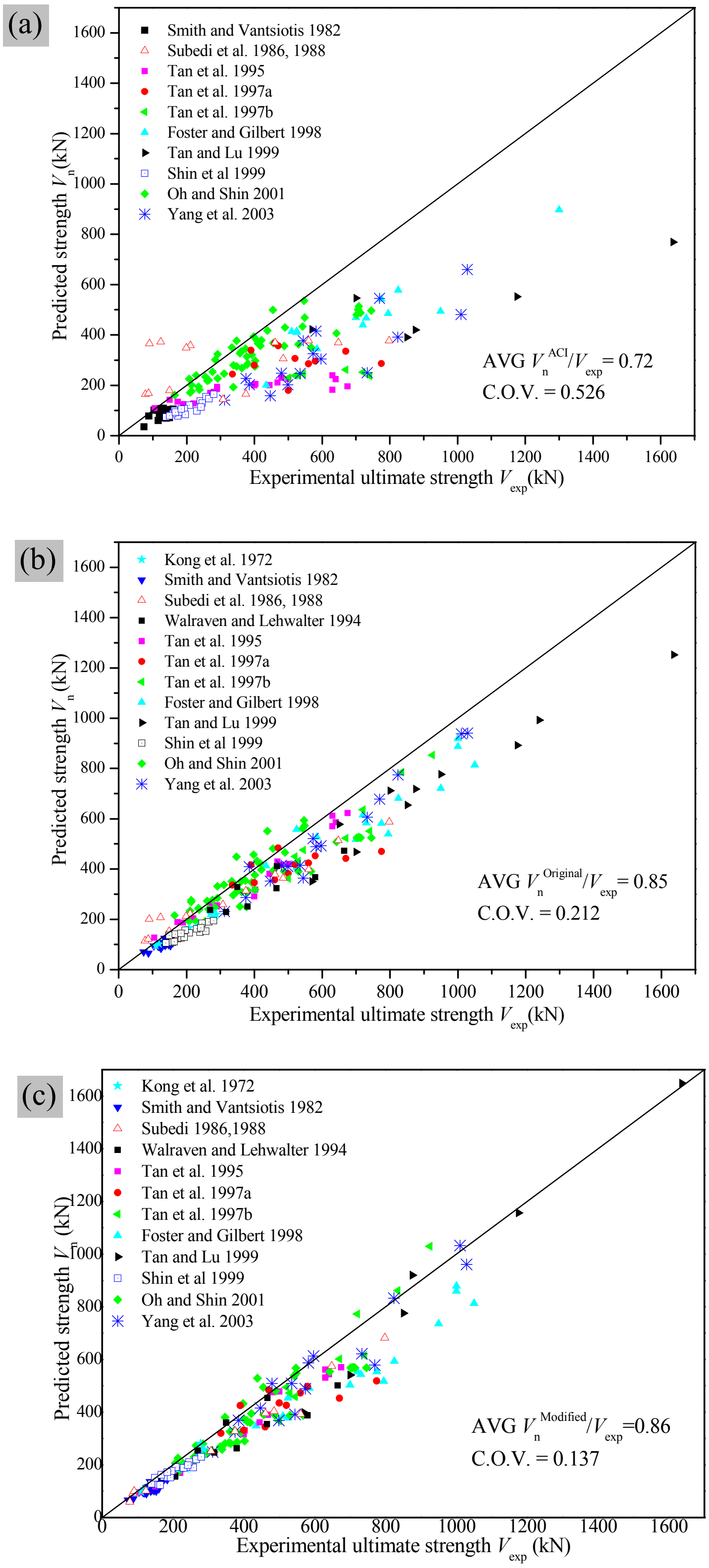

Figure 2.4 Ultimate strength predictions by means of: (a) ACI 318-99 (212 beams); (b) Original STM; (c) Modified STM for 233 reinforced concrete tested deep beams

The results obtained in terms of shear strength from the modified model on the 212 specimens have been compared with results obtained from ACI 318-99. Ten specimens from Kong et al. (1972) have been excluded from the case study because ACI 318-99 does not include the design of deep beams with inclined web reinforcement. The predicted shear strength V_n versus experimental shear strength V_{exp} are plotted in **Figure 2.4a** for ACI code. It can be observed that while ACI 318-99 gives AVG = 0.72 and C.O.V. = 0.526, the modified model provides AVG = 0.86 and C.O.V. = 0.137, highlighting improvement in both accuracy and consistency. It is noted that the shear strengths of some beams from Subedi (1986) were significantly over-predicted by the ACI code. It may be worth noting that the specimens were tested using relatively small loading and support bearing plates, around 100mm in width. This leads to significant reduction in diagonal struts and nodal zones, thus decreasing their capacities, and resulting in significant reduction in capacity. However, the ACI shear equation is unable to capture this effect as it does not consider the influence of the loading and bearing plate sizes. Besides, Subedi's beams were very lightly reinforced (ρ_s is around 0.25%); this may also lead to unconservative predictions by ACI code.

2.2.2 Influence of Factor *k* on the Prediction of Ultimate Strength V_n

The actual tensile stress distribution along the diagonal strut is highly nonlinear and difficult to be determined mechanically. For simplicity, it is assumed that the tensile stress distribution transverse to the diagonal strut is kp_t at the bottom nodal zone. Thus the maximum tensile capacity in the f_1 direction is:

$$f_{\mathrm{t}} = \frac{k f_{\mathrm{y}} A_{\mathrm{s}} \sin\theta_s}{A_{\mathrm{c}} / \sin\theta_s} + \frac{f_{\mathrm{yw}} A_{\mathrm{sw}} \sin(\theta_s + \theta_w)}{A_{\mathrm{c}} / \sin\theta_s} + f_{\mathrm{ct}} \tag{2.20}$$

The beam ultimate shear strength can be expressed from Eq. (2.19)

$$V_{\mathrm{n}} = \frac{1}{\dfrac{k\sin\theta_s \cos\theta_s}{f_{\mathrm{t}} A_{\mathrm{c}}} + \dfrac{\sin\theta_s}{f_{\mathrm{c}}' A_{\mathrm{str}}}} = \frac{1}{\dfrac{\cos\theta_s}{f_{\mathrm{y}} A_{\mathrm{s}} \sin\theta_s + \dfrac{A_{\mathrm{sw}} f_{\mathrm{yw}} \sin(\theta_s + \theta_w)}{k} + \dfrac{f_{\mathrm{ct}} A_{\mathrm{c}}}{k \sin\theta_s}} + \dfrac{0.8}{f_{\mathrm{c}}' A_{\mathrm{str}} \sin\theta_s}} \tag{2.21}$$

From the mathematical form of Eq. (2.21), it is noted that if the deep beam is not provided with any web reinforcement A_{sw} and the concrete tensile contribution f_{ct} is ignored, the prediction of ultimate shear strength V_{n} is completely independent of the k factor. That is to say, whatever the form of stress distribution might be along the diagonal strut, the model predicts the same value of V_{n} for the beam. However, as mentioned in the previous section, for optimal predictions, the term f_{ct} is considered. Thus, from Eq. (2.21), it can be deduced that with an increase in the k factor, V_{n} will slightly decrease. This is because as k increases, the contributions from web steel and concrete (which are independent of k) to the composite tensile strength f_{t} become relatively insignificant. Thus the f_1/f_{t} ratio increases as k increases, resulting in a relatively smaller failure load.

To demonstrate how the value of k influences the ultimate shear strength quantitatively, a parametric study is carried out. Two-hundred-and-sixteen fictitious beams with the same a/d ratio of 0.75 and a main reinforcement ratio of 1.5% are analyzed using the proposed STM. The variables are the web reinforcement ratio (ρ_{w}) ranging from 0 to 1.0% and concrete strength (f_{c}') from 20 to 80 MPa. The influence of k factor on the model prediction of beam shear strength V_{n} can be represented by the percentage of V_{n}, expressed by $(V_{\mathrm{n}} - V_{\mathrm{k=4}})/V_{\mathrm{k=4}}$, where $V_{\mathrm{k=4}}$ represents the beam shear strength obtained from proposed STM with k = 4. The plotted curves are shown in **Figure 2.5**. For higher web reinforcement ratios, the model predictions decrease more quickly as factor k increases. Similarly, for higher concrete strengths, the model predictions decrease more quickly as k increases. Generally, there are about 3% of reduction in shear strength when ρ_w goes from 0 to 1.0% and about 2% reduction when f_c' goes from 20 to 80 MPa. For $2 \leq k \leq 4$, the predictions are greater than $V_{k=4}$, but when $4 \leq k \leq 10$, the predictions are smaller than $V_{k=4}$. However, as shown in **Figure 2.5** the reduction is generally less than 5% of the predicted beam shear strength when k is greater than 4. Thus, it can be concluded that the k = 4 derived from the linear stress distribution assumption is sufficiently accurate for the model predictions. Besides, the new model now satisfies both force and moment equilibrium.

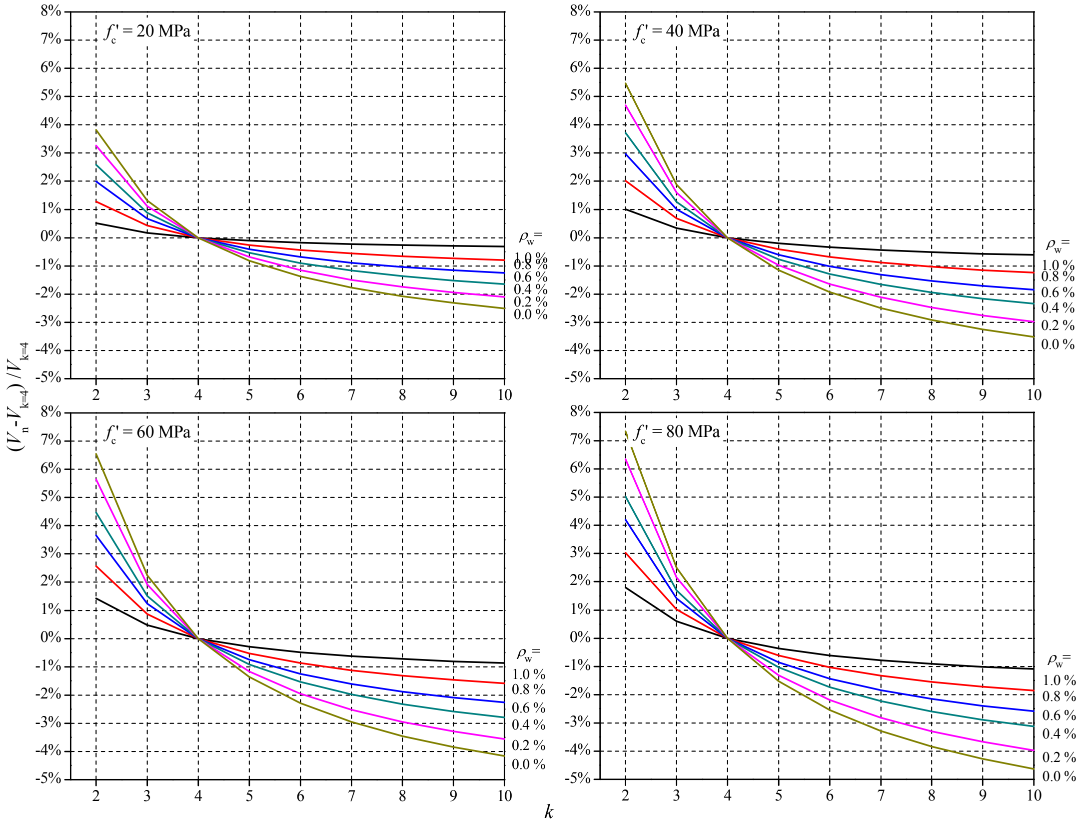

Figure 2.5 Influence of factor k on ultimate shear strength predictions

2.2.3 Softening Effect in the STM

Experimental studies have provided strong evidence that the ability of diagonally cracked concrete to resist compression decreases as the amount of tensile straining increases. A number of analytical models (Vecchio and Collins, 1986 and 1993; Belarbi and Hsu, 1995) have been proposed to represent the compression softening effect observed in cracked reinforced concrete in tension-compression stress state. According to the proposed STM, the equation that yields concrete softening coefficient v can be expressed as:

$$\frac{F_\mathrm{c}}{A_\mathrm{str}} = v f_\mathrm{c}' \tag{2.22}$$

Substituting Eqs. (2.10), (2.18) and (2.22) into Eq. (2.1), the following equation can be obtained:

$$v = 0.8 - \frac{3.2 T_s \sin^2 \theta_s}{A_\mathrm{c} f_\mathrm{t}} \tag{2.23}$$

where T_s is the tension force in the bottom reinforcement and can be expressed as $\varepsilon_\mathrm{s} E_\mathrm{s} A_\mathrm{s}$. It is noteworthy that the second term in Eq. (2.23) represents the contribution of tension force of bottom steel resolved in the direction of diagonal strut, which negates certain amount of compression force in the strut itself. The third term in Eq. (2.23) represents the contribution from transverse tensile stress due to bottom steel, which is the main factor for concrete softening. Substituting Eq. (2.20) into Eq. (2.23) and utilizing the relationship between T_s and ε_s, the following expression for the concrete softening coefficient is established,

$$v = 0.8 - \frac{3.2 E_s \varepsilon_s}{4 f_y + \dfrac{A_{sw} \sin(\theta_s + \theta_w)}{A_s \sin\theta_s} f_{yw} + \dfrac{f_{ct}}{\rho_s \sin^2\theta_s}} \tag{2.24}$$

where E_s and A_s are respectively the elastic modulus and cross-sectional area of longitudinal reinforcement; ε_s is the strain in the longitudinal reinforcement; A_{sw} is the cross-section area of web reinforcement crossing the diagonal strut; θ_s is the inclined angle of strut; f_y and f_{yw} are the yield strengths of the longitudinal and web reinforcement, respectively; A_{str} is the cross-sectional area of diagonal strut; $\rho_s = A_s/A_c$ is the effective longitudinal reinforcement ratio.

From Eq. (2.24), it is worth noting that the softening factor v in the STM is not only influenced by the strut angle θ_s but also by other variables such as compressive strength of concrete, yield strength and reinforcing ratio of steel reinforcement (main and web). However, the strut angle θ_s is the major variable that affects the softening coefficient v significantly. For a larger reinforcement ratio or greater yield strength of steel, the slope becomes gentler, i.e. the decreased portion of concrete compressive strength is less than in those lightly reinforced beams. Web reinforcement seems to reduce the softening slope, but the effect is minimal.

A typical deep beam specimen, say, 3-4.08/0.75 is chosen and the softening relationship by the STM is plotted in **Figure 2.6** together with Vecchio and Collins (1986) and Belarbi and Hsu (1995) softening curves. Details of the specimen are reported in Tan et al. (1997)'s experimental programme. In the figure, ε_s is the strain in the bottom main steel and the strut angle θ_s is 45°. It is shown that the concrete compressive strength has a nearly linear descending trend with an increase of strain in the bottom steel. This is due to the adoption of a linear interactive failure criterion in STM. The softening coefficient of STM is slightly larger than the other two curves when steel strain ε_s is relatively small. This is the situation when the beam is heavily reinforced and the strain in longitudinal reinforcement is small when the beam approaches failure. When ε_s is close to the yield strain ε_y (for f_y=499 MPa, E=20000 MPa, ε_y=0.0025), the STM softening coefficient v is comparable to the other softening curves (**Figure 2.6**), and when ε_s exceeds the yield strain, the STM coefficient is less than those determined by the other three equations, indicating a greater softening effect.

As can be seen from above, although the failure criterion adopted in the STM is based on stress values (Eq. (2.19)), the softening effect of concrete compressive strength due to transverse tensile strain is implicitly taken into account through Eq. (2.24). Furthermore, the descending trend with an increase of steel strain is determined not only by the strut angle θ_s but also by the web and main reinforcement details. This seems more reasonable for deep beams.

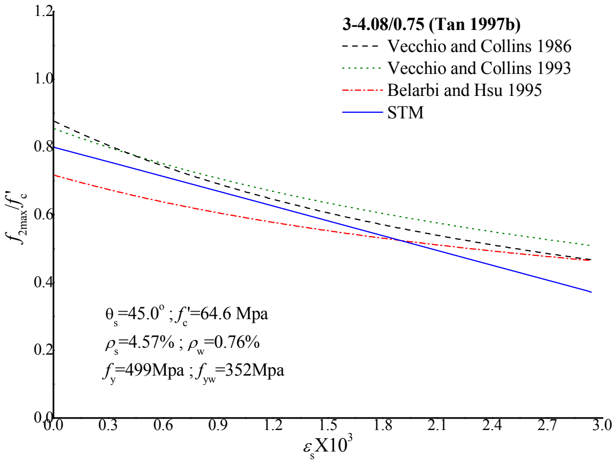

Figure 2.6 Typical maximum concrete compressive stress as function of tensile strain in reinforcement

2.3 Modelling Continuous Deep Beams

A Strut-and-Tie Model for two-span continuous deep beams (CDBs) is proposed in **Figure 2.7**. It can be idealized as a statically indeterminate truss as shown in **Figure 2.8**. Assuming perfect elastic-plastic material properties for concrete and steel bars, the internal forces of the truss are solved. Detailed derivation can be referred to Appendix A. They are denoted as F_{c1} = A·P, T_1 = B·P, T_2 = C·P, F_{c2} = D·P, where F_{c1} and F_{c2} represent the respective forces in the exterior and interior concrete strut, T_1 and T_2 represent the respective tension forces in the top and bottom longitudinal reinforcement, and P represents the point load acting on the beam (**Figure 2.8**).

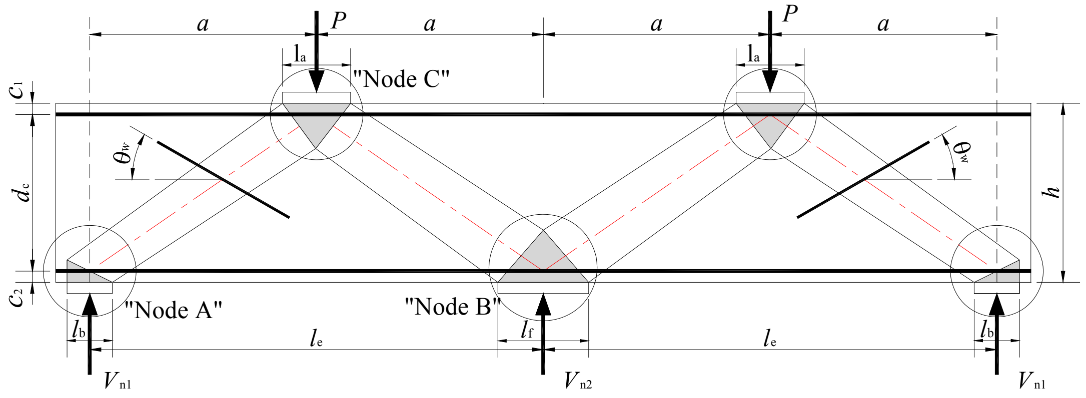

Figure 2.7 Two-span Continuous Deep Beam on Rigid Supports

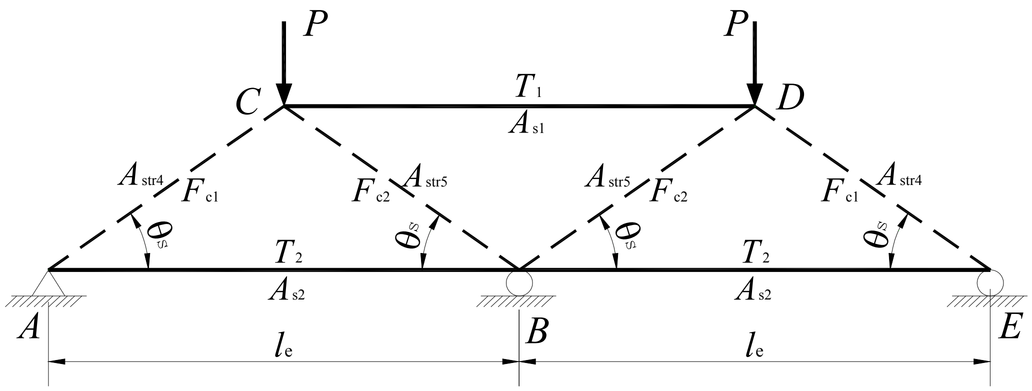

Figure 2.8 Truss model for two-span CDB on Rigid Supports

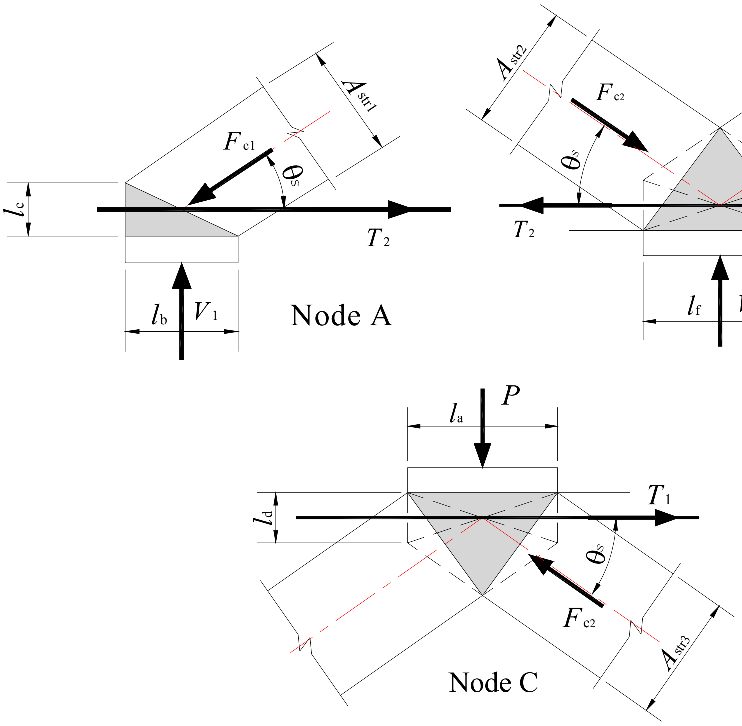

Figure 2.9 Details of nodal zones in CDB

Again, the Kupfer's linear interaction failure criterion is adopted at the interface between the strut and tension-compression nodal zones:

$$\frac{f_1}{f_t}+0.8\frac{f_2}{f_c'}=1 \tag{2.25}$$

Three tension-compression nodal zones A, B and C are identified in the STM for CDBs as shown in **Figure 2.7**. Similar to the modelling of SSDBs, Kupfer's failure criterion is applied to the three nodal zones, as follows:

Nodal zone A

The principal tensile stress f_{1A} across the diagonal strut and the principal compressive stress f_{2A} in the diagonal strut can be obtained in a similar manner as the SSDB:

$$f_{1A}=\frac{4T_2\sin\theta_s}{A_c/\sin\theta_s}=4C\sin^2\theta_s\cdot\frac{P}{A_c} \tag{2.26}$$

$$f_{2\mathrm{A}} = \frac{F_{\mathrm{c1}}}{A_{\mathrm{str1}}} = \mathrm{A} \cdot \frac{P}{A_{\mathrm{str1}}} \tag{2.27}$$

Where θ_s is the inclined angle of diagonal strut with respect to the horizontal, A_{str1} is the cross-sectional area at the bottom of the exterior concrete strut (**Figure 2.9**).

From Eqs. (2.25), (2.26) and (2.27), the following expression can be derived for the ultimate force P_{nA}:

$$P_{\mathrm{nA}} = \frac{1}{\dfrac{4\mathrm{C}\sin^2\theta_s}{f_{\mathrm{tA}} A_c} + \dfrac{0.8\mathrm{A}}{f_{\mathrm{c}}' A_{\mathrm{str1}}}} \tag{2.28}$$

Where f_{tA} is the maximum tensile capacity of nodal zone A in the f_1 direction and can be similarly expressed by:

$$f_{\mathrm{tA}} = \frac{4A_{\mathrm{s2}} f_{\mathrm{y}} \sin\theta_s}{A_{\mathrm{c}} / \sin\theta_s} + \frac{A_{\mathrm{sw}} f_{\mathrm{yw}} \sin(\theta_s + \theta_w)}{A_{\mathrm{c}} / \sin\theta_s} + f_{\mathrm{ct}}$$

Nodal zone B

The principal tensile stress $f_{1\mathrm{B}}$ across the diagonal strut at nodal zone B consists of two components: contribution from top and bottom reinforcement. As the k factor is -2 (compression) for top steel and 4 (tension) for bottom steel, the combined $f_{1\mathrm{B}}$ can be expressed as below

$$f_{1\mathrm{B}} = \frac{4T_2 \sin\theta_s - 2T_1 \sin\theta_s}{A_{\mathrm{c}} / \sin\theta_s} = (4\mathrm{C} - 2\mathrm{B})\sin^2\theta_s \cdot \frac{P}{A_{\mathrm{c}}} \tag{2.29}$$

The principal compressive stress at nodal zone B is obtained similarly as nodal zone A

$$f_{2\mathrm{B}} = \frac{F_{\mathrm{c2}}}{A_{\mathrm{str2}}} = \mathrm{D} \cdot \frac{P}{A_{\mathrm{str2}}} \tag{2.30}$$

where A_{str2} is the cross-sectional area at the bottom of the interior concrete strut (**Figure 2.9**).

From Eqs. (2.25), (2.29) and (2.30), the following expression can be derived for the ultimate load P_{nB}:

$$P_{\text{nB}} = \frac{1}{\dfrac{(4\text{C}-2\text{B})\sin^2\theta_s}{f_{\text{tB}}A_{\text{c}}} + \dfrac{0.8\text{D}}{f_{\text{c}}'A_{\text{str2}}}} \tag{2.31}$$

It is noteworthy that the maximum tensile capacity of nodal zone B f_{tB} is expressed by:

$$f_{\text{tB}} = \frac{4T_{2\max} - 2T_{1\text{a}}}{A_{\text{c}}/\sin^2\theta_s} + \frac{A_{\text{sw}}f_{\text{yw}}\sin(\theta_s+\theta_w)}{A_{\text{c}}/\sin\theta_s} + f_{\text{ct}}$$

where $T_{2\text{max}}$ is the yield strength of bottom steel and $T_{1\text{a}}$ is the corresponding tension force in the top steel at the yielding of bottom steel ($=\frac{\text{B}}{\text{C}}T_{2\max}$). The term $T_{1\text{a}}$ should not exceed the yield strength of top steel.

Nodal zone C

$$f_{1\text{C}} = \frac{4T_1\sin\theta_s - 2T_2\sin\theta_s}{A_{\text{c}}/\sin\theta_s} = (4\text{B}-2\text{C})\sin^2\theta_s \cdot \frac{P}{A_{\text{c}}} \tag{2.32}$$

$$f_{2\text{C}} = \frac{F_{\text{c2}}}{A_{\text{str3}}} = \text{D}\cdot\frac{P}{A_{\text{str3}}} \tag{2.33}$$

From Eqs. (2.25), (2.32), and (2.33), the following expression can be derived for the ultimate load P_{nC}:

$$P_{\text{nC}} = \frac{1}{\dfrac{(4\text{B}-2\text{C})\sin^2\theta_s}{f_{\text{tC}}A_{\text{c}}} + \dfrac{0.8\text{D}}{f_{\text{c}}'A_{\text{str3}}}} \tag{2.34}$$

The term f_{tC} in Eq. (2.34) is the maximum tensile capacity of nodal zone C:

$$f_{\text{tC}} = \frac{4T_{1\max} - 2T_{2\text{a}}}{A_{\text{c}}/\sin^2\theta_s} + \frac{A_{\text{sw}}f_{\text{yw}}\sin(\theta_s+\theta_w)}{A_{\text{c}}/\sin\theta_s} + f_{\text{ct}}$$

Similarly, $T_{1\text{max}}$ is the yield strength of top steel and $T_{2\text{a}}$ is the corresponding tension force in the bottom steel at the yielding of top steel ($=\frac{\text{C}}{\text{B}}T_{1\max}$). The value of $T_{2\text{a}}$ should not exceed the yield strength of bottom steel.

Thus the predicted ultimate load P will be the minimum among Eqs. (2.28), (2.31), and (2.34), denoted as P_n.

$$P_\mathrm{n} = \mathrm{Min}(P_\mathrm{nA}, P_\mathrm{nB}, P_\mathrm{nC}) \tag{2.35}$$

2.3.1 Reliability of STM for CDBs

The computing of STM for CDBs can be easily implemented by hand calculations or a spreadsheet. A worked example of hand calculations is shown in the Appendix B for illustrative purpose.

Fifty-four concrete continuous deep beams reported by other researchers have been evaluated by the author's model. The details of the specimens and the predicted-versus-actual ultimate strength ratios are summarized in **Table 2.2**. The beams had an overall depth h ranging from 400 to 1000 mm, and a l_e/d ratio from 0.95 to 4.49. The top-and-bottom longitudinal main reinforcement ratios ranged from 0.07 to 1.88% and 0.32 to 1.88%, respectively. The vertical and horizontal web reinforcement ratios ranged from zero to 0.90% and zero to 1.71%, respectively. The STM for CDBs generally performs well in predicting the ultimate strengths with an overall average prediction to test result of 0.87 and a C.O.V of 0.151. The ultimate strength P_n versus the experimental strength P_exp is plotted in **Figure 2.10**. Generally speaking, the proposed model is on the safe side and gives consistent predictions.

For simplicity, the model assumes linear material properties for steel and concrete when solving the statically-indeterminate truss. It is interesting to see the calculated middle support reactions fits reasonably well with the test results (**Table 2.3**). The fifty-four P_n/P_{exp} ratios obtained from the proposed model are plotted versus l_e/d ratio, concrete strength f_c', and total reinforcement ratio ρ_a in **Figure 2.11**. It is shown that the scatter is very low and uniform for the entire set of three variables. It can be concluded that the application of the modified STM to CDBs is feasible and successful. It also shows the validity and versatility of the proposed STM from simply-supported to continuous deep beams.

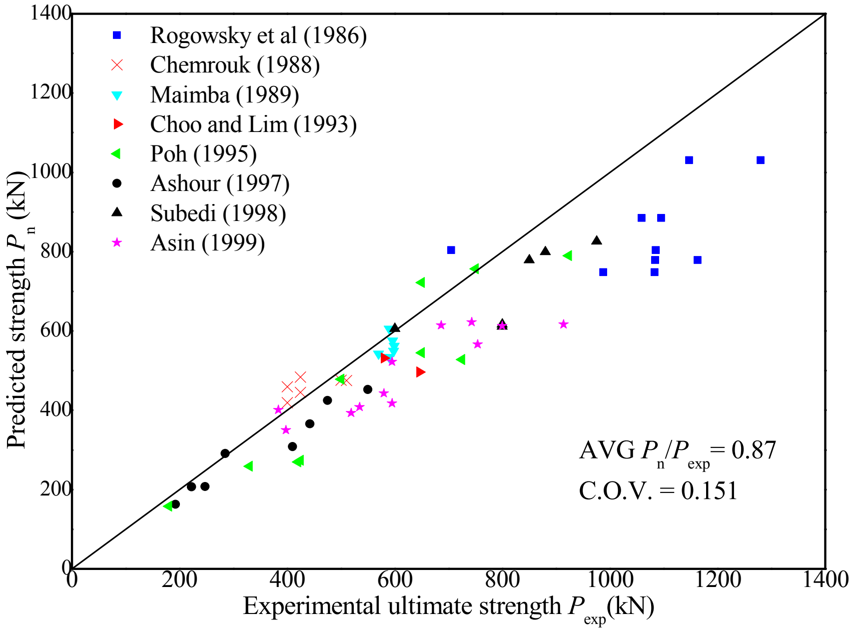

Figure 2.10 Ultimate strength predictions for 54 continuous deep beams

It is noteworthy that the overall average prediction-to-test result ratios for the 233 SSDBs and 54 CDBs are very close: 0.86 and 0.87, respectively, and the C.O.V. of both studies are coincidentally the same at 0.130. This shows that the predictions are consistent and accurate for both SSDBs and CDBs with different geometrical properties, concrete strengths and reinforcement configurations.

Table 2.2 Predictions of ultimate load for CDBs

No.	Beam Mark	f_c' (MPa)	h (mm)	b_w (mm)	l_e (mm)	f_yA_{s1}/f_yA_{s2} (kN / kN)	$f_{yv}A_v/f_{yh}A_h$ (kN / kN)	P_{exp} (kN)	P_n (kN) STM	P_n/P_{exp}
1	CD-0.5/V	40.4	960	47	860	163 / 163	43 / 0	400	419	1.05
2	CD-0.5/H	40.6	960	47	860	163 / 163	0 / 93	425	445	1.05
3	CD-0.5/I	45.1	960	47	860	163 / 163	(93)	500	476	0.95
4	CD-1.0/H	42.2	960	47	860	163 / 163	0 / 185	425	484	1.14
5	CD-1.0/I	41.0	960	47	860	163 / 163	(162)	510	475	0.93
6	CD-0.0	50.4	960	47	860	163 / 163	0 / 0	400	459	1.15
7	MC2-200	50.9	1000	40	860	15 / 314	23 / 42	598	550	0.92
8	MC2-150	48.4	1000	40	860	15 / 314	23 / 53	590	534	0.91
9	MC2-100	51.7	1000	40	860	15 / 314	23 / 87	599	562	0.94
10	MC2-75	53.1	1000	40	860	15 / 314	23 / 118	596	576	0.97
11	MC2-50	56.0	1000	40	860	15 / 314	23 / 182	590	606	1.03
12	MC2-75-2	48.8	1000	40	860	29 / 314	23 / 237	570	543	0.95
13	CDB1	30.0	625	120	1340	305 / 226	262 / 149	550	452	0.82
14	CDB2	33.1	625	120	1340	305 / 226	135 /74	475	425	0.90
15	CDB3	22.0	625	120	1340	305 / 226	0 / 74	285	291	1.02
16	CDB4	28.0	625	120	1340	305 / 226	135 / 0	443	366	0.83
17	CDB5	28.7	625	120	1340	113 / 113	135 / 74	410	308	0.75
18	CDB6	22.5	425	120	1340	192 / 192	139 / 39	248	208	0.84
19	CDB7	26.7	425	120	1340	192 / 192	72 / 20	223	207	0.93
20	CDB8	23.6	425	120	1340	113 / 113	72 / 20	193	163	0.85
21	BM 7/1.0(T1)	34.5	1000	200	2100	484 / 363	0 / 0	705	804	1.14
22	BM 7/1.0(T2)	34.5	1000	200	2100	484 / 363	0 / 0	1085	804	0.74
23	BM 6/1.0(T1)	35.8	1000	200	2100	484 / 363	0 / 194	1095	885	0.81
24	BM 6/1.0(T2)	35.8	1000	200	2100	484 / 363	0 / 194	1059	885	0.84
25	BM 5/1.0(T1)	36.9	1000	200	2100	484 / 363	518 / 0	1280	1030	0.80
26	BM 5/1.0(T2)	36.9	1000	200	2100	484 / 363	518 / 0	1147	1030	0.90
27	BM 4/1.0(T1)	28.5	1000	200	2100	456 / 342	0 / 65	1083	748	0.69
28	BM 4/1.0(T2)	28.5	1000	200	2100	456 / 342	0 / 65	988	748	0.76
29	BM 3/1.0(T1)	28.9	1000	200	2100	456 / 342	130 / 0	1084	779	0.72
30	BM 3/1.0(T2)	28.9	1000	200	2100	456 / 342	130 / 0	1163	779	0.67
31	HW	51.6	700	100	1400	338 / 225	0 / 247	646	496	0.77
32	VW	49.5	700	100	1400	338 / 225	330 / 0	580	532	0.92
33	N2-1.0-WO	36.9	600	150	1200	735 / 735	0 / 0	650	722	1.11
34	N2-1.0-WV	37.2	600	150	1200	735 / 735	162 / 0	750	757	1.01
35	N2-1.0-WVH	37.3	600	150	1200	735 / 735	162 / 216	923	790	0.86
36	N2-1.5-WO	33.9	600	150	1800	735 / 735	0 / 0	500	478	0.96
37	N2-1.5-WV	35.1	600	150	1800	735 / 735	206 / 0	725	528	0.73
38	N2-1.5-WVH	35.4	600	150	1800	735 / 735	206 / 165	650	545	0.84
39	2CB4	38.0	600	75	1680	116 / 323	182 / 114	420	270	0.64
40	2CB3	38.0	600	75	1680	323 / 323	182 / 114	425	274	0.64
41	1CB2	48.0	400	50	1000	99 / 99	48 / 29	180	158	0.88
42	1CB1	48.0	400	50	500	99 / 99	29 / 29	330	259	0.78
43	BM 1.0/1/1(r)	29.6	1000	150	2300	356 / 265	354 / 0	800	613	0.77
44	BM 1.0/1/2	27.5	1000	150	2300	356 / 265	257 / 0	754	566	0.75
45	BM 1.0/1/3	25.8	1000	150	2300	356 / 265	161 / 0	595	522	0.88
46	BM 1.0/2/1	25.2	1000	150	2300	265 / 356	354 / 0	914	617	0.67
47	BM 1.0/2/2	28.2	1000	150	2300	265 / 356	257 / 0	743	622	0.84
48	BM 1.0/2/3	30.4	1000	150	2300	265 / 356	161 / 0	686	614	0.89
49	BM 1.5/1/1	29.6	600	150	2300	445 / 356	354 / 0	595	418	0.70
50	BM 1.5/1/2	28.9	600	150	2300	445 / 356	257 / 0	519	393	0.76
51	BM 1.5/1/3	25.9	600	150	2300	445 / 356	161 / 0	398	350	0.88
52	BM 1.5/2/1	27.8	600	150	2300	356 / 445	354 / 0	580	443	0.76
53	BM 1.5/2/2	26.0	600	150	2300	356 / 445	257 / 0	535	408	0.76

54	BM 1.5/2/3	28.5	600	150	2300	356 / 445	161 / 0	384	401	1.05
									Mean	0.87
									S.D.	0.131
									C.O.V.	0.151

Note: Source — Specimens no. 1-6, Chemrouk 1988; 7-12, Maimba 1989; 13-20, Ashour 1997; 21-30, Rogowsky et al. 1986; 31-32, Choo and Lim 1993; 33-38, Poh 1995; 39-42, Subedi 1998; 43-54, Asin 1999.

Table 2.3 Comparison between calculated and measured middle support reaction

Beam Mark	Predicted interior support reaction X_n (kN)	Tested interior support reaction X_{exp} (kN)	X_n/X_{exp}
CDB1	577.2	702.0	0.82
CDB2	547.9	612.0	0.90
CDB3	367.9	360.4	1.02
CDB4	469.0	567.8	0.83
CDB5	387.8	516.0	0.75
CDB6	261.6	312.2	0.84
CDB7	260.3	281.0	0.93
CDB8	209.1	247.4	0.85
BM 7/1.0(T1)	960.2	842.0	1.14
BM 7/1.0(T2)	1019.6	1376.0	0.74
BM 6/1.0(T1)	1035.8	1281.0	0.81
BM 6/1.0(T2)	991.6	1186.0	0.84
BM 5/1.0(T1)	1400.7	1741.0	0.80
BM 5/1.0(T2)	1338.7	1491.0	0.90
BM 4/1.0(T1)	918.7	1330.0	0.69
BM 4/1.0(T2)	929.8	1228.0	0.76
BM 3/1.0(T1)	987.9	1374.0	0.72
BM 3/1.0(T2)	1032.0	1540.0	0.67
HW	636.0	828.0	0.77
VW	665.4	726.0	0.92
N2-1.0-WO	937.2	844.0	1.11
N2-1.0-WV	944.5	936.0	1.01
N2-1.0-WVH	988.8	1156.0	0.86
N2-1.5-WO	523.6	548.0	0.96
N2-1.5-WV	645.4	887.0	0.73
N2-1.5-WVH	717.2	856.0	0.84
BM 1.0/1/1(r)	806.8	1053.0	0.77
BM 1.0/1/2	742.2	989.0	0.75
BM 1.0/1/3	681.4	776.0	0.88
BM 1.0/2/1	790.3	1171.0	0.67
BM 1.0/2/2	784.9	937.0	0.84
BM 1.0/2/3	756.1	845.0	0.89
BM 1.5/1/1	561.2	798.0	0.70
BM 1.5/1/2	526.1	694.0	0.76
BM 1.5/1/3	607.4	691.0	0.88
BM 1.5/2/1	568.7	745.0	0.76
BM 1.5/2/2	515.3	675.0	0.76
BM 1.5/2/3	521.5	499.0	1.05
mean			0.84
S.D.			0.116
C.O.V.			0.138

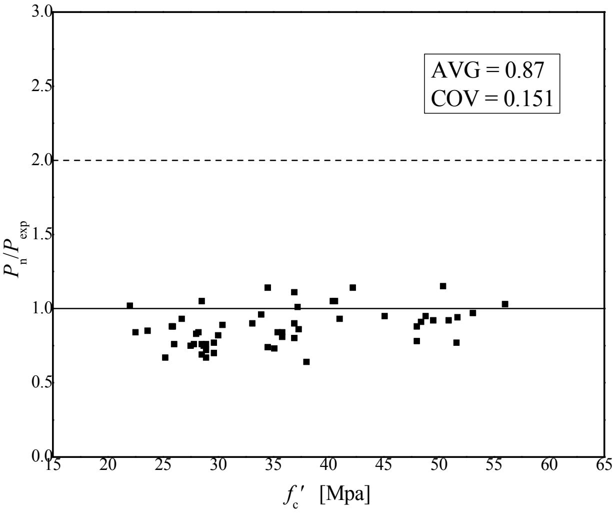

(a) concrete strength f_c'

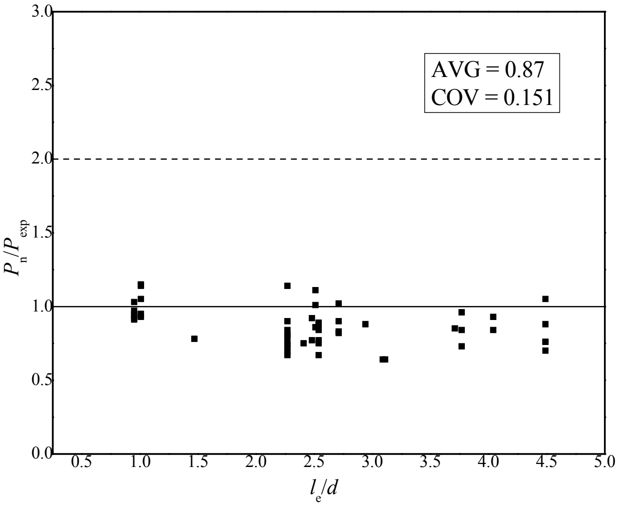

(b) effective span to overall depth ratio l_e/d

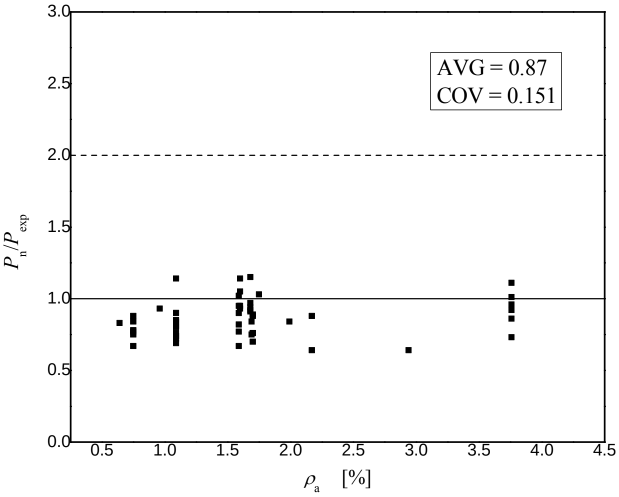

(c) total reinforcement ratio ρ_a

Figure 2.11 Effect of: (a) concrete strength; (b) effective span to overall depth ratio; and (c) total reinforcement ratio on ultimate strength predictions.

2.4 Modelling CDBs on Spring Supports

In Section 2.2 and 2.3, the modified STM on SSDBs is developed to achieve better prediction accuracy and consistency and is successfully extended to CDBs with rigid supports. To consider the effect of differential settlement between the middle and end supports of a CDB as shown in **Figure 2.12**, one spring with stiffness $K = V_{n2}/\Delta$ is added below the middle support B of the statically indeterminate truss (**Figure 2.13**). The term Δ denotes the differential settlement of the middle support over the end supports. Assuming bilinear elastic-plastic material properties for concrete struts and steel bars, the reaction force of middle support is solved and denoted as $X = \Gamma \cdot P$, where Γ is a support reaction factor. Detailed derivations are included in Appendix C. Hence, the member forces of the model with a spring middle support can be expressed as follows:

$$F_{c1} = \left(1 - \frac{\Gamma}{2}\right) \cdot \frac{P}{\sin\theta_s} \tag{2.36}$$

$$F_{c2} = \frac{\Gamma}{2} \cdot \frac{P}{\sin\theta_s} \tag{2.37}$$

$$T_1 = (\Gamma - 1) \cdot \frac{P}{\tan\theta_s} \tag{2.38}$$

$$T_2 = \left(1 - \frac{\Gamma}{2}\right) \cdot \frac{P}{\tan\theta_s} \tag{2.39}$$

where F_{c1} and F_{c2} represent the respective force in the exterior and interior diagonal struts (**Figure 2.13**a), T_1 and T_2 represent the respective tension forces in the top and bottom longitudinal reinforcement, P represents the point load acting on the beam, and θ_s is the inclined angle of diagonal strut with respect to the horizontal.

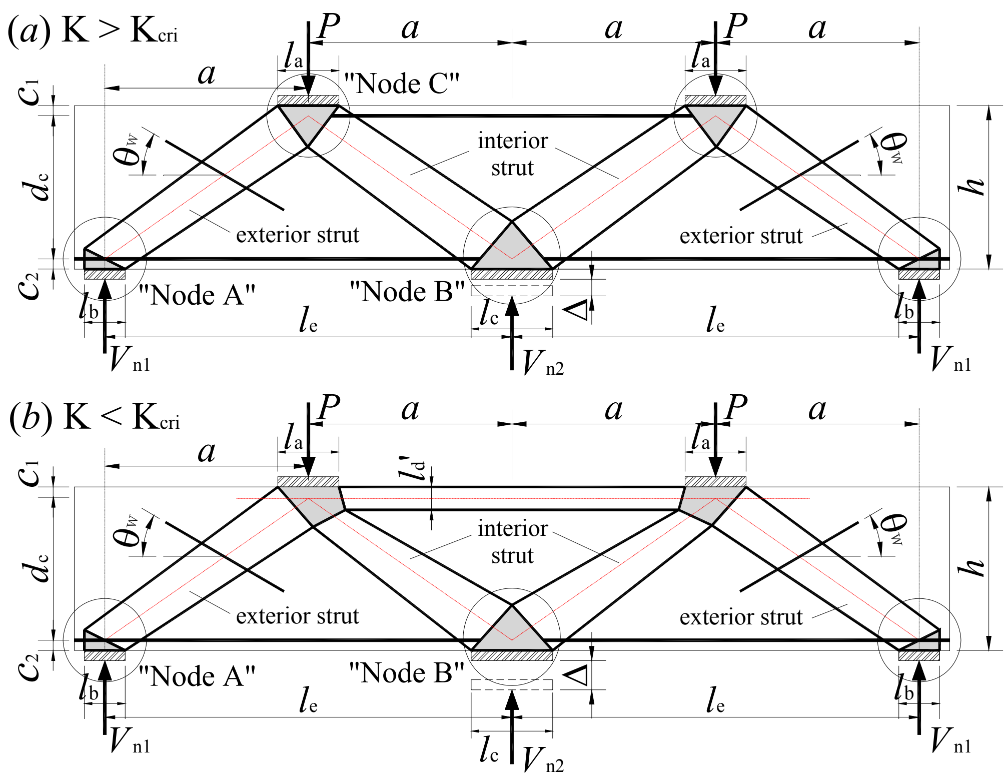

Figure 2.12 Two-span CDB with support settlement

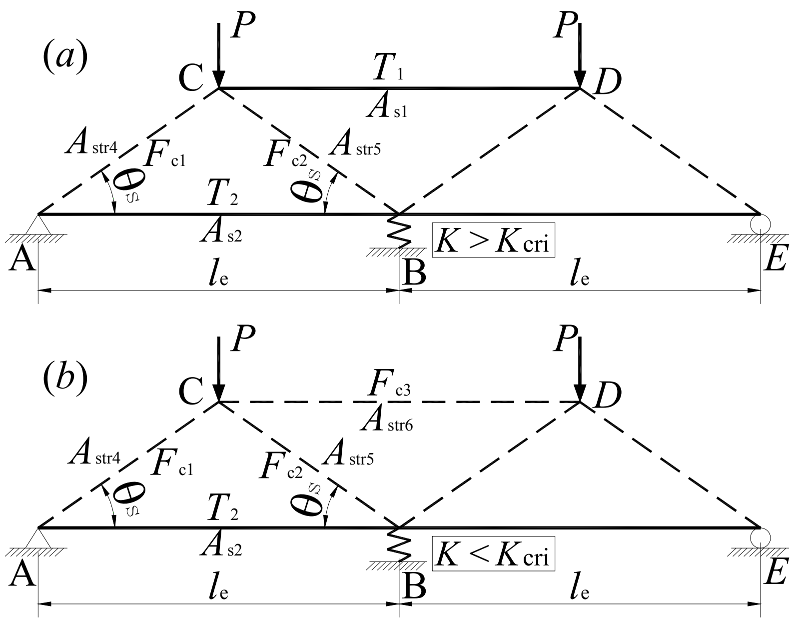

Figure 2.13 Truss models for two-span CDB on elastic supports

There are two scenarios to be considered, viz. the middle support stiffness K is greater or smaller than a threshold value K_{cri}. Although the middle support settles under loading, it is sufficiently rigid to effect hogging moment over the middle support.

Consequently, the top member of the truss is in tension and acts as a tie (**Figure 2.12**a and **Figure 2.13**a). However, if K is smaller than K_{cri}, the middle support settles considerably due to its low stiffness, and a sagging moment is present over the middle support. Therefore, the top of the beam is in compression, represented by a top horizontal concrete strut in the truss model (**Figure 2.12**b and **Figure 2.13**b). The threshold value of middle support stiffness K_{cri} is termed *critical support stiffness*. It can be determined by equating tie force T_1 in Eq. (2.38) to zero:

$$K_{cri} = \frac{4E_c A_{str5} \cos\theta_s \sin^2\theta_s}{\left(m+2p\cos^3\theta_s-1\right)l_e} \tag{2.40}$$

Where E_c is the modulus of concrete, A_{str5} is the average cross-sectional area of interior strut, l_e is the beam effective span (**Figure 2.12**), and m and p are ratios of axial stiffness of truss members. Details of these terms are included in Appendix A.

For calculating the maximum force P, Kupfer's linear interaction failure criterion is adopted at the interface between the strut and tension-compression nodal zones:

$$\frac{f_1}{f_t} + 0.8\frac{f_2}{f_c'} = 1 \tag{2.41}$$

When $K > K_{cri}$ (Case I), three different tension-compression nodal zones (A, B and C) are identified in the model as shown in **Figure 2.12**a. Similar to the procedure of modelling CDBs with rigid supports in Section 3 of this chapter, Kupfer's failure criterion is applied to the three tension-compression nodal zones (**Figure 2.9**) and the ultimate load determined from each nodal zone can be obtained as follows:

Nodal zone A

$$P_{\mathrm{nA}} = \frac{1}{\dfrac{(2-\Gamma)\sin 2\theta_s}{f_{\mathrm{tA}} A_c} + \dfrac{0.8(2-\Gamma)}{2 f_{\mathrm{c}}' A_{\mathrm{str1}} \sin\theta_s}} \tag{2.42}$$

$$f_{\mathrm{tA}} = \frac{4A_{\mathrm{s2}} f_{\mathrm{y}} \sin\theta_s}{A_{\mathrm{c}} / \sin\theta_s} + \frac{A_{\mathrm{sw}} f_{\mathrm{yw}} \sin(\theta_s + \theta_w)}{A_{\mathrm{c}} / \sin\theta_s} + f_{\mathrm{ct}}$$

Nodal zone B

$$P_{\mathrm{nB}} = \frac{1}{\dfrac{(3-2\Gamma)\sin 2\theta_s}{f_{\mathrm{tB}} A_{\mathrm{c}}} + \dfrac{0.8\Gamma}{2 f_{\mathrm{c}}' A_{\mathrm{str2}} \sin\theta_s}} \tag{2.43}$$

$$f_{\mathrm{tB}} = \frac{4T_{2\max} - 2T_{1\mathrm{a}}}{A_{\mathrm{c}} / \sin^2\theta_s} + \frac{A_{\mathrm{sw}} f_{\mathrm{yw}} \sin(\theta_s + \theta_w)}{A_{\mathrm{c}} / \sin\theta_s} + f_{\mathrm{ct}}$$

Nodal zone C

$$P_{\mathrm{nC}} = \frac{1}{\dfrac{(5\Gamma/2-3)\sin 2\theta_s}{f_{\mathrm{tC}} A_{\mathrm{c}}} + \dfrac{0.8\Gamma}{2 f_{\mathrm{c}}' A_{\mathrm{str3}} \sin\theta_s}} \tag{2.44}$$

$$f_{\mathrm{tC}} = \frac{4T_{1\max} - 2T_{2\mathrm{a}}}{A_{\mathrm{c}} / \sin^2\theta_s} + \frac{A_{\mathrm{sw}} f_{\mathrm{yw}} \sin(\theta_s + \theta_w)}{A_{\mathrm{c}} / \sin\theta_s} + f_{\mathrm{ct}}$$

Where A_{c} is the effective cross-sectional area of the deep beam; A_{str1}, A_{str2} and A_{str3} are the cross-sectional areas of concrete struts as illustrated in **Figure 2.9**, given by Eqs. (A.2) - (A.4) in Appendix A; $T_{1\max}$ and $T_{2\max}$ are the respective yield force of top and bottom steel reinforcement; $T_{1\mathrm{a}} = \frac{T_1}{T_2} T_{2\max}$ and $T_{2\mathrm{a}} = \frac{T_2}{T_1} T_{1\max}$ are the tension force in the top steel at the yielding of bottom steel and tension force in the bottom steel upon yielding of top steel, respectively; $T_{1\mathrm{a}}$ and $T_{2\mathrm{a}}$ should not exceed the respective yield strength of top and bottom reinforcement.

The predicted ultimate strength will be the minimum among Eqs. (2.42), (2.43) and (2.44) for the respective nodal zone A, B and C, denoted as P_{n}.

$$P_{\mathrm{n}} = \mathrm{Min}(P_{\mathrm{nA}}, P_{\mathrm{nB}}, P_{\mathrm{nC}}) \tag{2.45}$$

When K < K_{cri} (Case II), the top tie transforms to a compression strut, thus nodal zone C experiences a compression-compression stress state, so the failure load is governed by the compression-tension nodal zones at A and B only (**Figure 2.12**b). Thus, no further consideration is given to nodal zone C. The depth of top concrete strut l_{d}' (**Figure 2.12**b) is assumed to be equal to the effective depth of upper nodal zone l_{d} (**Figure 2.9**). The support reaction factor Γ can be similarly obtained from Eq. (C.3), except that the ratio n is substituted by n' as follows:

$$n' = \frac{E_{\mathrm{c}} A_{\mathrm{str5}}}{E_{\mathrm{c}} A_{\mathrm{str6}} + E_{\mathrm{s}} A_{\mathrm{s1}}} \tag{2.46}$$

where A_{str6} (= $l_{\mathrm{d}} b_{\mathrm{w}}$) is the cross-sectional area of top concrete strut. After obtaining the member forces of STM, failure load P_{n} can be predicted by applying Eq. (2.41) to nodal zones A and B in a similar fashion and by adopting the smaller value of the two.

$$P_{\mathrm{n}} = \mathrm{Min}(P_{\mathrm{nA}}', P_{\mathrm{nB}}') \tag{2.47}$$

where $P_{\mathrm{nA}}' = P_{\mathrm{nA}}$ as in Eq. (2.42), and P_{nB}' is expressed as below:

$$P_{\mathrm{nB}}' = \frac{1}{\dfrac{(2-\Gamma)\sin 2\theta_s}{f_{\mathrm{tB}}' A_{\mathrm{c}}} + \dfrac{0.8\Gamma}{2 f_{\mathrm{c}}' A_{\mathrm{str2}} \sin\theta_s}} \tag{2.48}$$

where f_{tB}' is the corresponding tensile capacity of nodal zone B:

$$f_{\mathrm{tB}}' = \frac{4T_{2\max}}{A_{\mathrm{c}} / \sin^2\theta_s'} + \frac{A_{\mathrm{sw}} f_{\mathrm{yw}} \sin(\theta_s' + \theta_w)}{A_{\mathrm{c}} / \sin\theta_s'} + f_{\mathrm{ct}}$$

In summary, the steps for direct calculation of ultimate strength P_n of CDB are summarised as follows:

Step 1 Determine θ_s from Eqs. (A.7);

Step 2 Determine m, n, p, ξ from Eqs. (C.4) - (C.7);

Step 3 Determine Γ and K_{cri} from Eqs. (C.3) and (2.40), respectively;

Case I: $\mathrm{K} > K_{\mathrm{cri}}$

Step 4 Determine P_{nA}, P_{nB} and P_{nC} from Eqs. (2.42), (2.43) and (2.44), respectively;

Step 5 Determine the ultimate load P_{n} from Eq. (2.45).

Case II: $\mathrm{K} < K_{\mathrm{cri}}$

Step 4 Determine P_{nA}' and P_{nB}' from Eqs. (2.42) and (2.48), respectively;

Step 5 Determine the ultimate load P_{n} from Eq. (2.47).

In the extreme case when K = 0, the two-span CDB reduces to single span and the support reaction factor $\Gamma = 0$. Correspondingly, in the STM, the interior diagonal struts (A_{str5}) vanish and the tension-compression nodal zone C no longer exists. Thus, the member forces (Eqs. (2.36) - (2.39)) are reduced to:

$$F_{\mathrm{c1}} = \frac{P}{\sin\theta_s}$$

$$F_{\mathrm{c2}} = 0$$

$$T_1 = -\cot\theta_s P$$

$$T_2 = \cot\theta_s P$$

Hence, the proposed STM for CDBs is identical to the one proposed for SSDBs in Section 2.

It is interesting to note, as shown in Appendix C, that when K is infinite, i.e. there is no relative settlement between the supports, the proposed STM will reduce to the CDB model comprising three perfectly rigid supports as developed in Section 3.

2.5 Asymmetrically Loaded SSDB

2.5.1 Model Geometry

Figure 2.14 shows a simply supported deep beam (SSDB) subjected to unequal and unsymmetrical two-point loading P_1 and P_2. The shorter and longer shear span are denoted as a and c, respectively. It should be noted that the top strut is no longer horizontal but inclines an angle θ to maintain force equilibrium of the truss.

The inclination angle θ can be derived from geometry and statics (Details can be referred to Appendix D):

$$\tan\theta = \begin{cases} \dfrac{h-d_3-l_c/2}{\Pi-l_a/2} & (\Pi>0) \\[2ex] \dfrac{h-d_3-l_c/2}{\Pi-b+l_a/2} & (\Pi<0) \end{cases} \tag{2.49}$$

where d_3 = the distance from the beam soffit to the centroid of bottom longitudinal reinforcement (**Figure 2.14**); l_c = the equivalent depth of the top nodal zone A; b = the distance between two loads; l_a = the width of the load plate.

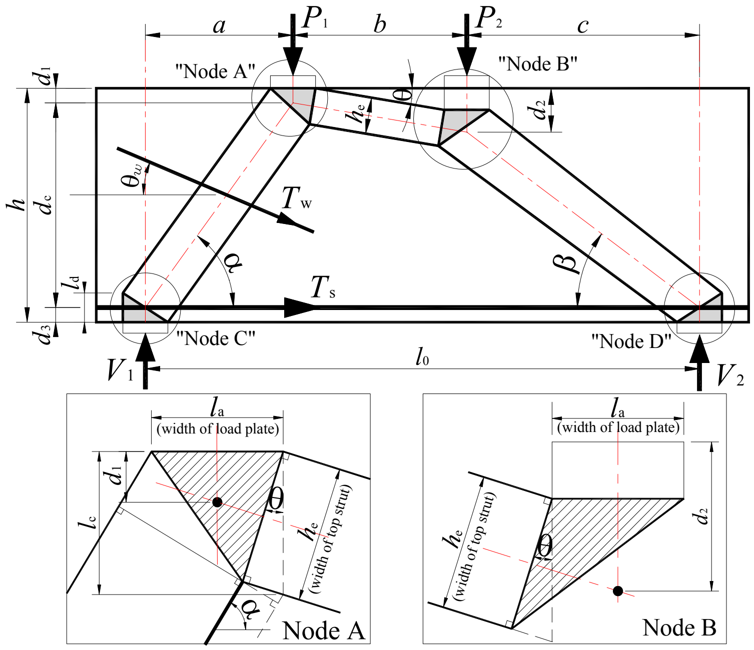

Figure 2.14 SSDB under unequal/unsymmetrical loading

Π is a load parameter containing the relevant information of both load inequality ($n_L = P_1/P_2$) and load asymmetry ($m_L = c/a$):

$$\Pi = \frac{n_L}{n_L - m_L} l_0 - a \tag{2.50}$$

When load inequality equals to load asymmetry, i.e. $n_L = m_L$, Π goes to infinity and θ equals to zero, which indicates that the top strut aligns to the horizontal. One such situation is when the beam is subjected to two symmetrical and equal point loads, i.e. $n_L = 1$, $m_L = 1$, thus $\Pi = \infty$, and the STM is balanced with zero inclination of the top strut (**Figure 2.15 (c)**). When load inequality (LI) n_L approaches infinity (that is, $P_1 \gg P_2$), $\tan\theta = d_c/(b + c)$. This means that the top strut AB and right diagonal strut BD join together as one straight line, i.e. θ = β. Thus the model is simplified to the case of single point load P_1 acting on the beam (**Figure 2.15(d)**). This is reasonable as the point load P_2 becomes insignificant when compared to P_1 as n_L grows larger.

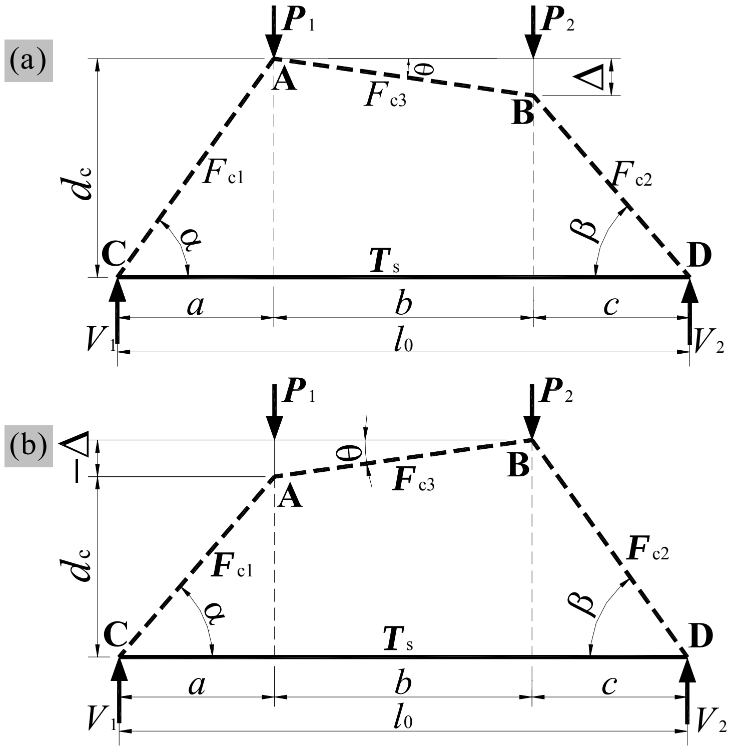

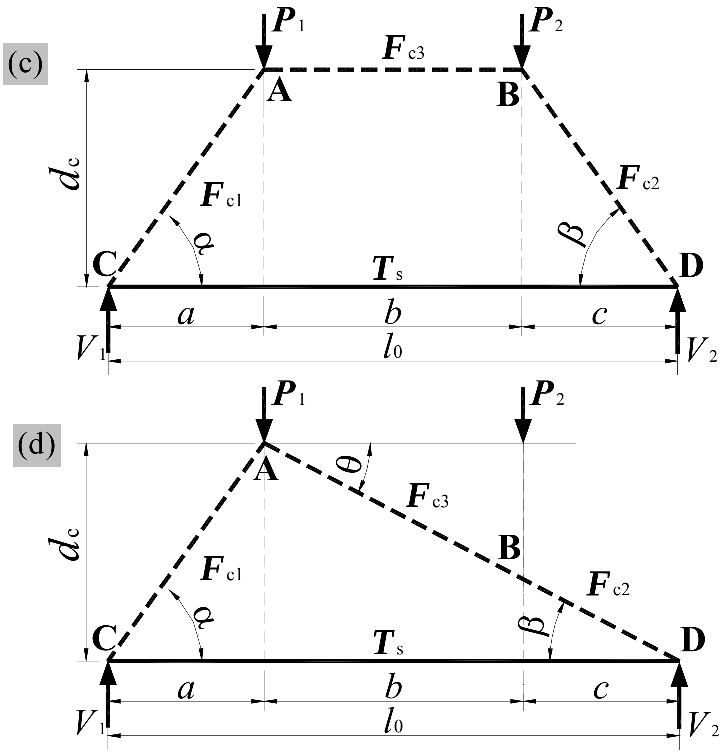

Figure 2.15 Truss model for SSDBs under unequal/unsymmetrical loadings
(a) Π > 0 (b) Π < 0 (c) Π = ∞ (d) Π = b + c

2.5.2 STM Modelling

From the equilibrium of bottom node C, the force in the concrete strut is (**Figure 2.14**):

$$F_{c1} = \frac{V_1}{\sin a} \tag{2.51}$$

The force in the bottom tension tie is:

$$T_s = \frac{V_1}{\tan a} \tag{2.52}$$

To determine the principal tensile stress f_1 perpendicular to the diagonal strut due to the main steel tensile force T_s at the nodal zone, it is necessary to assume the concrete stress distribution along the concrete strut arising from T_s. Linear approximation of stress distribution is adopted as it has been shown sufficiently accurate for determining the beam ultimate strength in section 2. The principal tensile stress f_1 can be obtained from considering moment and force equilibrium between the bottom steel force and its assumed stress distribution along the diagonal strut, as below:

$$f_1 = \frac{4T_s \sin a}{A_c / \sin a} \tag{2.53}$$

where A_c is the effective cross-sectional area of a deep beam; T_s is the force in the bottom steel; α is the inclined angle of the left diagonal strut with respect to horizontal line. The stress distribution due to evenly distributed web reinforcement can be similarly assumed.

The principal compressive stress f_2 in the direction of the diagonal strut at the bottom nodal zone C can be computed from:

$$f_2 = \frac{F_{c1}}{A_{\mathrm{str}}} \tag{2.54}$$

where $A_{\mathrm{str}} = b_w(l_d \cos\alpha + l_b \sin\alpha)$ is the cross-sectional area of the concrete diagonal strut. The bottom nodal zone C experiences a bi-axial tension-compression stress state, and the compressive strength of concrete is reduced due to the softening effect of the transverse tensile stress. It is shown in the experimental observation that there exists an interactive relationship between compression and tension forces in the beam web region. Thus, it lends experimental support for adopting Kupfer's interactive failure criterion (Eq. (2.1)) in the model. Combining Eqs. (2.1) and (2.51)-(2.54), the shear strength V_1 for unequally-loaded SSDB is expressed as below:

$$V_1 = \frac{1}{\dfrac{4\sin\alpha\cos\alpha}{A_{\mathrm{c}} f_{\mathrm{t}}} + \dfrac{0.8}{A_{\mathrm{str}} f_{\mathrm{c}}' \sin\alpha}} \tag{2.55}$$

where the composite tensile strength f_t is given by

$$f_{\mathrm{t}}=\frac{4f_{\mathrm{y}}A_{\mathrm{s}}\sin\alpha}{A_{\mathrm{c}}/\sin\alpha}+\frac{f_{\mathrm{yw}}A_{\mathrm{sw}}\sin(\alpha+\theta_{w})}{A_{\mathrm{c}}/\sin\alpha}+f_{\mathrm{ct}} \tag{2.56}$$

The term f_{ct} in Eq. (2.56) represents the contribution from tensile strength of cracked concrete.

The total ultimate load F_{u} can be obtained by:

$$F_{u}=\frac{(n+1)l_{0}}{nb+nc+c}V_{1} \tag{2.57}$$

However, the ultimate shear force V_1 cannot be determined directly since l_{c} (Eq. (2.49)) is initially unknown and the accurate values of angle θ and α need to be determined through an iterative procedure.

On the other hand, from horizontal force equilibrium of top nodal zone A,

$$F_{\mathrm{c3}}\cos\theta=V_{1}\cot\alpha \tag{2.58}$$

where F_{c3} is the compression force in the top concrete strut (**Figure 2.15**). The author suggests that the compressive stress in the bi-compression nodal zone should not exceed f_{c}'.

$$F_{\mathrm{c3}}=f_{\mathrm{c}}'b_{\mathrm{w}}h_{\mathrm{e}}=f_{\mathrm{c}}'b_{\mathrm{w}}l_{\mathrm{c}}\cos\theta \tag{2.59}$$

From Eqs. (2.58) and (2.59), the equivalent depth l_{c} of the nodal zone A can be expressed as follows:

$$l_{\mathrm{c}}=\frac{V_{1}}{b_{\mathrm{w}}f_{\mathrm{c}}'\tan\alpha\cos^{2}\theta} \tag{2.60}$$

Through Eqs. (2.49), (2.55) and (2.60), an iterative procedure is mobilized to determine the ultimate shear strength. In practice, iteration can begin by assuming the initial l_{c} equal to l_{d} (**Figure 2.14**). The convergence is very rapid with only 3 or 4 iterations. The iterative procedure is illustrated in **Figure 2.16**.

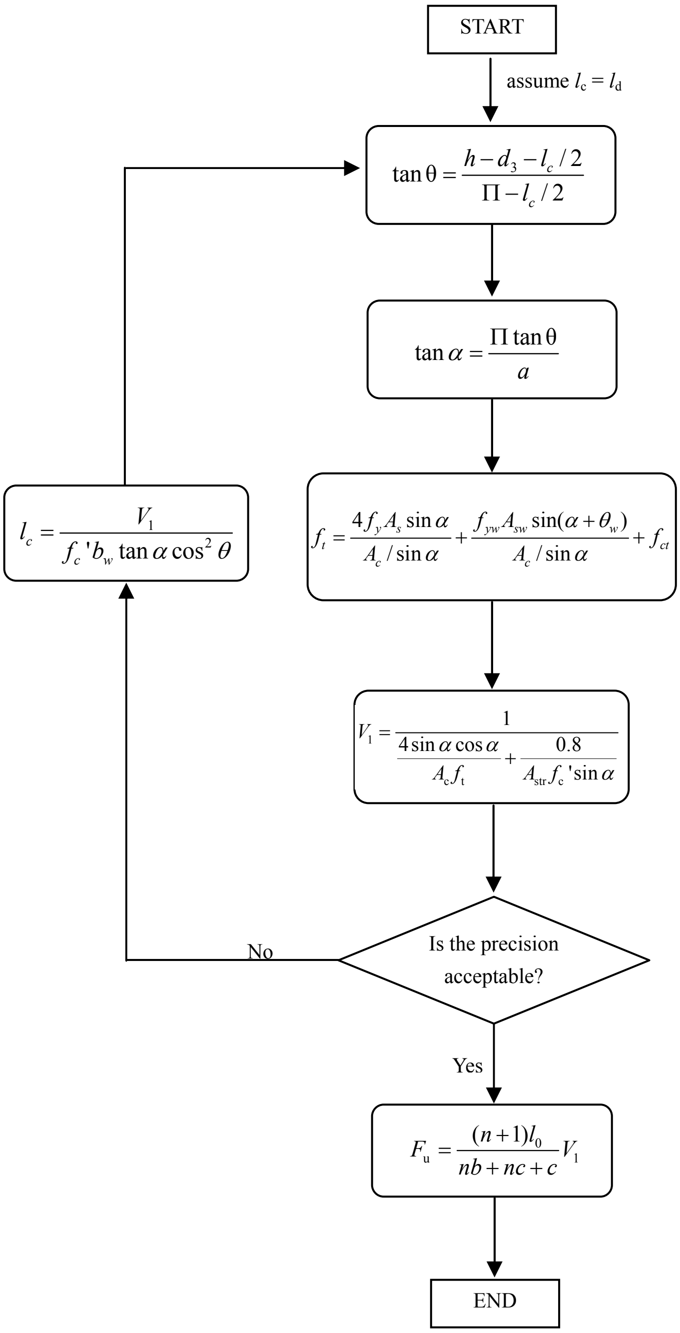

Figure 2.16 Iteration procedures for computing ultimate strength of SSDBs

2.5.3 Predicting Failure Mode

This section describes how the modified STM can be used to predict the failure modes of specimens. The Kupfer's failure criterion (Eq. (2.1)) in terms of stress ratios can be rewritten as follows:

$$v_t + 0.8v_c = 1 \tag{2.61}$$

where v_c and v_t are the compressive and tensile stress ratios, respectively, expressed by

$$v_t = \frac{f_1}{f_t} \tag{2.62}$$

and

$$v_c = \frac{f_2}{f_c'} \tag{2.63}$$

Eq. (2.61) embodies an interaction between two orthogonal stresses, i.e. compressive stress causing concrete crushing and tension stress causing diagonal splitting.

Normally, deep beams exhibit combined failure modes. The author argues that when one of the two failure modes becomes dominant, the corresponding stress ratio is significantly increased. For instance, for a deep beam that fails predominantly in diagonal splitting mode, tensile stress ratio far exceeds compressive stress ratio, whereas in a shear-compression failure mode the converse is true. That is to say, the closer the principal tensile stress is to the composite tensile strength (represented by a high value of v_t), the more likely the beam may fail in that mode, and vice versa. Thus, one can expect to see crushing of concrete for beams with high v_c, and diagonal splitting for high v_t. Through determining either the value of v_t or v_c (since they are related by Eq. (2.61)) the proposed model has the capability to predict the failure mode.

Substituting Eqs. (2.51) - (2.55) into Eqs. (2.62) and (2.63), we have:

$$v_t = \frac{\omega}{1+\omega} \tag{2.64}$$

$$v_c = \frac{1}{0.8(1+\omega)} \tag{2.65}$$

where

$$\omega = 0.25 + \frac{5\sin^2 a \cos a A_{\mathrm{str}} f_{\mathrm{c}}^{'}}{A_{\mathrm{c}} f_{\mathrm{t}}} \tag{2.66}$$

It is helpful to determine a threshold value of stress ratio which delineates the boundary between the two failure modes. Such a threshold may be obtained from a statistical analysis of experimental results. The author analyzed a selected group of deep beams (Subedi 1986, 1988; Tan et al 1997; Oh and Shin 2001) including the author's specimens with *a*/*d* ratios ranging from 0.45 to 2.11. For simplicity, the failure modes of the beams are reduced to 2 major categories: a) failure dominated by tensile stress, which includes diagonal splitting, shear tension and shear flexure; b) failure dominated by compressive stress, which includes shear compression and crushing of strut. The former failure mode is less explosive, marked by limited ductility when there is sufficient web reinforcement, whereas the latter failure mode is usually accompanied by a loud "bang", with an abrupt drop in loading. The beams are plotted using calculated tensile stress ratios v_{t} against *a*/*d* (**Figure 2.17**). From the figure and observed failure modes of the published test specimens, it appears that an appropriate threshold value between the two failure modes is around $v_{\mathrm{t}} = 0.75$. It should be noted that for v_{t} greater than 0.75, the failure mode will shift towards diagonal splitting, and vice versa. At or around the threshold value, the beam may fail in a mixed mode, viz. diagonal splitting with shear compression. And the further v_{t} is from the threshold value, the more distinct is the corresponding beam failure mode.

It is worth noting that the statistical threshold value of v_{t} is greater than 0.5. This bias means that even if a beam apparently fails in compression-dominated mode, the tensile stress ratio usually exceeds the compressive stress ratio, although in terms of total force, the compression component is always greater than tension component.

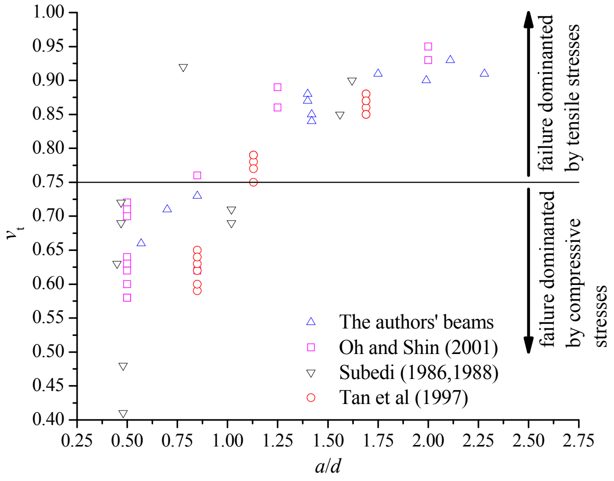

Figure 2.17 Tensile stress ratios v_t related with failure modes of specimens.

It suggests that for failure to take place, the tensile stress ratio must attain a certain level. This is supported by the fact that transverse tensile stress always occurs along with compressive stress in the concrete strut. Thus, it is unlikely that a deep beam can fail in purely compression mode without the tensile stress developing to a certain level.

2.6 STM Incorporating Size Effect Causes

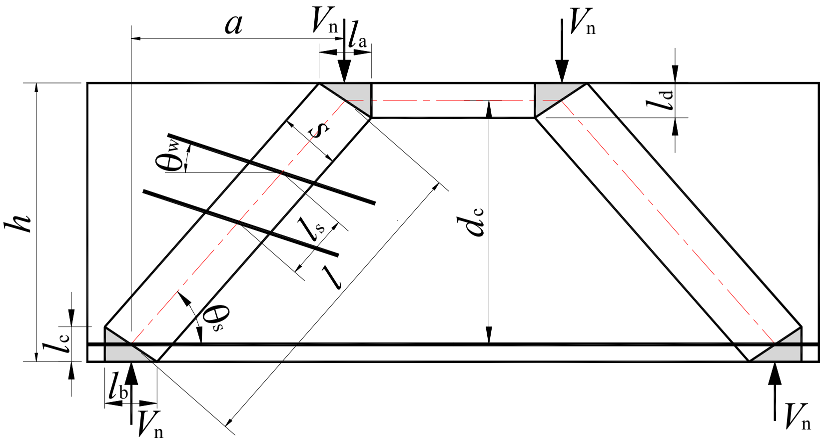

Figure 2.18 Strut-and-tie model for SSDB

In Section 2, below expression for V_n has been proposed for SSDBs:

$$V_n = \frac{1}{\dfrac{2\sin 2\theta_s}{f_\text{t} A_\text{c}} + \dfrac{0.8}{f_\text{c}' A_\text{str} \sin\theta_s}} \tag{2.67}$$

where θ_s is the inclined angle of the diagonal strut (**Figure 2.18**); f_c' is the cylinder compressive strength; A_c is the cross-sectional area of the deep beams; A_str is the cross-sectional area of the diagonal strut and f_t is the maximum tensile capacity of the bottom nodal zone computed as:

$$f_\text{t} = \overset{\text{Main longitudinal steel}}{\frac{4A_s f_\text{y} \sin\theta_s}{A_\text{c}/\sin\theta_s}} + \overset{\text{Web steel}}{\sum \frac{f_\text{yw} A_\text{sw} \sin(\theta_s + \theta_w)}{A_\text{c}/\sin\theta_s}} + \overset{\text{Cracked concrete tensile strength}}{0.31\sqrt{f_\text{c}'}\left(\frac{\varepsilon_\text{cr}}{\varepsilon_1}\right)^{0.4}} \tag{2.68}$$

where A_s and A_sw are the respective total areas of longitudinal and web reinforcement; f_y and f_yw are the respective yield strengths of longitudinal and web reinforcement; θ_w is the inclined angle of web reinforcement with respect to horizontal line (**Figure 2.18**).

It was argued (Kotsovos and Pavlovic 1997, 2004, Tan and Cheng 2006, Tan et al 2008) that the conventional definition of the ultimate shear strength of $V/(bd)$ as indicative of size effect is inappropriate for concrete deep beams. This equation originating from steel beams, with more-or-less uniform shear flow in the steel web, does not reflect the arch action in a deep beam. It is believe that this is the primary cause of size effect (Tan and Cheng 2006). It was found that after the formation of diagonal cracks, the ultimate shear strengths of deep beams depend on the arch capacity (Tan et al 2005). However, the arch capacity largely depends on the geometry and boundary conditions of diagonal strut. Tan and Cheng (2006) defined these variations as the secondary causes of size effect and modified the concrete strength at nodal zone to vf_c' to take account of these causes. The term v was the efficiency factor and taken as the product of ξ and ζ, where ξ accounts for the effect of *strut geometry* and ζ for the effect of *strut boundary condition* influenced by web reinforcement. These two parameters are expressed as follows:

$$\xi = 0.8 + \frac{0.4}{\sqrt{1+(l-s)/50}} \tag{2.69}$$

$$\zeta = 0.5 + \sqrt{\frac{kd_s}{l_s}} \le 1.2 \tag{2.70}$$

where l and s are the strut length and width, respectively (**Figure 2.18**); the larger the strut length l, the more slender is the strut and the smaller is the value of ξ. The term d_s is the diameter of web steel bar; when web steel is not provided, d_s is taken as the minimum diameter of bottom longitudinal steel bars; $k = \frac{1}{2}\sqrt{\frac{\pi f_y}{f_{ct}}}$ is a material factor incorporating steel bar yield strength f_y and concrete tensile strength f_{ct}; when web steel is not provided, it is taken as half of the above value; l_s is the maximum spacing of web steel intercepted by the inclined strut.

Hence, the author proposes the following equation for ultimate shear strength, taking account of size effect:

$$V_n = \frac{1}{\dfrac{2\sin 2\theta_s}{f_t A_c} + \dfrac{0.8}{vf_c' A_{str} \sin\theta_s}} \tag{2.71}$$

By configuring the loading and support plate width w_e proportional to the beam size, the widths of diagonal strut and bottom nodal zone also increase accordingly. The modified STM indicates that, if the strut geometry (determined by plate width) and strut boundary conditions (determined by web reinforcement) are kept proportionally constant for different beam sizes, then the size effect will be dramatically mitigated or even eliminated. That is to say, the ultimate beam shear strength does not reduce as the beam size h increases proportionally. It is also interesting to investigate if unintended out-of-plane action is indeed the primary cause of size effect in shear strength. In order to verify these hypotheses on size effect, an experimental programme consisting of three groups of different heights of deep beams were carried out in this study and is presented in Chapter 5. To reduce the number of variables, the loading and support plate-width-to-beam-height ratio was kept constant at 0.20 for all the specimens. It is essential to design specimens of different sizes, made of the same grade of concrete, having proportional geometry and reinforcement configuration, and exhibiting the same mode of failure.

2.7 Summary

In this chapter, the author proposed a modified Strut-and-Tie Model (STM) for SSDBs which was evaluated using 233 test results collected from literature. The modified model yielded better results than the original STM (Tan et al., 2001 and 2003) in terms of both accuracy and consistency. The influence of stress distribution factor k on model prediction was studied numerically. It was shown that a k value of 4 derived from linear stress distribution assumption is sufficiently accurate for predicting the deep beam shear strength. The modified model was also shown to embed a softening effect in concrete compressive strength due to transverse tensile strain, by adopting an interactive failure criterion, i.e. Kupfer’s failure criterion. The softening effect given by the model was shown comparable to that obtained from MCFT and Belarbi and Hsu's equations.

The modified STM was further extended to predict the ultimate strengths of concrete continuous deep beams (CDBs) on rigid supports. Kupfer's interactive failure criterion was applied to the tension-compression nodal zones and no empirical stress limit is required. The predictions of the STM for CDBs including beam strengths and support reactions were in good agreement with a total of 54 test results of concrete CDBs. The STM was also developed to calculate the ultimate strength of CDBs with differential support settlements. The model predicted the critical middle support stiffness K_{cri}, below which the top member of the STM transformed from a tension tie to a compression strut. The STM correctly reduced to the one for SSDBs when the centre support stiffness vanished, showing the robustness of the model. An experimental programme was carried out to investigate in greater detail the behaviour of CDBs subject to support settlements and to validate the proposed STM using test results. The details will be described in Chapter 3.

Based on the proposed modified STM, the author further developed the model to apply to SSDBs subjected to asymmetrical loads. No empirical stress limit was required for determining (i) the deep beam strength and (ii) the failure mode. The developed STM was shown to be a generalized form for SSDBs embodying the special cases of single-point and two-equal-point symmetric loading conditions. The geometry of STM was dependent on the configuration of asymmetrical loadings, i.e. Load Inequality (LI) and Load Asymmetry (LA). An experimental programme was planned and conducted to look into the effects of unequal and unsymmetrical loadings on deep beams, which will be presented in Chapter 4. The results are also used to validate the proposed STM.

Finally, the author proposed a modified STM incorporating the causes of size effect. It included strut geometry (which governs the size of the loading and support plates and strut length) and strut boundary conditions (which governs the spacing and diameter of web reinforcement that run transverse to the struts). An experimental programme was devised to investigate the size effect in deep beams as presented in Chapter 5. By validating the proposed STM with test results, the author hoped to shed light on the interesting phenomenon of size effect on deep beams by means of strut-and-tie approach.

CHAPTER 3 CONTINUOUS DEEP BEAMS ON SPRING SUPPORTS

This chapter investigated the effects of differential support settlement on the strength and behaviour of two-span Continuous Deep Beams (CDBs). An experimental programme consisting of 6 specimens was carried out with different middle support conditions to investigate the effects of support settlement on the beam behaviour and the influence of web reinforcement in accommodating differential settlements. Material strengths, test setup and loading procedure were briefly introduced. Test results including crack patterns, load-deflection curves, strains in steel, serviceability loads, and ultimate loads were presented and discussed with the effects of support stiffness and web reinforcement. Finally, a direct Strut-and-Tie Model (STM) was proposed to calculate the ultimate strengths of CDBs subjected to support settlement.

3.1 Background

Differential support settlement is commonly encountered in real structures. Even in the laboratory experiments, it is difficult to completely eliminate differential settlement. When the middle support of a two-span continuous deep beam settles more than that at either ends, a sagging moment is formed over the middle support. Consequently, the middle reaction force is relieved somewhat and the end reaction forces are increased.

Leonhardt and Walther (1966) tested two reinforced continuous deep beams, both of which failed in shear at their interior shear spans. The test results showed that the distributions of bending moments and support reactions in continuous concrete deep beams were substantially different from those in regular continuous shallow beams. Rogowsky et al. (1986) reported 17 two-span concrete deep beams tested to failure with a central point load at each span. It was found that beams with vertical web reinforcement showed more ductility and failed at much higher loads than their counterparts without web reinforcement. Chemrouk (1988) conducted an experimental programme consisting of 12 continuous deep beams. Experimental results confirmed earlier findings by Rogowsky et al (1986) that the distributions of bending moments and support reactions in continuous deep beams were fundamentally different from those predicted by ordinary beam theory. The end reactions and the mid-span moments were greater than the predicted values based on ordinary beam theory. Ashour (1997) did a study on continuous deep beams and concluded that the shear capacity is influenced more by vertical web reinforcement as compared to horizontal web reinforcement.

Differential support settlement is commonly believed to be critical in continuous deep beams, and may significantly affect the distribution of reactions and aggravate the crack widths, thereby lowering the ultimate strength (Ashour, 1997; Maimba, 1989; Asin, 1999). However, detailed studies about continuous deep beams subjected to controlled differential support settlement are rather scarce if at all found. The effects of support settlement still remain vague and not fully understood.

Due to the scarcity of test data, specimens with or without web reinforcement are designed with a range of middle support stiffness K, to simulate varying degrees of differential support settlement. The test programme is also aimed to provide test validation for the proposed strut-and-tie model, which incorporates the influence of support settlement. Two variables are introduced in the author's experimental programme, namely, relative middle support stiffness K, and web reinforcement ratio. The term K quantifies the vertical stiffness of the middle support relative to the end supports:

$$K = \frac{R}{\Delta} = \frac{R}{\Delta_B - (\Delta_A + \Delta_C)/2} \tag{3.1}$$

where R = the reaction force of middle support; Δ = the relative settlement of middle support; Δ_A, Δ_B, Δ_C = the respective absolute settlement of support A, B and C. K equals infinity if there is no differential support settlement.

3.2 Experimental Programme

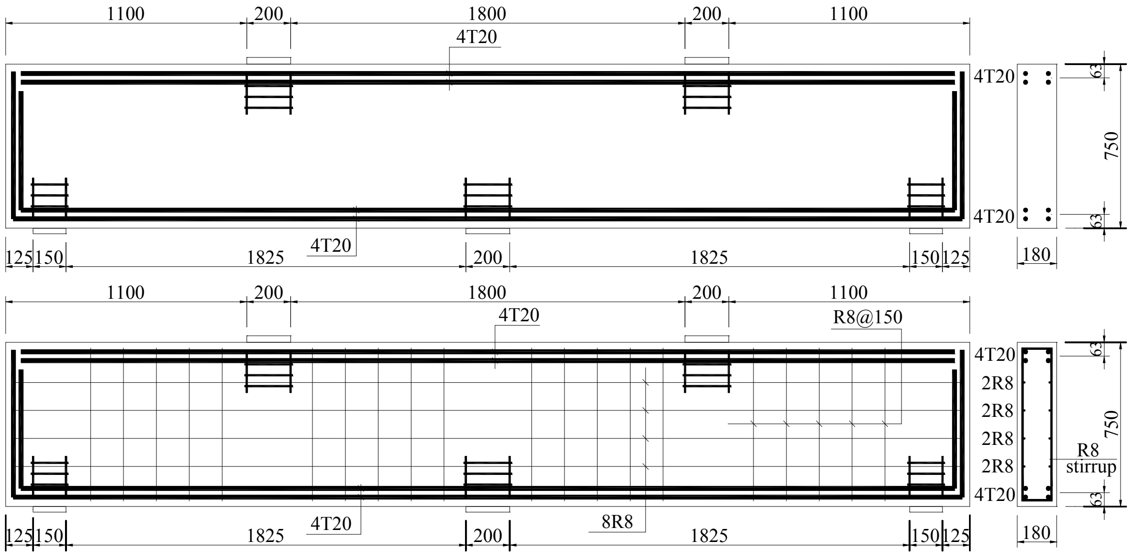

Note: The number following R or T indicates the nominal diameter of the reinforcement bar.

Figure 3.1 Dimensions of specimens and typical reinforcement layout – Top: TCDB-1 series beams, Bottom: TCDB-2 series beams

3.2.1. Specimen details

A total of 6 concrete deep beams of dimension 180 mm (width) x 750 mm (height) x 4400 mm (length) were fabricated. The beam notation was typically written as ‘TCDB-A-B’, where TCDB was an acronym for "two-span continuous deep beam". Two variables were used to characterize the specimens, namely: the web reinforcement configuration ‘A’ and the support configuration ‘B’. There were only two types of web reinforcement configuration ‘A’ with “1” indicating no web steel and “2” both horizontal and vertical web reinforcement. The second alphabet ‘B’ had three variations. The first type was a deep beam tested on three rigid supports (coded 1). The second was a deep beam tested on three elastic supports (coded 2), and the last referred to one with two rigid end supports and one elastic middle support (coded 3). The three different support arrangements led to three different degrees of settlements at the middle support. As an example of the beam notation, specimen TCDB-2-3 was provided with both horizontal and vertical web reinforcement, and rested on rigid end supports and elastic middle support.

The details of the specimens and their respective support conditions are summarised in **Table 3.1**. The beam size and longitudinal reinforcement were kept the same for all 6 specimens, among which, the last three specimens were with web reinforcement, whereas the first three were without. Two types of reinforcement were used in the specimens, namely, deformed high tensile steel (T bar) for top and bottom longitudinal reinforcement and plain round mild steel (R bar) for web reinforcement. The reinforcement details of the specimens are shown in **Figure 3.1**. The top and bottom faces of beams were reinforced with four longitudinal T20 bars, arranged in two layers throughout the whole length. The bottom longitudinal bars had 90° bend at both ends so as to have sufficient anchorage length. Local reinforcement cages were provided at locations of loading and support points to prevent premature crushing.

The concrete mix was designed to have 28-day compressive cube strength of 40MPa. Chippings of 10 mm size were used as coarse aggregates to prevent congestion between the bottom layers of reinforcement. Three cubes and cylinders for each beam were prepared and cured under the same condition as the beams. They were tested on the same day as the beams to assess the concrete strength (**Table 3.1**).

Table 3.1 Details of the Specimens

Beam Notations	h (mm)	b_w [a] (mm)	l_e [b] (mm)	c_1 [c] (mm)	c_2 [c] (mm)	ρ_s [d] (%)	ρ_h [e] (%)	ρ_v [e] (%)	f_y [f] (N/mm^2)	f_{yw} [g] (N/mm^2)	f_c' (N/mm^2)	Support Conditions [h]	
												end	middle
TCDB-1-1	750	180	2000	63	63	1.86	0	0	514.9	525.7	35.6	Rigid	Rigid
TCDB-1-2							0	0			36.1	Spring A	Spring B
TCDB-1-3							0	0			38	Rigid	Spring B
TCDB-2-1							0.36	0.28			36.7	Rigid	Rigid
TCDB-2-1(r)							0.36	0.28			38.9	Rigid	Rigid
TCDB-2-2							0.36	0.28			39.3	Spring A	Spring B
TCDB-2-3							0.36	0.28			38.5	Rigid	Spring B

[a] b_w = beam width;

[b] l_e= Effective span (support to support distance);

[c] c_1, c_2 = the distances from beam top to the top steel centroid and from beam soffit to the bottom steel centroid, respectively;

[d] ρ_s = reinforcement ratio of longitudinal steel (top and bottom);

[e] ρ_h, ρ_v = reinforcement ratios of horizontal and vertical web steel, respectively;

[f] f_y = yield strength of main steel;

[g] f_{yv} = yield strength of web steel;

[h] Details of Spring A and Spring B is referred to **Figure 3.2**.

3.3 Instrumentation and Test Setup

Spring elements A and B (**Figure 3.2**) were specially fabricated for the experimental programme, with nominal spring stiffness of 68 and 101 kN/mm, respectively. It should be noted that spring elements with any higher stiffness are very costly and were not used in the programme.

A typical experimental set-up on three elastic supports is shown in **Figure 3.3**. This set-up (adopted for specimens TCDB-1-2 and TCDB-2-2) was to produce a smaller differential support settlement compared to only using spring element B under the middle support. Two point loads were applied from the top at each mid-span by two actuators, which include inbuilt load cells and attached swivel heads. The computer-driven actuators were controlled by a console, which can toggle between the load- or displacement-control mode. The loading area on top of the beam was leveled off by casting a thin layer of dental stone capping to ensure proper contact. A steel plate of 200 mm in length was then placed over the capping as the loading plate. To record reaction forces, 200-ton and 100-ton load cells were laid under the beam soffit for the middle and the end supports, respectively. Each end support consisted of a concrete block and spring element A with a roller support on top of it. The middle support had spring element B at the bottom and a 200-ton hydraulic jack over it for adjusting the support level. The swivel head attached to the top of the jack served as a pin bearing so that the middle support was free to rotate but was restrained from translation. The lengths of support plates were 150mm and 200mm for the end and the middle support, respectively.

Support settlement was monitored by two 25mm LVDTs on each edge of the support as shown in **Figure 3.3**, making a total of four LVDT measurements for each support. The beam deflection of each span was monitored by two 100mm LVDTs located at the middle soffit. Uniaxial strain gages were installed at the longitudinal and web reinforcement, as shown in **Figure 3.4**, indicated by 'SG' followed by a sequence number.

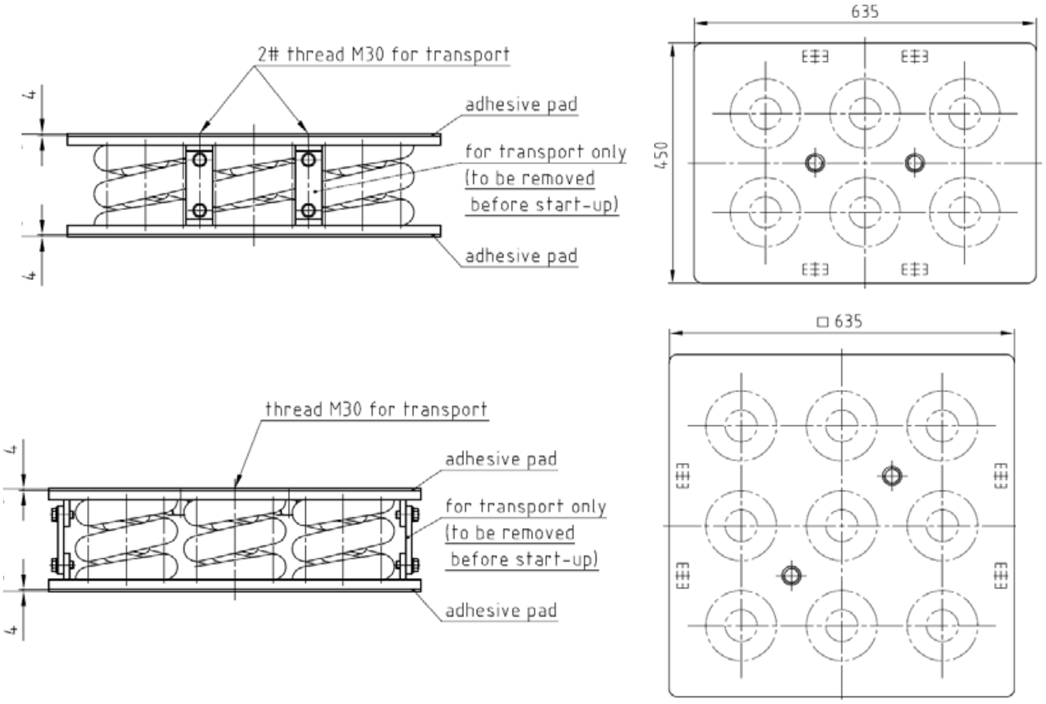

Figure 3.2 Details of the spring elements – Top: Spring A, Bottom: Spring B

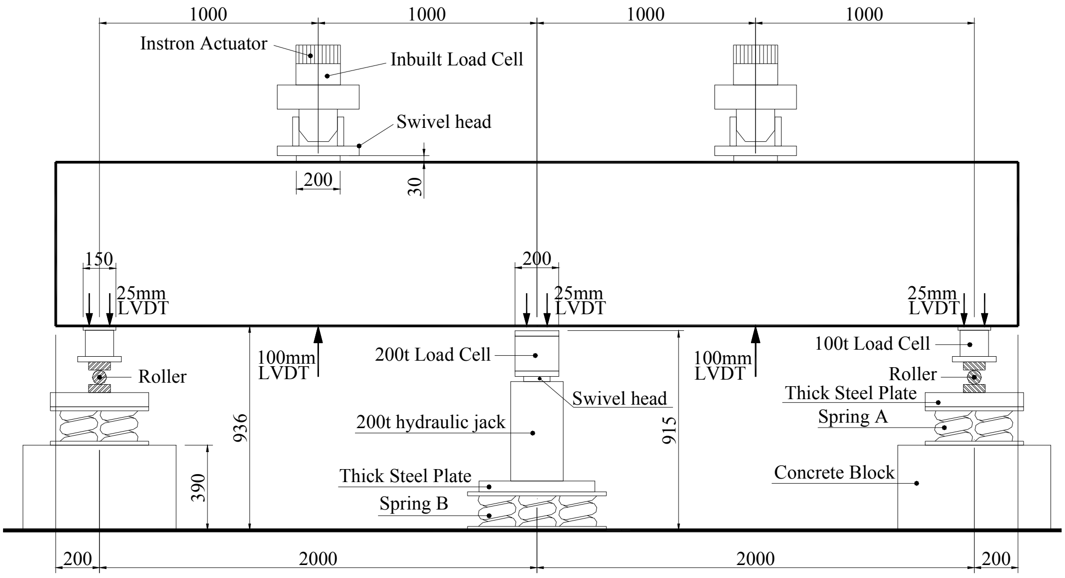

Figure 3.3 Test Setup for Specimens loaded on three elastic supports (TCDB-1-2 and TCDB-2-2)

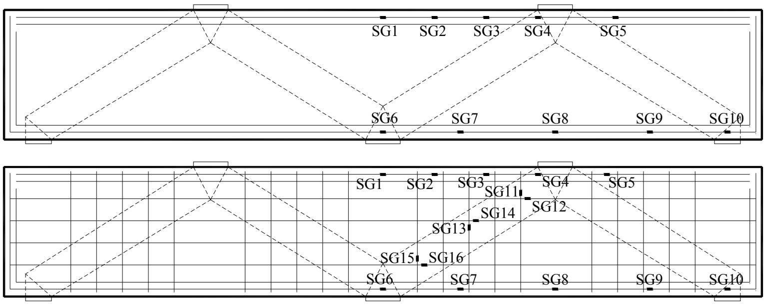

Figure 3.4 Locations of strain gages (with STM indicated in dashed line) – Top: TCDB-1 series beams, Bottom: TCDB-2 series beams

The set-ups for specimens with one elastic support (TCDB-1-3 and TCDB-2-3) and three rigid supports (TCDB-1-1 and TCDB-2-1) were similar to that shown in **Figure 3.3**, except that the appropriate spring elements were replaced with rigid concrete blocks.

Before testing begins, a load P_i = 50 kN was applied to a specimen at each loading point, then the middle support was jacked up to support the beam. The height of middle support was adjusted so that the reaction forces were equal to the values obtained from the linear elastic finite element analysis of the deep beam. This was done to ensure that the middle and end supports were strictly leveled at the beginning of each test. This is permissible as at the uncracked stage, the load-reaction response of a continuous deep beam conforms to elastic finite element analysis (Ashour, 1997). Then the pre-applied load P_i was reduced to almost zero. Load-control mode was firstly adopted at an increment of 20 kN before any cracks were formed on the beam surface. After the first flexural crack was detected, the load increment was increased to 40 kN until the total load reached around 75% of predicted failure load from finite element analysis. Then both actuators were toggled to displacement-control mode to prevent the specimen failing in a sudden manner.

3.4 Experimental Results and Discussion

Table 3.2 Summary of experimental results

Beam Notation	Relative Stiffness of Middle Support K (kN/mm)	f_c'	Ultimate Load P_{exp}(kN)	First positive flexural crack load P_{pcr}(kN)	First negative flexural crack load P_{ncr}(kN)	First diagonal crack load P_{dcr}(kN)	Serviceability Load P_{ser}(kN)
TCDB-1-1	422	35.6	797	240	420	400	400
TCDB-1-2	194	36.1	637	210	400	330	350
TCDB-1-3	83	38	640	180	n/a	280	280
TCDB-2-1	436	38.9	1001	230	410	450	490
TCDB-2-2	200	39.3	1001	220	490	490	450
TCDB-2-3	88	38.5	957	190	n/a	480	400

The specimens were tested under intended differential support settlement by utilizing spring elements at the middle and end supports. By using different spring elements, different values of support stiffness K can be achieved. As the experimentally measured points in R-versus-Δ (Eq. (3.1)) plots do not fall exactly onto a straight line, linear regression is used to obtain the slope (support stiffness K). The value of K for each beam (**Table 3.2**) is very sensitive to support settlement. For a reaction force of 1000 kN, an additional support settlement of 0.2 mm could result in a change in the K value of about 50 kN/mm. It is noted that even for specimens tested with the same support configuration, there was still a slight difference in K values (less than 5%). This is probably due to some uncertain factors that may affect the support settlement, for example, deformation of contact surfaces between steel plates over the support, and deformation of a layer of dental stone cast at the beam soffit. Generally, specimens tested with three rigid supports (TCDB-1-1, TCDB-2-1) have K values exceeding 400 kN/mm. Specimens with three elastic supports (TCDB-1-2, TCDB-2-2) have K values around 200 kN/mm, while specimens with elastic middle support and rigid end supports (TCDB-1-3, TCDB-2-3) have the lowest K value around 90 kN/mm.

3.4.1. Crack Patterns

The crack patterns of the failed specimens are shown in **Figure 3.5**. The load at which each crack was first observed is also indicated in the figure. Those cracks believed to be the cause of failure are marked in bold and the hatched areas indicate concrete crushing or spalling. It can be seen that the crack patterns of beams with web reinforcement (last three specimens) were more developed than their counterparts without web reinforcement (first three specimens). The cracking loads, serviceability loads, ultimate loads, and failure modes of the specimens are summarised in **Table 3.2**. The specimens remained elastic with no visible cracks until flexural cracking took place. The first positive flexural crack load P_{pcr} (per actuator) was typically around 180-240 kN. The first negative flexural crack load P_{ncr} was at the level of 400-490 kN. The presence of web reinforcement did not seem to influence the magnitude of cracking loads (both positive and negative). However, the settlement of middle support substantially influenced the beam cracking strength. As K decreases, the beams experienced a larger settlement.

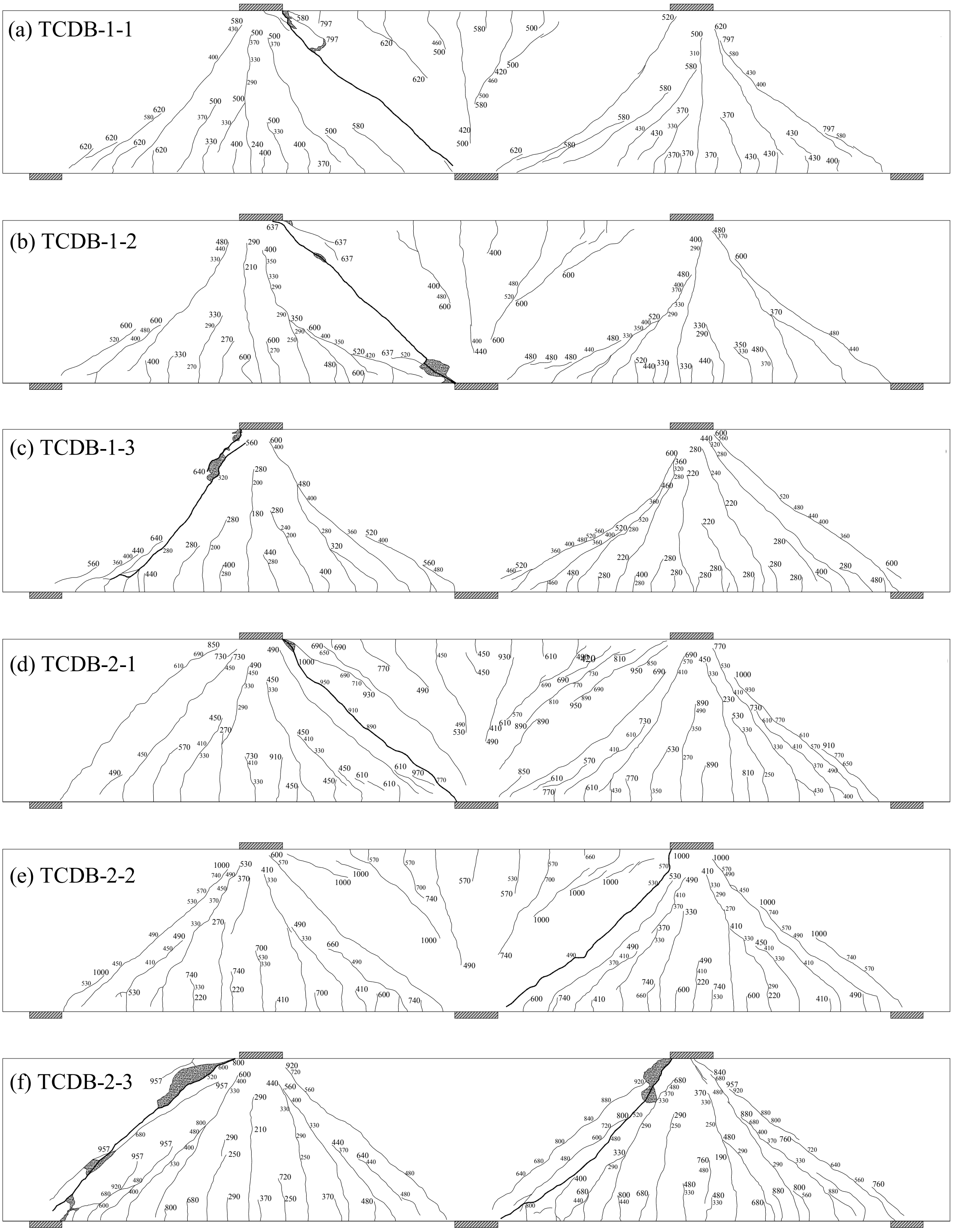

Figure 3.5 Crack patterns of specimens at failure

The first positive flexural crack occurred at an earlier stage whereas the first negative crack over the middle support occurred at a later stage (or even does not occur for TCDB-1-3 and TCDB-2-3 in **Figure 3.5**). This is attributed to increased sagging moment at the mid-span and reduced hogging moment over the middle support. Particularly for beams with web reinforcement, as K decreased from 436 to 88 kN/mm, P_{pcr} was reduced by 17%; for beams without web reinforcement, a reduction of 25% in P_{pcr} was recorded as K decreased from 422 to 83 kN/mm.

Typically, one long flexural crack of about 2/3 of the beam depth occurs over the middle support, accompanied by several smaller flexural cracks near the top reinforcement. Contrary to the shallow beam theory, the first flexural crack occurs at the mid-span rather than over the middle support. This distinct behaviour of CDBs due to shear deformation had also been reported by other researchers (Ashour 1997, Asin 2000, Poh 1995, Subedi 1998). As stiffness K of middle support decreased, this difference in behaviour became even more evident. For specimens TCDB-1-3 and TCDB-2-3, negative flexural cracks did not occur throughout the test. This is attributed to large settlement of middle support, which renders the concrete portion over middle support in compression. Flexural crack widths never reached the serviceability limit of 0.3mm or caused eventual beam failure. Generally, they were finely distributed in the vicinity of bottom reinforcement, indicating mobilization of bottom tie.

Diagonal cracks occurred after negative flexural cracks had taken place and widened quickly under increasing load. The first diagonal crack load P_{dcr} ranged from 280-490 kN, or 0.45 to 0.49 of ultimate load. It was significantly influenced by the support stiffness and web reinforcement. Serviceability limit of cracking (0.3 mm) was reached by diagonal cracks or inclined cracks in the specimens. As diagonal crack widths widened quickly, a few of them merged and developed into critical diagonal cracks that finally led to beam failure.

3.4.2. Load-deflection Response

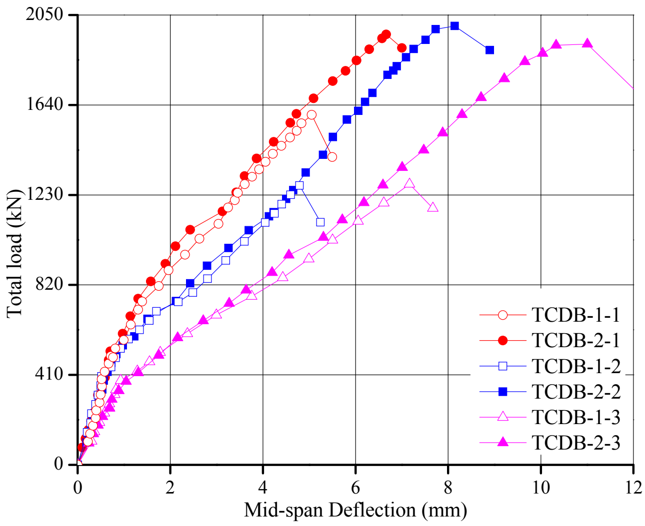

Figure 3.6 Load-deflection curves for specimens

The load-versus-mid-span deflection curves of the failure spans of specimens are plotted in **Figure 3.6**. The settlements of end supports have been excluded from the beam mid-span deflections. As can be seen from the figure, TCDB-1-1 and TCDB-2-1 exhibit the highest beam stiffness whereas TCDB-1-3 and TCDB-2-3 the lowest. It is clear that the support stiffness K has a significant effect on the load-deflection response. As K decreases, the gradient of load-deflection curve becomes gentler. It is attributed to a larger settlement of middle support relative to the end supports. However, web reinforcement has little effect on the beam stiffness. Generally, for the same support conditions, there are no observable differences in load-deflection curves between specimens with or without web reinforcement. Notwithstanding that, web reinforcement significantly increases the ultimate shear strength for all support conditions.

3.4.3. Support Reactions

Table 3.3 Load distribution at ultimate stage

Beam Notations	Reaction Forces (kN)			Loads (kN)	
	Left Support	Right Support	Middle Support	Left Actuator	Right Actuator
TCDB-1-1	324	325	946	797	798
TCDB-1-2	260	259	755	637	636
TCDB-1-3	318	318	643	640	639
TCDB-2-1	389	388	1223	1001	999
TCDB-2-2	418	419	1163	999	1001
TCDB-2-3	497	499	917	957	956

The load-versus-reaction-force responses are plotted in **Figure 3.7**. It is found from the figure that the distribution of support reactions is significantly affected by support stiffness K. As K decreases, the middle support settles more and the end supports take over more loads, thus relieving the reaction of the middle support. Particularly for beams with web reinforcement, 23% of the middle support reaction is transferred to the end supports at the same load when K decreases from 436 kN/mm to 88 kN/mm. A similar reduction in middle support reaction is observed for beams without web reinforcement. This suggests a considerable redistribution of beam internal forces due to support settlement.

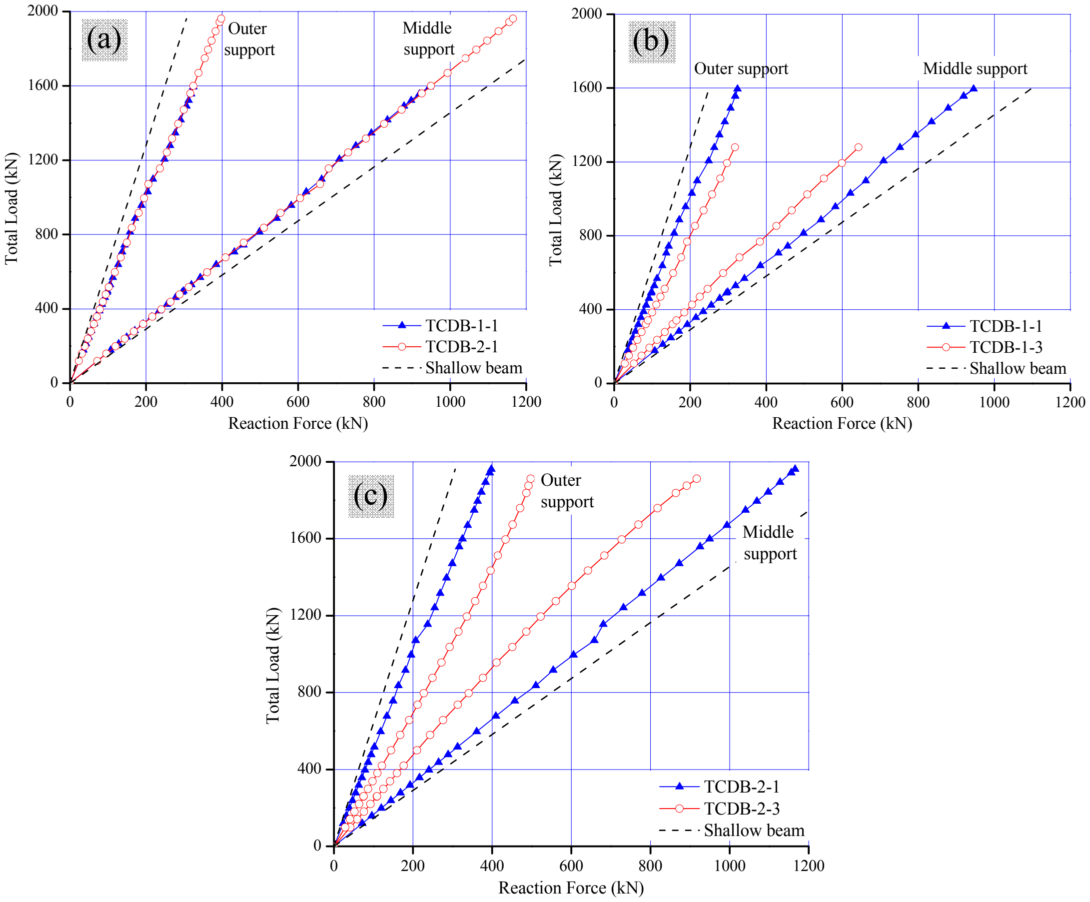

Figure 3.7 Influence of experimental parameters on distribution of support reactions — (a): effect of web reinforcement; (b) & (c): effect of support stiffness

However, the presence of web reinforcement has negligible influence on redistribution ability. This becomes obvious from **Figure 3.7**a, in which specimens with and without web reinforcement exhibit almost the same load-reaction response. Asin (1999) also reported similar findings for the influence of web reinforcement from his experimental programme. At failure, the reaction force of the middle support in a two span continuous shallow beam is about 15% greater than its deep beam counterpart (**Figure 3.7**a). This distinct behaviour of CDBs has been reported by other researchers before (Rogowshy et al., 1986; Ashour, 1997; Asin, 1999; Subedi, 1998; Kong, 1990) and is re-confirmed in the author’s experiments. Furthermore, this difference grows larger as support stiffness K decreases. **Figure 3.7**b and 3.7c show the effect of spring stiffness on the reaction force of the middle support. Compared to the middle support reaction of specimen TCDB-2-3 (K = 88 kN/mm), its shallow counterpart is about 55% higher (**Figure 3.7**c). This is attributed to higher hogging moment over middle support in shallow continuous beams. The reaction forces at failure of the specimens are included in **Table 3.3**.

3.4.4. Serviceability and Ultimate Beam Strengths

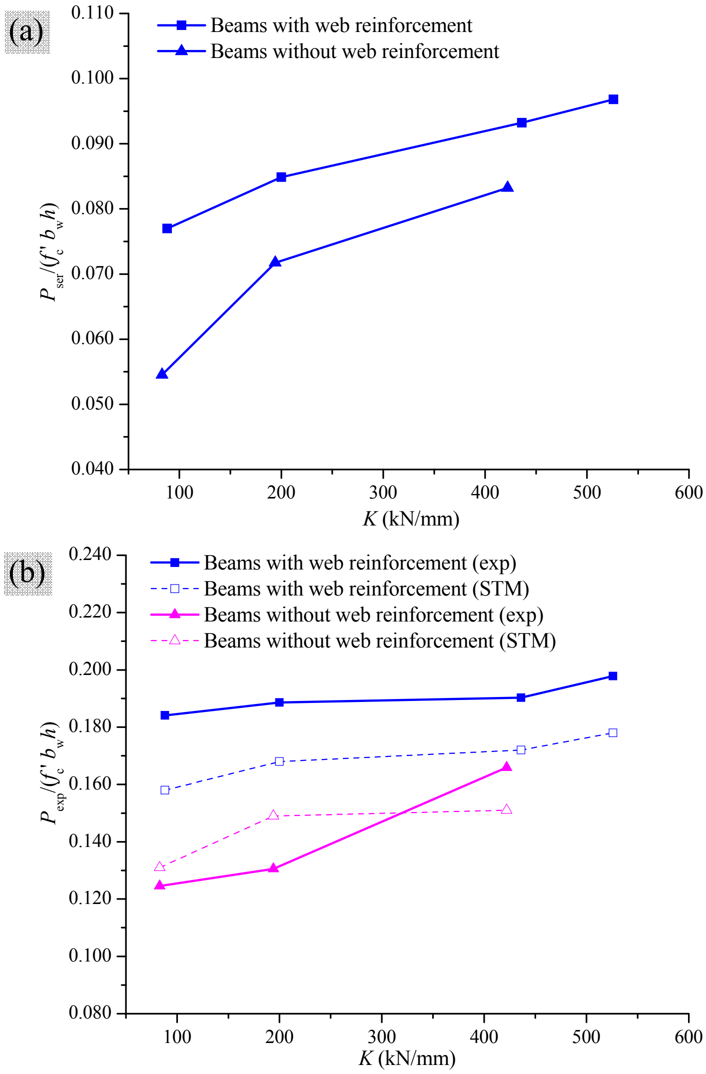

Figure 3.8 Effects of support stiffness K on – (a): service load; (b): ultimate load

The dimensionless ultimate load $P_{exp}/(f_c'b_w h)$ and serviceability load $P_{ser}/(f_c'b_w h)$ of the beams are plotted against support stiffness K in **Figure 3.8**. Test results show an upward trend of the serviceability and ultimate strengths with an increase of K. Serviceability load is significantly reduced as K decreases. Under the same support conditions, that is, with elastic or rigid supports, beams with web reinforcement exhibit slightly higher serviceability loads (0.3 mm cracking) than beams with plain concrete web. This is because the web reinforcement resists tensile stresses in the cracked concrete and deters the widening of crack width. However, web reinforcement plays a more important role in ultimate strength. This increase in ultimate strength is more evident when K decreases, and an enhancement as high as 48% is found in specimen TCDB-2-3 compared to its counterpart without web reinforcement TCDB-1-3 (**Figure 3.8**b).

It is interesting to note that for beams with web reinforcement, the ultimate strength is relatively less sensitive to support stiffness, compared to those without, as opposed to the significant redistribution of beam reaction due to change of support stiffness. This can be explained by the proposed strut-and-tie approach. At the same load level, as K decreases, the compression force in the interior diagonal strut (**Figure 2.12**) decreases whereas the compression force in exterior diagonal strut (**Figure 2.12**) increases, thus delaying the failure within the interior shear span close to the middle support. In this sense, the deep beam capacity does not deteriorate significantly. The specimens exhibited considerable tolerance in accommodating the differential support settlement, particularly for those beams with web reinforcement. In the case when the compression force in exterior diagonal strut increases and initiates failure earlier than interior diagonal strut does, the failure zone would shift from the interior shear span to the exterior. This was observed in specimens TCDB-1-3 and TCDB-2-3 (**Figure 3.5**). In the following, a strut-and-tie model is developed to predict the shear strengths of specimens considering the effects of support settlement.

3.5 Verifications of Proposed STM

Figure 3.9 demonstrates the development of steel strains in specimens. Figures on the left refer to the measured strains on TCDB-2-1 with rigid supports, while those on the right refer to TCDB-2-3 with elastic middle support. The yield strains of longitudinal and web reinforcement are $\varepsilon_y = 2512\ \mu$ and $\varepsilon_{yw} = 2503\ \mu$, respectively. Locations of strain gages can be found in **Figure 3.4**.

The strain development of SG 7-9 in the bottom steel is comparable to one another, validating the assumption of bottom tie. SG 6 and SG10, located at the respective nodal zone C and B (**Figure 2.12**), show substantial delay in their strain development (**Figure 3.9a, 12b**). This is attributed to the interference of compression forces transferred into the nodal zone from diagonal concrete struts. The strain development of SG 1 and SG 2 at the top steel is very similar along the course of loading. For TCDB-2-1, they are in tension whereas for TCDB-2-3, they are slightly in compression. Though SG 3 shows some delay in development, it is reasonable to assume that the top reinforcement acts like a tie. SG 5 is located outside the load point and is in essence under compressive stress, indicating that the top tie member exists only between the two load points. Web reinforcement within the interior shear span yielded prior to or at imminent failure of the beam (**Figure 3.9e**). This suggested the interior diagonal strut was effective.

For specimens tested on elastic middle support and rigid end supports (TCDB-1-3 and TCDB-2-3), the bottom reinforcement yielded at the beam failure **(Figure 3.9b)** and the top reinforcement was in compression throughout the test **(Figure 3.9d),** suggesting the action of a compression strut at the top between two loads. This is due to increased sagging moment caused by large support settlement.

Web reinforcement within the interior shear span did not yield **(Figure 3.9f)** because the interior diagonal strut (**Figure 2.12**b) carried a smaller load compared to the interior diagonal struts of specimen on rigid supports. The exterior shear span attained its shear capacity prior to the interior shear span, and led to the failure of the beam. (**Figure 3.5**c, 5g).

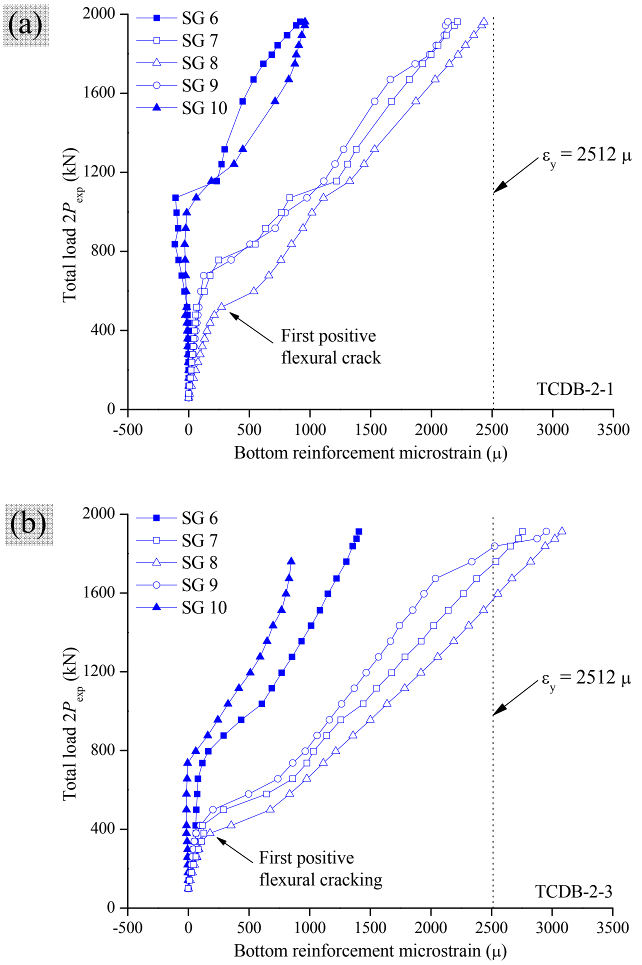

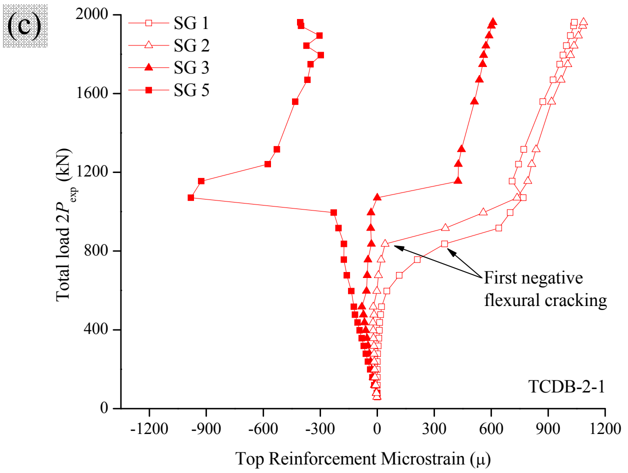
(c)
SG 1
SG 2
SG 3
SG 5
Total load $2P_{exp}$ (kN)
2000
1600
1200
800
400
0
-1200
-900
-600
-300
0
300
600
900
1200
Top Reinforcement Microstrain (μ)
First negative flexural cracking
TCDB-2-1

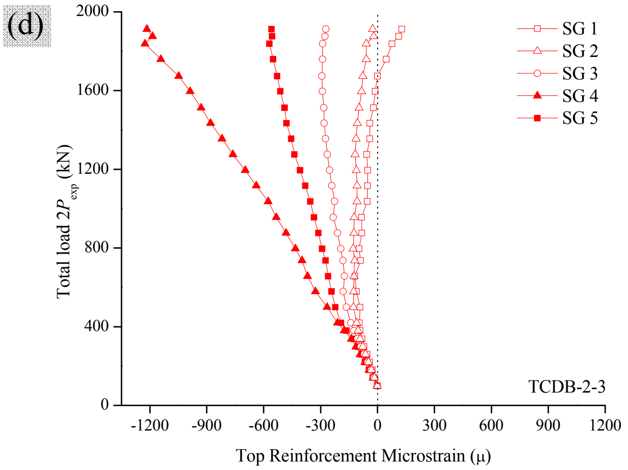
(d)
SG 1
SG 2
SG 3
SG 4
SG 5
Total load $2P_{exp}$ (kN)
2000
1600
1200
800
400
0
-1200
-900
-600
-300
0
300
600
900
1200
Top Reinforcement Microstrain (μ)
TCDB-2-3

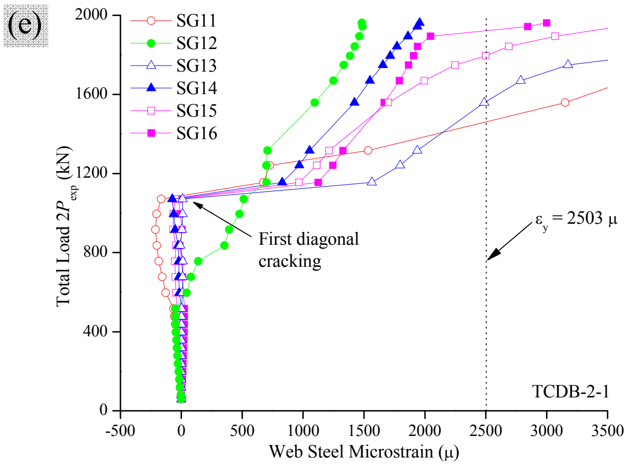
(e)
SG11
SG12
SG13
SG14
SG15
SG16
Total Load $2P_{exp}$ (kN)
2000
1600
1200
800
400
0
-500
0
500
1000
1500
2000
2500
3000
3500
Web Steel Microstrain (μ)
First diagonal cracking
ε_y = 2503 μ
TCDB-2-1

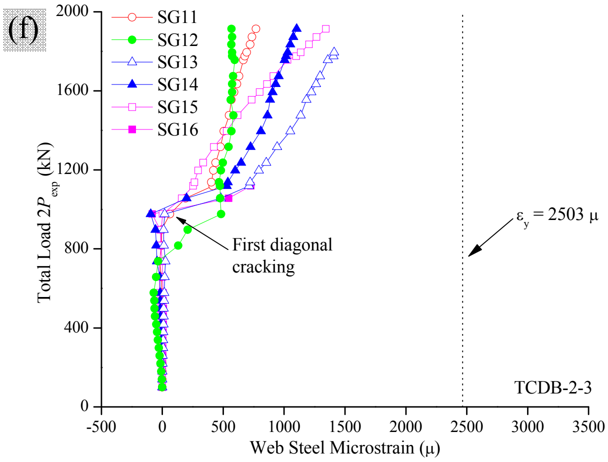

Figure 3.9 Development of steel strains in TCDB-2-1 and TCDB-2-3

The verification of the proposed STM in Chapter 2 on the prediction of failure loads is carried out using the author's tested specimens in **Table 3.1**. The K_{cri} value of the specimens is calculated from Eq.(2.40) to be 99 kN/mm. Thus, specimens TCDB-1-3 (K = 83 kN/mm) and TCDB-2-3 (K = 88 kN/mm) are categorized under Case II where the top horizontal member is in compression – concrete strut. This is evidenced by the crack patterns of the two beams (TCDB-1-3 and TCDB-2-3) where no negative flexural cracks are observed until failure takes place (**Figure 3.5**). The stiffness K of the other specimens is larger than 99 kN/mm, thus these beams belong to Case I, where the top member acts as a tie.

The STM calculations for CDBs can be easily implemented using a spreadsheet. For modelling efficiency, bilinear elastic-plastic material properties are assumed. This simplification for solving the statically-indeterminate truss (**Figure 2.12**) is validated by the good agreement of the ratio of STM-to-experimentally-measured middle support reaction forces at failure (X_{STM}/X_{exp} in **Table 3.4**). It suggests that the proposed STM correctly predicts the internal force distribution of continuous deep beams for different middle support stiffness at ultimate stage. The STM-versus-experiment ultimate strength ratios (P_{STM}/P_{exp}) are also summarised in **Table 3.4**. The STM for CDBs generally performs well in predicting the ultimate strengths with an overall mean of 0.79 and a C.O.V of 0.124. According to the author's model, the failure loads of all Case I specimens are governed by nodal zone B, whereas Case II specimens fail at nodal zone A of exterior shear span. This conforms to the experimental observations that Case I beams fail at the interior shear span whereas Case II specimens at the exterior (critical crack leading to failure is highlighted in **Figure 3.5**). The model also predicts a reduction trend in beam capacity as K increases in value (**Figure 3.8**b). The curves are comparable to experimental results.

Table 3.4 Comparison between STM predictions and test results

Beam Notations	f_c' (MPa)	$2P_{exp}$ (kN)	$2P_{STM}$	X_{exp} [a]	X_{STM} [b]	P_{STM}/P_{exp}	X_{STM}/X_{exp}
TCDB-1-1	35.6	1595	1251	946	759	0.78	0.80
TCDB-1-2	36.1	1274	1212	755	683	0.95	0.90
TCDB-1-3	38	1279	1075	643	515	0.84	0.80
TCDB-2-1	36.7	1962	1492	1166	917	0.76	0.79
TCDB-2-2	39.3	2000	1524	1163	927	0.76	0.80
TCDB-2-3	38.5	1912	1256	917	610	0.66	0.67
Mean						0.79	0.79
SD						0.098	0.076
COV						0.124	0.096

[a] X_{exp} = tested middle support reaction forces;

[b] X_{STM} = predicted middle support reaction forces by STM.

3.6 Summary

This Chapter presented the results of an experimental programme devised to investigate the effects of differential support settlement on the strength and behaviour of CDBs. Major findings are summarised below:

1. All the specimens failed in shear. Support settlement significantly influenced the cracking behaviour and crack patterns of continuous deep beams. The crack patterns of beams with web reinforcement were more extensively developed than those without web reinforcement.

2. Support settlement significantly reduced the serviceability load and beam stiffness; however the beams exhibited considerable tolerance in accommodating the support settlement. The reduction in ultimate strength was not significant, particularly for beams with web reinforcement. The failure zone shifted from interior shear span to exterior as the middle support stiffness K fell below critical support stiffness K_{cri}. Web reinforcement significantly increased the beam capacity, though it had little effect on beam stiffness. Furthermore, web reinforcement was effective on restraining the widening of diagonal cracks, thus increasing the serviceability load.

3. For specimens with middle support stiffness K greater than the critical support stiffness (i.e. $K > K_{\text{cri}}$), it was observed that neither the bottom nor the top longitudinal steel reinforcement yielded during the test. Web reinforcement within the interior shear span yielded prior to or at imminent failure of the beam. This suggested that the interior diagonal concrete strut was fully effective. For specimens with K lesser than the critical support stiffness (i.e. $K < K_{\text{cri}}$), the bottom reinforcement yielded at failure whereas the top reinforcement was in compression throughout the test. This was due to sagging moment caused by large middle support settlement. The exterior shear span

reached its shear capacity prior to the interior shear span and led to the failure of the beam.

4. The distribution of support reactions was significantly affected by the middle support stiffness K. As K decreased, the middle support attracted lesser load while the end supports took more, suggesting a considerable redistribution of beam internal forces. The web reinforcement had negligible influence on the distribution of reaction forces.

The proposed STM in Chapter 2 to calculate the ultimate strength of CDBs with support settlement was used to evaluate the tested specimens. The model predicted the critical middle support stiffness K_{cri} of 99 kN/mm for the beams, below which the top member of STM transformed from a tension tie to a compression strut. This theoretical derivation was backed by experimental observations in strain measurements and crack patterns of Specimens TCDB-1-3 and TCDB-2-3. The K value of these two beams fell below K_{cri}. The proposed model was evaluated by the author's test programme consisting of six medium-strength concrete CDBs with K values ranging from 83 to 436 kN/mm and with or without web reinforcement. It was shown that the model predictions for support reactions and ultimate beam strengths were in good agreement with test results. The simplicity in principle and its ease in implementation show clearly that the proposed STM is a promising tool for engineers.

CHAPTER 4 DEEP BEAMS SUBJECTED TO ASYMMETRICAL LOADS

This chapter examines the effects of unsymmetrical loadings on the strength and behaviour of simply supported deep beams. An experimental programme consisting of 8 specimens was carried out. Test results including crack patterns, load-deflection responses, steel and concrete strains, and failure loads were presented and discussed with the effects of load inequality (LI) and load asymmetry (LA). Conclusions were drawn on the effects of LI and LA on deep beam behaviour. A strut-and-tie model (STM) for was developed for predicting the failure loads of unsymmetrically-loaded deep beams. The ACI 318-05 Strut-and-Tie method and the FEM program WCOMD were employed to calculate the strength of the specimens and compared to the results of the author’s model.

4.1 Background

Simply-supported deep beams (SSDBs) subjected to two equal and symmetrical concentrated point loads have long been one of the main research topics in concrete structures. Technical publications abound with such test data (Kong et al. 1972, Smith and Vantsiotis 1982, Rogowsky et al. 1988, Walraven and Lehwalter 1994, Tan et al. 1995, 1997, Foster and Gilbert 1998, Tan and Lu 1999, Ashour 2000, Tan et al. 2005) and how to model them using strut-and-tie methods as shown in **Figure 4.1** (Tan et al. 1997, 2001, Tan and Cheng 2006, Foster and Malik 2002, Tang and Tan 2004). Strut-and-tie models for deep beams were initially devised based on the stress trajectory of beams under symmetrical and equal loadings (Schlaich et al. 1987). SSDBs subjected to two-point unsymmetrical loads, either in the positions of the loads, or the load magnitude, or a combination of both, have hardly received any attention. However, in practice, deep beams are often loaded unsymmetrically and subjected to unequal load magnitudes. To investigate these effects, the author carried out an experimental programme consisting of 8 deep beams. Two parameters were introduced to define the inequality in load magnitudes and positions respectively, Load Inequality (LI) $n_L = P_1/P_2$ and Load Asymmetry (LA) $m_L = c/a$. As shown in **Figure 4.2**, P_1 and P_2 are the left and the right top load, a and c are the left and the right shear span, respectively. The specimens were designed and tested to failure with different LI and LA configurations to investigate their effects on the behaviour and strength of deep beams.

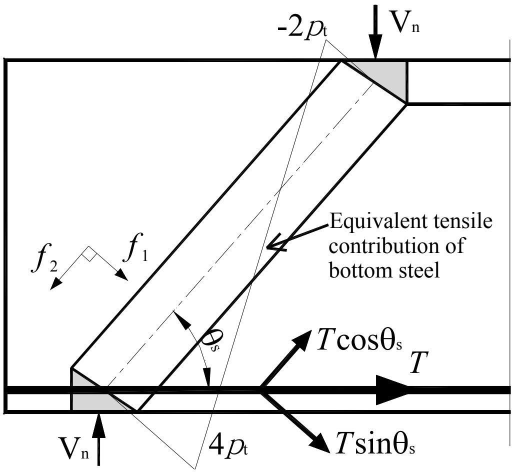

Figure 4.1 Strut-and-tie Model for equally- and symmetrically-loaded SSDBs

The following expression has been proposed from STM for SSDBs under equal and symmetrical loading in Chapter 2:

$$V_{\mathrm{n}} = \frac{1}{\dfrac{4\sin\theta_s\cos\theta_s}{A_{\mathrm{c}}f_{\mathrm{t}}} + \dfrac{\sin\theta_s}{A_{\mathrm{str}}f_{\mathrm{c}}'}} \tag{4.1}$$

where θ_s is the inclination angle of concrete diagonal strut (**Figure 4.1**), A_c is effective cross-sectional area of the beam, and A_{str} is the cross-sectional area of diagonal strut. The term f_t is a composite tensile strength. It has been demonstrated in Chapter 2 that the model is capable of giving *consistent* and *conservative* predictions of shear strengths of normal- and high- strength concrete deep beams. The modified STM for SSDBs subjected to unequal and unsymmetrical loadings is also developed in Chapter 2. The model geometry is analytically derived and experimentally verified by the test specimens conducted by the author. Interestingly, the model also has the capability of predicting the failure modes of specimens. Details of the experimental programme are reported in the following sections.

4.2 Experimental Programme

4.2.1 Specimen Details

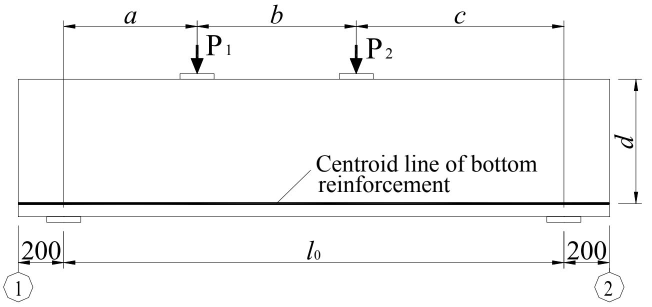

Figure 4.2 Loading configuration of Specimens

In total 8 deep beams were prepared as batch 2 specimens for the experimental programme. The batch 1 specimens consisting of 6 beams were prepared and tested by

Leong (2001). The effective span l_0 and the spacing b between two loads were kept constant for all the specimens (**Figure 4.2**). The details and the loading configurations for each specimen are summarized in **Table 4.1**. Basically, there were four different loading configurations: (a) equal and symmetrical two-point loading, i.e. LI = LA = 1, (b) symmetrical but unequal loading, where the two loads are symmetrically positioned but unequal in magnitude, i.e. LA = 1 whereas LI varies from 1 to 6; (c) equal but unsymmetrical loading, where specimens were subjected to two equal point-loads but the loading positions were not symmetrical about the beam centre, i.e. LI = 1 whereas LA varies from 1 to 4; and (d) both unequal and unsymmetrical loading, where the loads were neither symmetrical in position nor equal in magnitude.

Table 4.1 Details of the Specimens

Beam number		h (mm)	b_w (mm)	a (mm)	b (mm)	c (mm)	d (mm)	ρ_s (%)	ρ_v (%)	f_y (MPa)	f_{yw} (MPa)	f_{cu} (MPa)	f_c' (MPa)	LA	LI
Batch 1 (Leong 2001)	0.60/0.60/P	500	150	600	600	600	428	0.35	1.24	484	328	48.5	41.2	1.00	1
	0.60/0.60/2P			600		600								1.00	2
	0.60/0.60/5P			600		600								1.00	5
	0.45/0.75/P			450		750								1.67	1
	0.30/0.90/P			300		900								3.00	1
	0.30/0.90/5P			300		900								3.00	5
Batch 2	0.75/0.75/P	600	160	750	700	750	527	0.42	1.43	495	369	47.2	38.3	1.00	1(0.94)
	0.75/0.75/2P			750		750								1.00	2(1.94)
	0.75/0.75/4P			750		750								1.00	4(3.70)
	0.75/0.75/6P			750		750								1.00	6(6.51)
	0.45/1.05/P			450		1050								2.33	1
	0.45/1.05/2P			450		1050								2.33	2(2.09)
	0.30/1.20/P			300		1200								4.00	1
	0.30/1.20/2P			300		1200								4.00	2(2.19)

Note: b_w = beam width; d = Effective depth; f_y = yield strength of main steel; f_{yv} = yield strength of web steel; LI = Load Inequality, the number in parenthesis is the measured value; LA = Load Asymmetry.

The beam notation represents the load position and the load magnitude of the specimen. For example, Beam 0.45/1.05/2P refers to a beam with a left shear span of 0.45 m, a right shear span of 1.05 m and the left top load is twice (as designed) larger than the right top load. A single 'P' refers to equal loading, that is, the left top load equals to the right top load. Each beam was provided with an overhang of 200 mm at both ends to ensure sufficient anchorage for the main tension reinforcement. The geometrical properties and reinforcement details the specimens are shown in **Figure 4.3**. All the main bars were bent up at both ends of the beam to develop sufficient anchorage length. There was no web steel provided in the region between the two loading points. Local reinforcement cages were placed at the locations of loading or support points to guard against premature crushing.

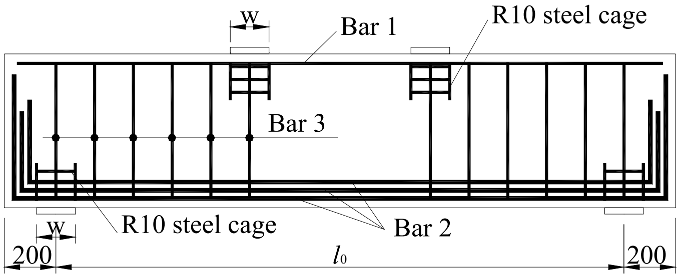

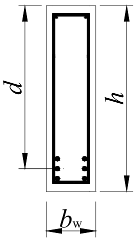

	Batch 1	Batch 2
l_0 (mm)	1800	2200
h (mm)	500	600
d (mm)	428	527
b_w (mm)	150	160
w (mm)	100	150
Bar 1	2R10	2R8
Bar 2	6T13	6T16
Bar 3	R10@300	R8@150

Note: The number following R or T indicates the nominal diameter of the reinforcement bar.

Figure 4.3 Details of Typical Specimens

Specimens were cast using the same batch of concrete and reinforcement. Chippings of 10 mm size were used instead of normal-size aggregates to prevent congestion of reinforcement at the bottom of the beam. The mean values of f_c' for the beams are 41.2 MPa and 38.3 MPa for Batch 1 and Batch 2 specimens, respectively. Details of the steel reinforcement can be found in **Table 4.1**. Two types of reinforcement were used in the specimens, namely, deformed high tensile steel (T bar) for main longitudinal reinforcement and plain round mild steel (R bar) for vertical web reinforcement.

4.2.2 Instrumentation and Test Setup

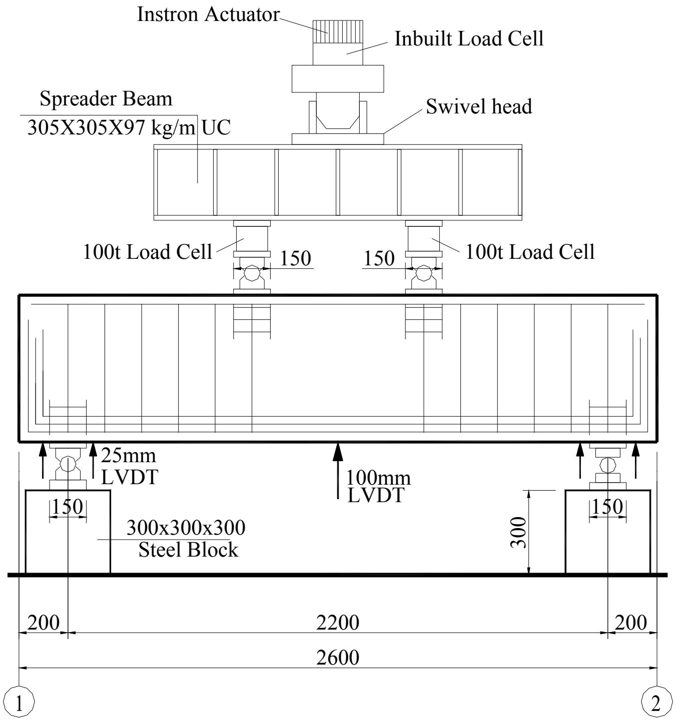

Figure 4.4 Typical Test Setup for Batch 2 Specimens

A typical experimental set-up is shown in **Figure 4.4**. Two loads of unequal magnitude were produced by adjusting the position of a spreader beam. One 100-ton load cell was placed under each loading position to record applied load for Batch 2 beams. Strains in steels were measured using electrical strain gauges. Typical locations of strain gauges are shown in **Figure 4.5**, indicated by ‘SG’ followed by a sequence number. At the same location, there were 2 strain gauges, one at the front and another at the rear surface of the beam, distinguished by letter “a” or “b”, respectively; for example, SG 1a means that the gauge was located on the front surface of the beam. Four specimens, namely, 0.75/0.75/P, 0.75/0.75/2P, 0.45/1.05/P and 0.45/1.05/2P, were mounted with inclined LVDTs to measure the diagonal concrete strain. Typical locations of the LVDTs on the beam are shown in **Figure 4.5**, indicated by a capital letter “L” followed by a sequence number.

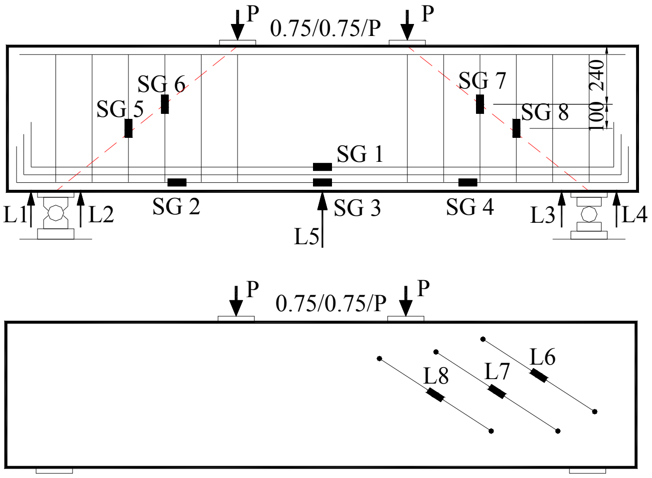

Figure 4.5 Typical locations of LVDTs and strain gauges

Load control method was adopted at first. The specimen was loaded at an increment of 10 kN before any cracks were formed on the beam surface. After the first flexural crack was detected, the load increment was increased to 20 kN until the peak load was reached. Then the actuator was toggled to displacement-control mode with an incremental step of 0.3 mm until the specimen finally failed.

4.3 Experimental Results and Discussion

4.3.1 Crack Patterns

The crack patterns at failure for the beams are shown in **Figure 4.6**. The load at which each crack was first observed is also indicated in the figure. Those cracks which were believed to be the cause of failure are marked in bold and the hatched areas indicate the crushing of concrete. The number beside the load arrow is the designed LI while the number in parenthesis next to it is the measured LI. There could be slight differences between the designed and measured LI due to positioning of the spreader beam. The general cracking behaviour is summarized as follows:

1. For beams under symmetrical but unequal loadings, cracks within the heavier loaded shear span were more developed. Flexural cracks formed at the mid-span tend to incline towards the heavier loaded point. The propagating directions of the flexural and inclined cracks were controlled by the position of heavier load.

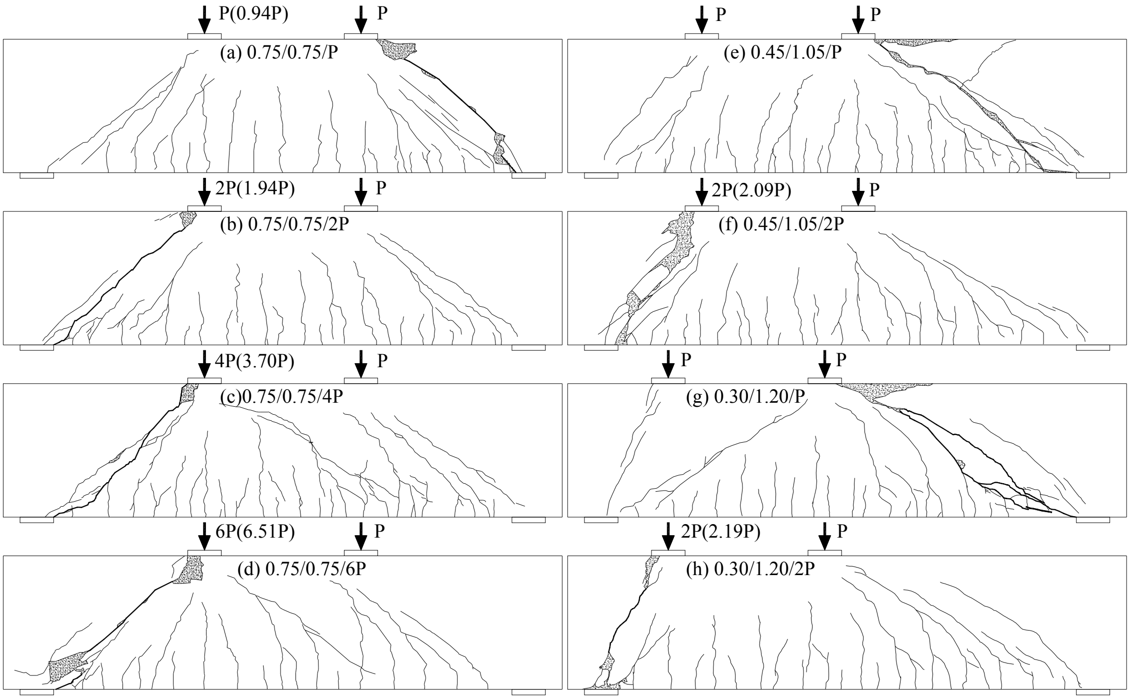

Figure 4.6 Crack patterns for Batch 2 specimens

2. For beams under equal but unsymmetrical loadings, cracks within the longer shear span were more developed. Cracks tend to incline towards the load point nearer the mid-span. In comparison, the load nearer to the support was less dominant on the

crack formation. Diagonal cracks within the shorter shear span did not extend deep into the loading area. All the beams failed at the longer shear span. At imminent failure, a rigid body rotation of the end portion of the longer shear span about the nearer load point was manifest.

3. For beams under combined unequal and unsymmetrical loadings, the shorter and heavier loaded shear span had more developed diagonal cracks. All these beams failed at the shorter shear span.

4.3.2 Behaviour under Unequal/Unsymmetrical Loadings

Table 4.2 Test results of the Specimens

Beam Notations		Initial Flexural Crack Load F_f (kN)	Initial Diagonal Crack Load		Service Load F_{ser} (kN)	Ultimate Load			Mode of Failure	F_f/F_u	F_d/F_u	F_{ser}/F_u
			Left shear-span F_{dl} (kN)	Right shear-span F_{dr} (kN)		F_u (kN)	P_{1u} (kN)	P_{2u} (kN)				
Batch 1 (Leong 2001)	0.60/0.60/P	120	200	n/a	320	500.2	250.1	250.1	DS	0.24	0.40	0.64
	0.60/0.60/2P	200	220	n/a	280	550.1	366.7	183.4	DS	0.36	0.40	0.51
	0.60/0.60/5P	100	240	n/a	280	420.2	350.2	70.0	DS	0.24	0.57	0.67
	0.45/0.75/P	100	n/a	160	220	576.3	288.1	288.2	DS	0.17	0.28	0.38
	0.30/0.90/P	140	n/a	240	300	621.7	310.8	310.9	DS	0.23	0.39	0.48
	0.30/0.90/5P	120	220	n/a	300	589.0	490.8	98.2	SC	0.20	0.37	0.51
Batch 2	0.75/0.75/P	110	230	230	260 (L)	841	408	433	DS	0.13	0.27	0.31
	0.75/0.75/2P	100	220	240	240 (L)	720	475	245	DS	0.14	0.31	0.33
	0.75/0.75/4P	100	210	250	250 (L)	744	586	158	DS	0.13	0.28	0.34
	0.75/0.75/6P*	90	200	240	300 (L)	498	432	66	DS	0.18	0.40	0.60
	0.45/1.05/P	100	200	240	300 (R)	806	407	399	DS	0.12	0.25	0.37
	0.45/1.05/2P	130	210	290	310 (L)	798	540	258	SC	0.16	0.26	0.39
	0.30/1.20/P	100	280	360	280 (C)	907	458	449	DS	0.11	0.22	0.31
	0.30/1.20/2P	140	240	440	320 (L)	871	598	273	SC	0.16	0.28	0.37

Note: * indicates unexpected premature failure; the underlined diagonal cracking load indicates the shear span the specimen failed at; F_{ser} = Total top load at service limit state of cracking (0.3 mm); F_u = Total top load at failure; P_{1u}, P_{2u} = Left and right top load at failure; F_{dl}, F_{dr} = Total top load at the formation of the first diagonal crack on left and right shear span; DS = Diagonal Splitting; SC = Shear Compression; (L), (R) = Serviceability load reached due to diagonal cracks on the left and right shear span; (C) = Serviceability load reached due to diagonal cracks between two loading points.

The cracking loads, service loads, ultimate failure loads and failure modes of the two batches of specimens are summarized in **Table 4.2**. The first flexural cracking load of the specimens was initiated by the maximum bending moment and ranged from 90 to 140 kN, or 0.11 to 0.16 of their ultimate loads.

A typical load versus mid-span deflection curve of SSDB under unsymmetrical loading is plotted in **Figure 4.7**. The initial part of the curve was a short straight line. The beam remained uncracked up to this stage. After the occurrence of first flexural crack, the gradient of the curve decreased slowly and gradually until the formation of the first diagonal crack. Then the curve softened abruptly due to a sudden decrease in beam stiffness and continued with a gentler slope. The curve softened abruptly once again when the diagonal crack within another shear span first occurred. Afterwards, it carried on approximately linearly with an even gentler slope until it reached the softening point and finally the peak. The curve dropped quickly as the beam failed by dramatically losing the load-carrying capacity.

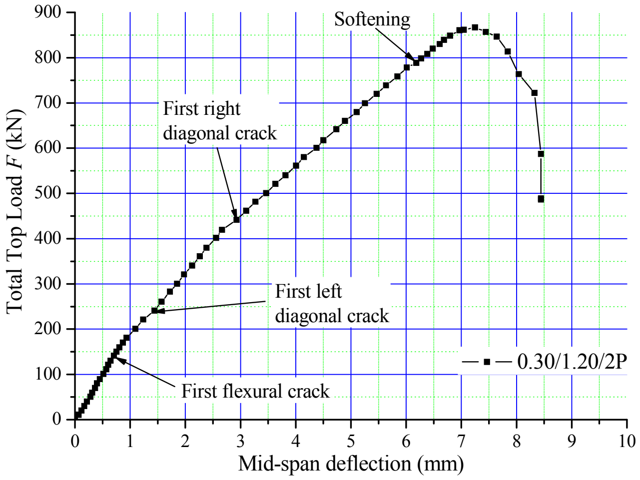

Figure 4.7 Typical load versus mid-span deflection curve

4.3.3 Effects of LI (P_1/P_2) on Beam Behaviour

Three specimens of Batch 1 (Beam 0.60/0.60/P, 2P, 5P) and four specimens of Batch 2 (Beam 0.75/0.75/P, 2P, 4P, 6P) were tested to failure under two symmetrically-positioned but unequal loads, among which the only variation is Load Inequality ratio (LI) P_1/P_2 ranging from 1 to 6. The ultimate shear forces of the *failure shear span* for the specimens are calculated from test results and plotted in **Figure 4.8a**. Test result of Beam 0.75/0.75/6P was excluded from analysis due to premature failure. From the trend line of the test results shown in the figure, there is no strong evidence that an increase of LI has any effect on the shear capacity of the failure span. This is because there is no apparent change in the diagonal strut angles within the failure span as LI increases. Thus the shear capacity of the failure span is expected to be about the same, almost independent of LI. **Figure 4.8b** shows the effect of LI on the *total load capacity* of deep beams. From the figure, it is clear that the total load capacity decreases as the LI increases. The regression line in **Figure 4.8b** gives a better picture of this downward trend. The decrease in the ultimate total load capacity is reasonable as for the same load magnitude a larger part of the total applied load was transferred to the heavier loaded shear spans with an increase of LI. However, the shear strength of the heavily loaded shear span remained unchanged, thus rendering the beam to fail at a lower total applied load.

The load vs. mid-span deflection curves of the four specimens of Batch 2 are plotted in **Figure 4.9a**. As seen from the figure, Beam 0.75/0.75/P exhibited the highest beam stiffness whereas Beam 0.75/0.75/6P showed the lowest one. Thus a higher LI would result in a lower beam stiffness.

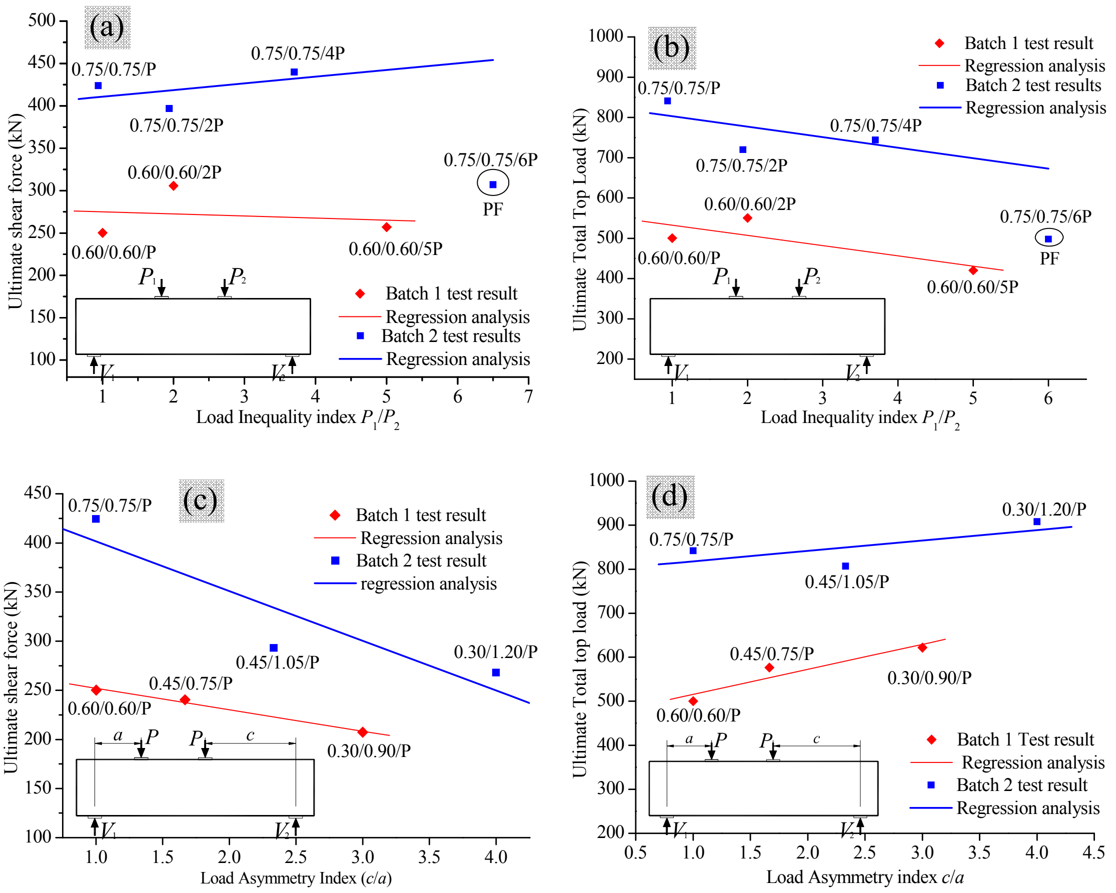

Figure 4.8 Effects of LI and LA on Deep Beam Strength

4.3.4 Effects of LA (c/a) on Beam Behaviour

Two specimens from Batch 1 (Beam 0.45/0.75/P and 0.30/0.90/P) and two specimens from Batch 2 (Beam 0.45/1.05/P and 0.30/1.20/P) were tested to failure under two unsymmetrically-positioned but equal loadings. The designed Load Asymmetry (LA) *c/a* ranged from 1 to 4, where *c* and *a* are the longer and shorter shear spans of the specimen (**Figure 4.2**), respectively. This is because in the longer shear span the diagonal strut angle is much smaller than that of the shorter shear span, resulting in lower shear strength.

The ultimate shear forces of the *failure shear span* are plotted in **Figure 4.8c**. Test results from both batches showed the downward trend of the shear capacity with an increase of LA. This decrease in ultimate shear capacity is due to the reduction of inclination angle of the diagonal concrete strut in the failure span as the loads moved away from the beam centre. It is concluded that LA reduces the beam shear capacity. **Figure 4.8d** shows the effect of load asymmetry on the *total load capacity*. It is interesting to note that the total beam capacity slightly increases as LA becomes larger.

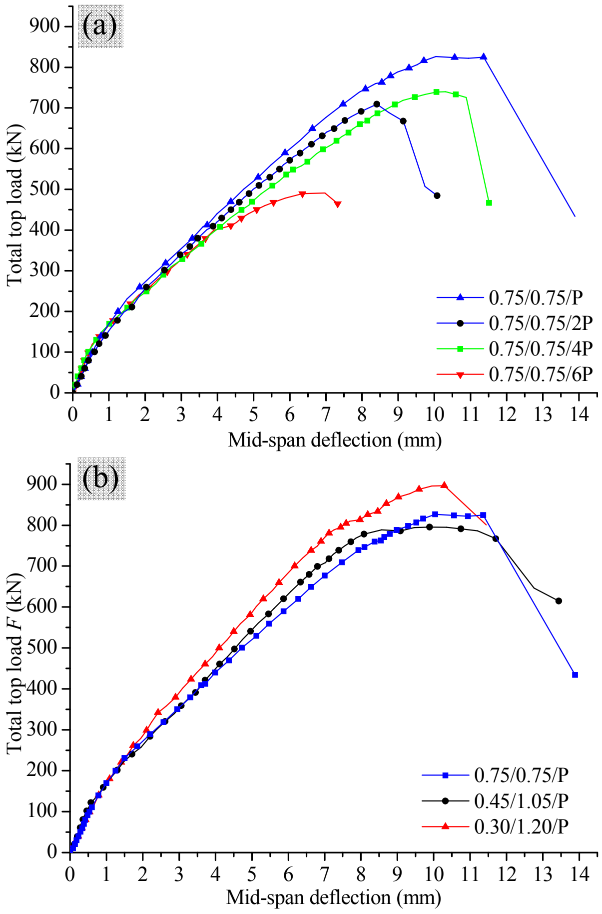

Figure 4.9 Effects of LI and LA on Deep Beam Stiffness

The load versus mid-span deflection curves for unsymmetrically-loaded beams are plotted in **Figure 4.9b**. It is shown that the beam stiffness increased with increasing LA. It reveals that the positions of two-point loads were significant on the beam stiffness and the most critical loading position is nearer to the beam centre.

4.3.5 Steel Strains and Diagonal Deformations

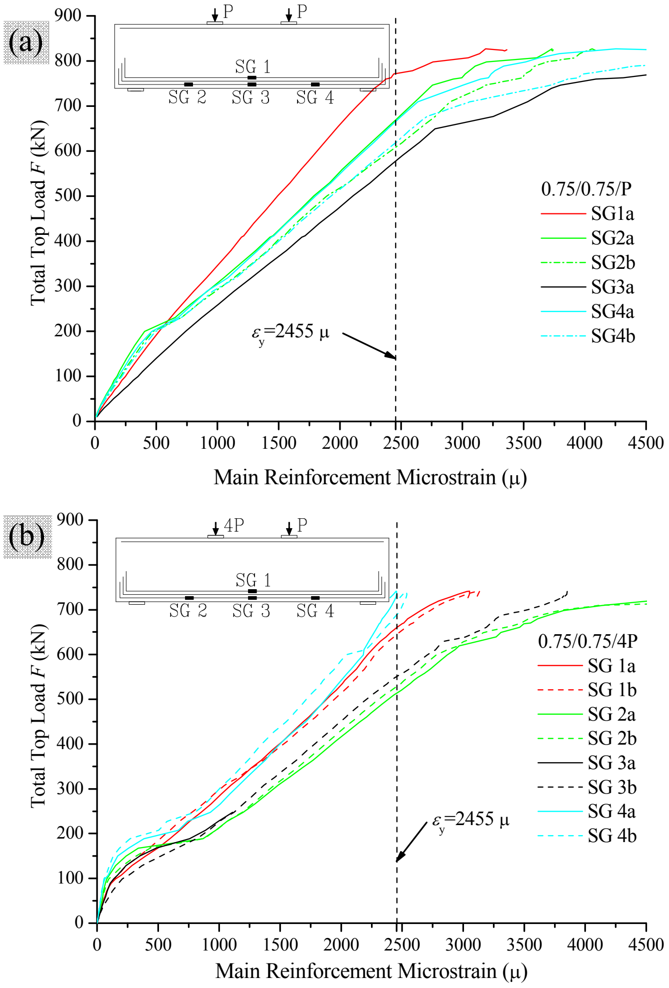

Figure 4.10 Steel strains in main reinforcement

The yield strains of the bottom and web steel are ε_y = 2455 μ and ε_{yw} =1792 μ, respectively. Generally, the main bottom reinforcement yielded before or at imminent failure of the beam. Nonetheless, none of the beams failed in the rupture of the reinforcement or had excessively wide flexural cracks. **Figure 4.10** shows the influence of LI on the main steel strains. The strain development of SG2 and SG4 was almost similar for the equally-loaded specimen in **Figure 4.10a**. But for the unequally-loaded beam, the difference between SG2 and SG4 was obvious. The average difference of tensile forces in longitudinal reinforcement was roughly around 10% of the yield force, and the difference was further reduced as the load increased and the reinforcement reached yielding. This delay of strain increase may indicate a later formation of tension tie within the less heavily loaded span. As the LI increased, such delay became more obvious (**Figure 4.10b**). However, it is still reasonable to assume the main tension reinforcement acting as a *uniform* tension tie, because at the ultimate state of the beam, the strains along the bottom reinforcement were nearly uniform. The LA was observed to have similar influence, where strains in the main reinforcement within the longer shear span were smaller than those within the shorter shear span.

Stirrups in deep beams generally yielded well before failure of the beam. It is obvious that the web reinforcement was effective on restraining the widening of diagonal cracks. As LA decreased to unity, the development of strains in stirrups became faster (**Figure 4.11**), revealing that the tensile stresses within the span were increased as the inclination angle of the diagonal strut decreased in both shear spans.

The average concrete strains along the diagonal strut are determined by the measurements of the LVDTs divided by their respective gauge lengths. **Figure 4.12** clearly shows that diagonal strains within the confines of assumed diagonal concrete strut are much more prominent than those measured outside, about 9 times greater within the failure shear span and 5 times greater within the non-failure shear span. Generally, concrete strains in the diagonal strut within the failure shear span nearly reached the concrete peak strain at failure, averaged at 2132 μ.

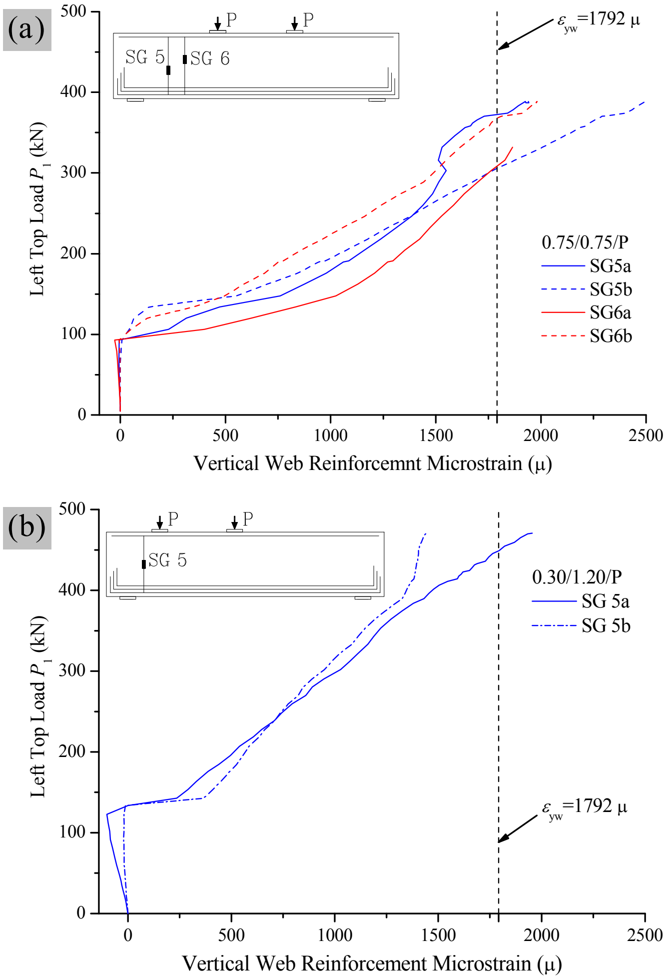

Figure 4.11 Steel strains in stirrups

Meanwhile, strains in diagonal struts within the non-failure shear span were less than 1000 μ. The strains outside the confines of the diagonal strut were significantly reduced, lending strong support to the geometry shape of strut-and-tie model proposed in the following section. It is worth noting that by comparing **Figure 4.12a** and **12b** the compressive strains in the diagonal strut at failure decreased as the diagonal strut angle decreased, whereas tensile strains of the stirrup increased. This suggested there is an interactive relationship between the tensile and compressive actions within the shear span.

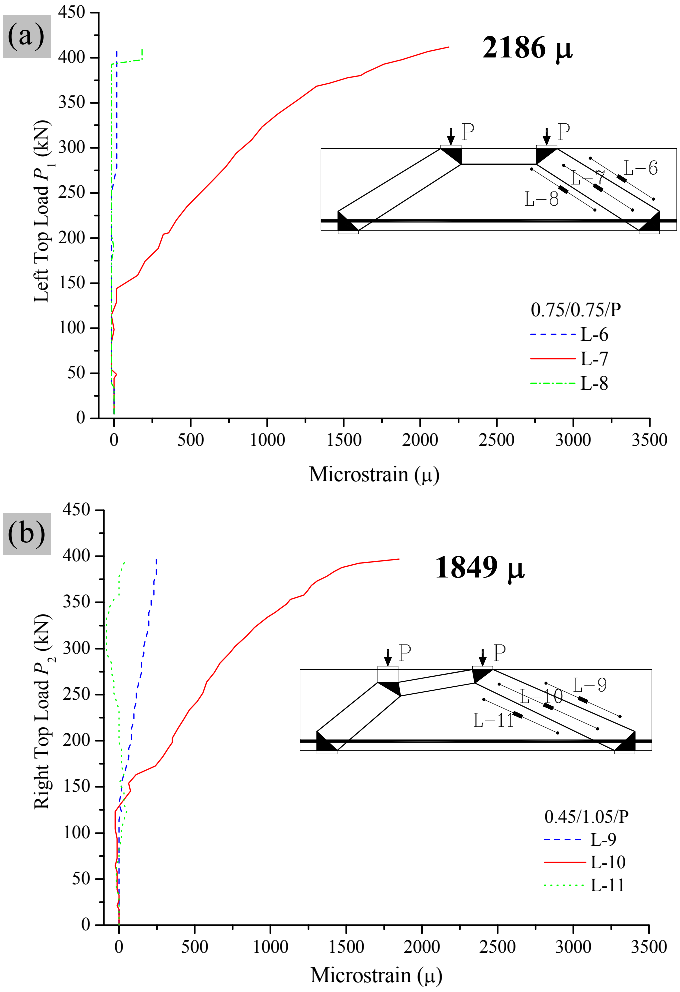

Figure 4.12 Concrete strains in diagonal strut

4.4 Verification of Proposed STM

The STM for SSDBs under asymmetrical loads is proposed in Chapter 2. The outline of the proposed strut-and-tie models for Batch 2 beams are plotted in **Figure 4.13.** The crack patterns at failure are superimposed onto the STMs to demonstrate the similarity between the two. As shown in **Figure 4.13 (a)**, **(b)**, **(c)** and **(d)**, for symmetrically-loaded specimens, with an increase of LI (P_1/P_2) ratio, the top concrete strut rotates clockwise. From the observed crack patterns, it is conceivable that at the limit for very large P_1/P_2, the load-carrying mechanism will be similar to the STM shown in **Figure 2.15(d)**. On the contrary, an increase in LA (c/a) causes the top strut to rotate anticlockwise (**Figure 4.13(a), (e), (g)**). It is interesting to note that in the limit for very large LA, the load-carrying mechanism will also be similar to **Figure 2.15(d)**, that is, left diagonal strut CA and top strut AB join as one straight line, i.e. θ = α. This is clearly observed from Figure 4.16 (c) and (d), when LI = 4 and 6, respectively.

Table 4.3 Summary of prediction results

Beam Notations		Tested F_u^{test} (kN)	Predicted F_u^{ACI} (kN)	$\frac{F_u^{ACI}}{F_u^{test}}$	Predicted F_u^{STM} (kN)	$\frac{F_u^{STM}}{F_u^{test}}$	Predicted F_u^{FEM} (kN)	$\frac{F_u^{FEM}}{F_u^{test}}$	Tested Failure Mode	v_t by STM
Batch 1 (Leong 2001)	0.60/0.60/P	500.2	704.7	1.41	417.9	0.84	490.0	0.98	DS	0.88
	0.60/0.60/2P	550.1	513.9	0.93	381.2	0.69	470.0	0.85	DS	0.88
	0.60/0.60/5P	420.2	472.2	1.12	349.7	0.83	410.0	0.98	DS	0.87
	0.45/0.75/P	576.3	711.2	1.23	433.8	0.75	530.1	0.92	DS	0.91
	0.30/0.90/P	621.7	763.7	1.23	470.3	0.76	530.0	0.85	DS	0.93
	0.30/0.90/5P	589	527.6	0.90	460.5	0.78	540.0	0.92	SC	0.70
Batch 2	0.75/0.75/P	841	813	0.97	576.6	0.69	778.6	0.93	DS	0.85
	0.75/0.75/2P	720	756	1.05	535.9	0.74	705.8	0.98	DS	0.84
	0.75/0.75/4P	744	712	0.96	504.0	0.68	653.7	0.88	DS	0.84
	0.75/0.75/6P*	498	687	1.38	485.6	0.98	606.3	1.22	ST	0.84
	0.45/1.05/P	806	847	1.05	626.6	0.78	748.1	0.93	DS	0.90
	0.45/1.05/2P	798	825	1.03	612.7	0.77	786.1	0.99	SC	0.73
	0.30/1.20/P	907	928	1.02	705.4	0.78	831.1	0.92	DS	0.91
	0.30/1.20/2P	871	665	0.76	663.3	0.76	801.1	0.92	SC	0.66
	Mean			1.05		0.77		0.93		
	SD			0.167		0.075		0.045		
	COV			0.159		0.097		0.049		

Note: * = this beam failed prematurely and was excluded from analysis; DS = Diagonal Splitting; SC = Shear Compression; ST = Shear Tension.

The STM for SSDBs under unequal and unsymmetrical loadings performs well in predicting the ultimate strengths with an overall mean prediction-to-test-result ratio of 0.77 and a C.O.V of 0.097 (**Table 4.3**). A worked example is included in Appendix E to illustrate the use of proposed strut-and-tie model. Calculated stresses in STM components are summarized in **Table 4.4.** In general, the proposed model is on the safe side and gives accurate and consistent predictions.

Table 4.4 Summary of calculated stresses in STM components

	Beam Notations	Calculated compressive stress in strut	Tested compressive stress in strut	Calculated tensile stress in nodal zone	Tested tensile stress in nodal zone
Batch 1 (Leong 2001)	0.60/0.60/P	0.35f_c'	0.42f_c'	0.16f_c'	0.19f_c'
	0.60/0.60/2P	0.35f_c'	0.50f_c'	0.16f_c'	0.23f_c'
	0.60/0.60/5P	0.35f_c'	0.42f_c'	0.16f_c'	0.19f_c'
	0.45/0.75/P	0.36f_c'	0.47f_c'	0.12f_c'	0.17f_c'
	0.30/0.90/P	0.36f_c'	0.47f_c'	0.10f_c'	0.13f_c'
	0.30/0.90/5P	0.43f_c'	0.55f_c'	0.28f_c'	0.36f_c'
Batch 2	0.75/0.75/P	0.43f_c'	0.63f_c'	0.19f_c'	0.27f_c'
	0.75/0.75/2P	0.43f_c'	0.58f_c'	0.19f_c'	0.25f_c'
	0.75/0.75/4P	0.43f_c'	0.63f_c'	0.19f_c'	0.28f_c'
	0.75/0.75/6P	0.43f_c'	0.44f_c'	0.19f_c'	0.19f_c'
	0.45/1.05/P	0.45f_c'	0.58f_c'	0.12f_c'	0.16f_c'
	0.45/1.05/2P	0.46f_c'	0.60f_c'	0.30f_c'	0.39f_c'
	0.30/1.20/P	0.46f_c'	0.60f_c'	0.10f_c'	0.13f_c'
	0.30/1.20/2P	0.50f_c'	0.65f_c'	0.34f_c'	0.44f_c'

The Strut-and-Tie Model (STM) documented in Appendix A of the ACI 318-05 is also used to calculate the shear capacity of the author's specimens. The ACI 318-05 STM procedure is similar to the ACI 318-02, which was demonstrated by Russo et al. (2005) to calculate deep beam shear strengths, except that the effective compressive stress ratio of concrete in the strut β_s is revised to 0.75 by ACI 318-05. The comparison result is shown in **Table 4.3**. The mean ratio of ACI strut-and-tie prediction-to-test result is 1.05 with a COV of 0.159. It appears that the ACI STM slightly overestimated the ultimate shear strengths.

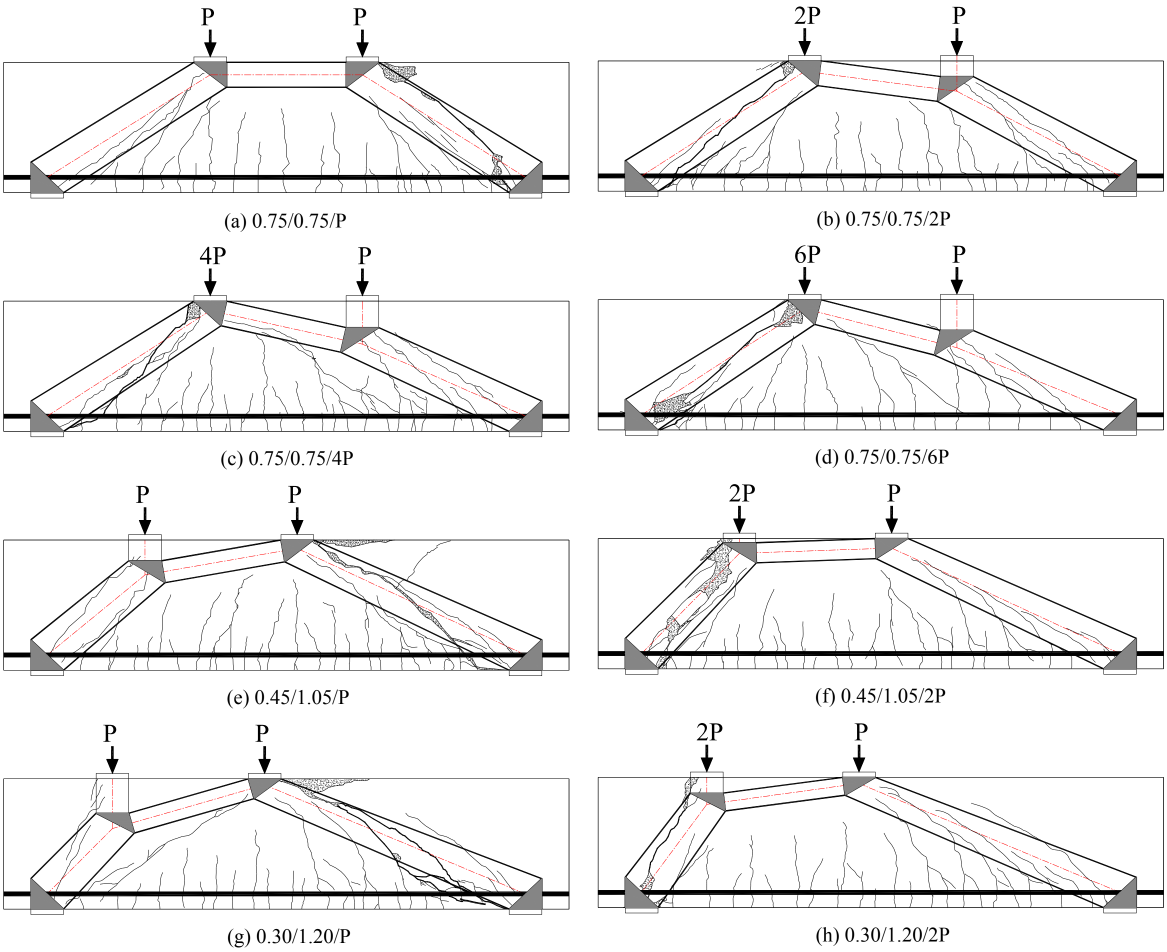

(a) 0.75/0.75/P
(b) 0.75/0.75/2P
(c) 0.75/0.75/4P
(d) 0.75/0.75/6P
(e) 0.45/1.05/P
(f) 0.45/1.05/2P
(g) 0.30/1.20/P
(h) 0.30/1.20/2P

Figure 4.13 Strut-and-Tie model and cracks pattern of tested specimens

4.5 Finite Element Analysis

In this analysis, finite element program WCOMD developed at the University of Tokyo is used. It is capable of accurately modelling the shear behaviour of reinforced concrete beams by considering tension softening, shear softening of plain concrete, and the bond effect of reinforcement. The program has been verified for various cases including shear failures of RC members by researchers (Maekawa et al. 2003, Tsuchiya et al. 2002, Tan et al 2005). The zoning method proposed by An et al. (1997) is adopted in the meshing of finite element models. Concrete domain is divided into two different zones, i.e. the plain concrete (PL) zone and the reinforced concrete (RC) zone. The PL zone exhibits tension-softening behaviour with discrete localization whereas the RC zone exhibits tension-stiffening behaviour with distributed fractures. The overall behaviour is therefore described by a mixed discrete-smeared fracture varying from place to place over the whole domain. It is also applicable to use a mixed element formulation containing both PL and RC zones when reinforcement is small and separate. In this case, the stiffening/softening parameter *cm* is determined from the equation of fracture energy balance as follows:

$$\int_0^\infty \sigma_\mathrm{t} d\varepsilon_\mathrm{t} = \int_0^\infty f_\mathrm{t}\left(\frac{\varepsilon_\mathrm{tu}}{\varepsilon_\mathrm{t}}\right)^{cm} d\varepsilon_\mathrm{t} = \frac{(l_\mathrm{e} - h_\mathrm{e})\int_0^\infty \sigma_\mathrm{PL} d\varepsilon_\mathrm{t} + h_\mathrm{e}\int_0^\infty \sigma_\mathrm{RC} d\varepsilon_\mathrm{t}}{l_\mathrm{e}} \tag{4.2}$$

where l_e is the height of finite element and h_e is the equivalent height of RC zone; ε_t is the average concrete tensile strain and ε_tu is the concrete cracking strain. The respective stresses in RC and PL zone, σ_RC and σ_PL, are defined as follows:

$$\sigma_\mathrm{RC} = f_\mathrm{t}\left(\varepsilon_\mathrm{tu} / \varepsilon_\mathrm{t}\right)^{0.4} \tag{4.3}$$

$$\int \sigma_\mathrm{PL} d\varepsilon_\mathrm{t} = \int f_\mathrm{t}\left(\varepsilon_\mathrm{tu} / \varepsilon_\mathrm{t}\right)^{c} d\varepsilon_\mathrm{t} = \frac{G_\mathrm{f}}{l_\mathrm{r}} \tag{4.4}$$

where fracture energy G_f can be determined from CEB-FIP model code (1990) for normal strength concrete:

$$G_\mathrm{f} = (1.25 d_\mathrm{max} + 10)(f_c^{'} / 10)^{0.7} \times 10^{-3} \tag{4.5}$$

where d_max is the maximum size of aggregate in mm.

Shear softening is implemented in finite element computation by adjusting the shear stress-strain curve based on shear fracture energy and element size, in a similar way to tensile fracture.

$$\tau = \begin{cases} G\gamma & \text{if } \gamma < \gamma_{\mathrm{u}} \\ G\gamma \left(\dfrac{\gamma_{\mathrm{u}}}{\gamma} \right)^{c} & \text{if } \gamma \geq \gamma_{\mathrm{u}} \end{cases} \tag{4.6}$$

Here c in Eq. (4.6) is the shear softening parameter, γ_{u} is the ultimate shear strain defined to be 400 μ for plain concrete and 4000 μ for RC.

In the analysis, the "member" tensile strength used in the analysis was determined from reverse analysis so that the predicted load at the first cracking coincided with experimental results. The FEM results are shown in **Table 4.3** with an average prediction-to-test-result ratio of 0.93 and a COV of 0.049.

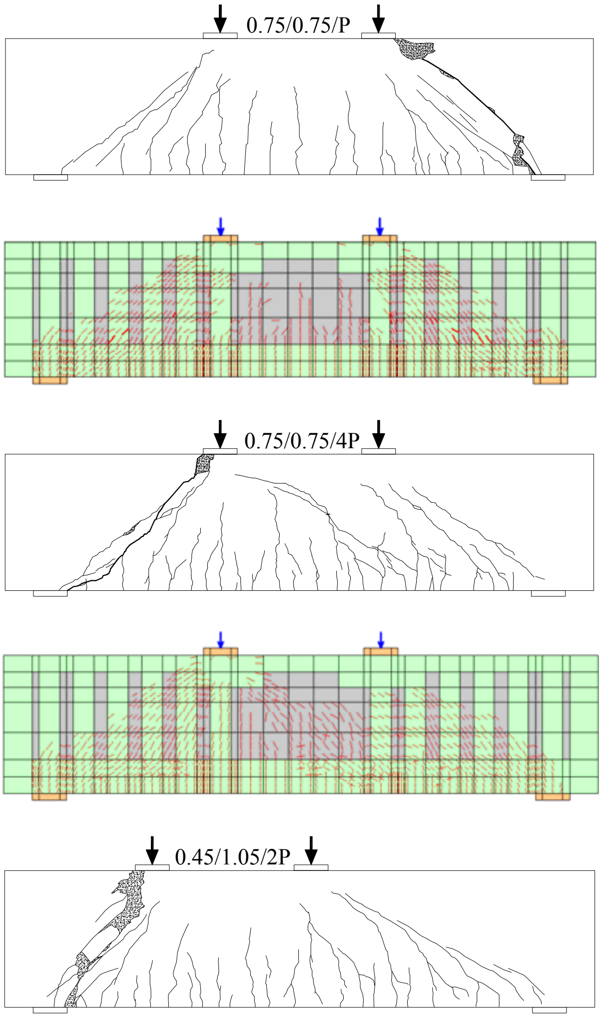

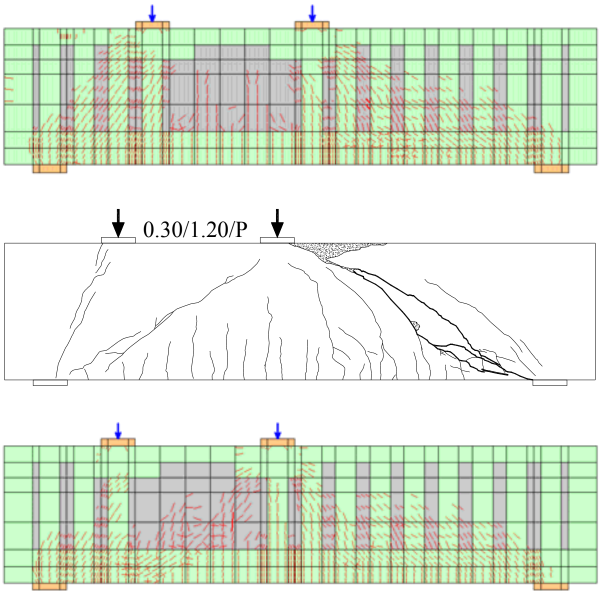

Figure 4.14 Crack patterns of Specimens at failure (a) Test (b) FEM

The FEM simulated crack patterns are also plotted with the crack patterns for Batch 2 beams in **Figure 4.14**. Clearly, they show very good resemblance to observed failure crack patterns

4.6 Summary

This chapter presented the findings of an experimental programme on the effects of unequal and unsymmetrical loadings on the strength and behaviour of SSDBs, summarized below:

1. LI and LA significantly influenced the cracking behaviour and patterns of deep beams.

2. LI reduced the ultimate total load and beam stiffness, whereas LA enhanced the ultimate total load and beam stiffness. Increase of LI appeared to have little influence on the shear strength of the failure shear span.

3. Generally, main bottom longitudinal reinforcement yielded before or at imminent failure of the beam. This lent experimental evidence to the formation of a

tension tie at the failure stage. However, all the beams failed in shear. Stirrups in deep beams also yielded well before failure of the beam.

4. Generally, concrete strains along diagonal strut within the failure shear span reached or nearly reached the peak concrete compressive strain. Concrete strains outside the confines of the diagonal strut were significantly smaller.

5. With an increase of diagonal strut angle, the compressive strain (at failure) in the diagonal concrete strut increased while the tensile strain in the stirrups (at failure) within the shear span decreased. It suggested an interactive relationship between tension and compression actions within the failure shear span.

In Chapter 2, the author proposed a direct strut-and-tie model utilizing Kupfer's interactive failure criterion. The proposed STM was found to be a generalized form for SSDBs embodying the special cases of single-point and two-equal-point symmetric loading conditions. The geometry of STM was dependent on the configuration of asymmetrical loadings, i.e. Load Inequality (LI) and Load Asymmetry (LA). This theoretical derivation was backed by experimental observations from **Figure 4.13**. Explicit expressions of failure loads for the beams were derived and an iterative procedure was employed. The proposed model was evaluated by 14 specimens, with LI ranging from 1 to 6 and LA from 1 to 4. The resemblance between the STM geometry and the observed crack patterns validated that the proposed STM was a reasonable representation of the beam stress trajectory at the ultimate stage. The model predictions for ultimate beam strengths were found in good agreement with test results. The FEM analysis was carried out using program WCOMD to supplement the study.

The beam failure crack patterns and the ultimate strengths were correctly predicted by FEM.

It was shown that the prediction accuracy and consistency of proposed STM were comparable to FEM predictions. The proposed STM was a promising tool for predicting the failure strengths and modes of deep beams.

CHAPTER 5 SIZE EFFECT IN DEEP BEAMS

An experimental programme consisting of three groups of 11 specimens was carried out to investigate the possible causes of size effect, typically represented by a reduction in shear strength with an increase in the height of deep beams. It was postulated that the factors influencing the strength of a compression member, i.e. the strut geometry and boundary conditions, govern the size effect. The experimental programme provided experimental evidence to the hypotheses from strut-and-tie models. By properly configuring the loading and support plate dimensions, size effect in ultimate shear strength was significantly mitigated, even for beams with plain concrete web. Effects of out-of-plane actions and web reinforcement on beam strength were also investigated and discussed. The modified STM incorporating the causes of size effect was introduced and compared with several other methods in predicting the ultimate beam shear strengths.

5.1 Background

Size effect in shallow RC beams is represented by a reduction in ultimate shear strength due to an increase in beam size. The phenomenon has been well documented in the literature (Kani 1967, Walraven 1978, Reinhardt 1981, Bazant and Kim 1984; Bazant and Kazemi 1991). It has been suggested that the causes of size effects may be explained in terms of fracture-mechanics concepts, in both linear (Reinhardt 1981) and non-linear forms (Bazant and Kim 1984, Bazant and Kazemi 1991). Recently, new developed methods such as discrete element method (DEM) to determine dynamic response of concrete structures seemed promising in simulating the size effect of shear and flexural strength in shallow beams by considering non-homogeneous material characteristics and the concrete fracture (Rios and Riera 2004).

However, RC deep beams ($a/d \leq 2$ (ACI 318-05)) loaded in shear behave very differently from shallow beams due to the arch-action after diagonal cracking has occurred. Whether size effect occurs in deep beams remains questionable among researchers (Walraven and Lehwalter1994, Kotsovos and Pavlovic 2004). This is mainly because experimental data are relatively scarce on deep beams with geometrically-varied beam size and reinforcement, while maintaining the same a/d ratio and comparable concrete strength f_c'. Moreover, researchers did not pay much attention to the dimensions of loading and support plates when planning this kind of tests (Collins and Kuchma 1999; Tan and Lu 1999; Yang et al 2003).

Lertsrisakulrat et al (2001) tested a series of concrete cylinders with the same diameter but various heights from 200 to 800 mm. As the member size increases, a higher compression load is expected. Thus a larger volume of concrete failure zone would be needed to consume the additional energy at failure. However, in the tests, the size of concrete failure volume was found to be almost unchanged despite an increase in cylinder height. This was largely attributed to all cylinders having the same diameter, i.e. the same loading area. Hence, it is inferred from their tests that, if an increase in concrete member size does not bring about a corresponding increase in its potential failure volume, then the enhancement in member strength is limited. Interestingly, Soltani et al 2005 demonstrated using exact stress field approach that a set of two-dimensional scaled prismatic beams (both concrete cross section and axial length are proportionally scaled) is size-independent when subjected to shear and axial forces. On the contrary, the shear stresses of the prismatic beams with only cross section scaled were shown to be size-dependent.

Following the above observation, the author argues that the dimensions of loading and support plates have a significant effect on shear strength of RC deep beams because the diagonal struts mobilised by arch action (after diagonal cracking) are analogous to concrete cylinders under compression. The loading and support plate size will affect the dimension of diagonal strut and nodal zone (potential concrete failure volume), thereby considerably influencing the ultimate shear strength. Some researchers (Tan and Cheng 2006, Tan et al 2008) had identified the dimensions of loading and support plates as one of the key factors on size effect. They explained it through the concept of a strut-and-tie approach. For geometrically-similar beams, the widths of diagonal struts and nodal zones remain unchanged if the widths of loading and support plates remain constant, regardless of an increase in the beam height *h*. Thus, as *h* increases, the capacities of nodal zones and struts are somehow constant, leading to the apparent observation that shear strength decreases with beam height *h* when shear strength is computed as $V/(bdf_c')$, where *b* is the beam width and *d* is the effective depth. The factor f_c' is to take account of slight variations in concrete strength among the specimens. Thus, size effect becomes apparent due to this definition (Collins and Kuchma 1999, Tan and Lu 1999, Yang et al 2003).

By keeping the loading plate width-to-beam depth ratio equal to 0.25, Walraven and Lehwalter (1994) tested two groups with different shear reinforcement ratios of

0.15 and 0.30 per cent, respectively. Again, size effect was found in both groups. This time, however, the effect is attributed to the uneven distribution of shear reinforcement for different beam sizes (Tan and Cheng 2006). Due to significant arch action in deep beams, the actual shear strength is greater than the predictions based on sectional approach (Tan and Lu 1999). But this enhancement varies with the effectiveness of arch action, which in turn depends on the geometry and boundary conditions of diagonal struts (Tan and Cheng 2006). The presence of web reinforcement helps mitigate this variation of shear strength in deep beams (Tan et al 2008, Bazant and Hsu-Huei 1987).

A common practice in experimental investigation of size effect of deep beams is to keep the beam width constant while increasing the beam height. It was implicitly assumed by researchers that the beam width has a negligible effect on the structural behaviour of deep beams. However, this conclusion is largely drawn from test results of stocky beams having small height-to-thickness (h/b) ratios.

In 1967, Kani (1967) compared the failure stresses of a series of 152 mm wide beams with 610 mm wide beams and came to the conclusion that the width of specimens had no effect on the failure shear stress. However, it should be noted that the h/b ratios of Kani's beams were only 0.5 and 1.8, much smaller than deep beam specimens tested nowadays, which easily exceed 10 and can be up to 67 (Kong et al 1986). Kotsovos and Pavlovic (1994) argued that it would be difficult to prevent the occurrence of out-of-plane actions when the beam cross section is very slim. They pointed out that small stresses induced by unintended out-of-plane actions may have a significant effect on beam strength. They proposed that the main cause of size effect was due to unintended out-of-plane actions. In Kani's (1967) specimens, the unintended out-of-plane action was negligible due to small h/b ratios (0.5 and 1.8). However, for deep beams with larger h/b ratios (but not large enough to cause buckling failure), it remains unknown whether the influence of unintended out-of-plane action on beam shear strength is negligible. Thus, there is a need to investigate this effect through an experimental programme.

5.2 Experimental Programme

5.2.1 Specimen Details

Three groups of concrete deep beams were designed, each consisting of four specimens with overall height h varied proportionally from 350 to 1000 mm, and loading and support plate width w_e from 52.5 to 150 mm. Beams were tested to failure under two point-loads applied with no load eccentricity. All specimens had the same a/d ratio at 1.1 and similar longitudinal reinforcement ratio ρ_s around 1.2%. Details of the specimens are summarised in **Table 5.1**.

Group 1 beams consisted of 1DB35bw, 1DB50bw, 1DB70bw and 1DB100bw. Lower case letter "b" denotes specimens with proportionally increasing beam width whereas "w" indicates with web reinforcement. The beam width b increased proportionally from 80 to 230 mm with overall height h from 350 to 1000mm, maintaining the same h/b ratio of 4.4 for the four specimens in Group 1. Web reinforcement was provided for this group of beams to sustain additional stresses caused by "unintended load eccentricity" so as to minimize the influence of unintended out-of-plane actions. This was perceived as one possible cause of size effect at the onset of the experimental investigation. Web steel bars were distributed evenly within the shear span and web steel ratio ρ_{sw} was maintained around 0.4%.

Table 5.1 Summary of specimen details

Beam Designation	Beam width b (mm)	Overall height h (mm)	Effective depth d (mm)	Width of loading & support plate w_e (mm)	Bottom Reinforcement A_s (mm^2)	Web Reinforcement A_{sw} (mm^2)	ρ_s (%)	ρ_{sw} (%)	a/d	h/b	f_c' (MPa)
1DB35bw	80	350	313	52.5	314 (4T10)	113 (2R6)	1.25	0.40	1.1	4.4	25.9
1DB50bw	115	500	454	75	668 (2T16+2T13)	226 (4R6)	1.28	0.39	1.1	4.4	27.4
1DB70bw	160	700	642	105	1257 (4T20)	503 (5R8)	1.22	0.45	1.1	4.4	28.3
1DB100bw	230	1000	904	150	2502 (2T25+4T22)	942 (6R10)	1.20	0.41	1.1	4.4	28.7
2DB35	80	350	314	52.5	314 (4T10)	-	1.25	0	1.1	4.4	27.4
2DB50	80	500	459	75	423 (2T13+2T10)	-	1.15	0	1.1	6.3	32.4
2DB70	80	700	650	105	668 (2T16+2T13)	-	1.28	0	1.1	8.8	24.8
2DB100	80	1000	926	150	933 (2T16+4T13)	-	1.26	0	1.1	12.5	30.6
3DB35b	80	350	314	52.5	314 (4T10)	-	1.25	0	1.1	4.4	27.4
3DB50b	115	500	454	75	668 (2T16+2T13)	-	1.28	0	1.1	4.4	28.3
3DB70b	160	700	642	105	1257 (4T20)	-	1.22	0	1.1	4.4	28.7
3DB100b	230	1000	904	150	2502 (2T25+4T22)	-	1.20	0	1.1	4.4	29.3

Group 2 specimens, consisting of 2DB35, 2DB50, 2DB70 and 2DB100, had a constant beam width b at 80 mm as h increased from 350 to 1000 mm. Thus, the beam h/b ratio grew from 4.4 to 12.5 accordingly as beam height increased. No web reinforcement was provided for this group of beams.

Group 3 beams, comprising 3DB35b, 3DB50b, 3DB70b and 3DB100b, were similar to Group 1 beams except they did not have web reinforcement. It should be noted that the two specimens 2DB35 and 3DB35b were identical; therefore only one beam was fabricated and tested to obtain the experimental result used in both groups. By comparing Group 1 and Group 3 beams, the effect of web reinforcement on beam strength and size effect can be studied.

Table 5.2 Summary of steel bar properties

Type of Rebars	Nominal yield stress f_y (MPa)	Nominal ultimate stress f_u (MPa)	Young's Modulus E (GPa)
R6	426	488	195
R8	370	472	199
R10	455	522	190
T10	469	622	198
T13	520	611	190
T16	499	648	194
T20	522	592	193
T22	520	614	197
T25	555	639	193

Note: The number following R or T indicates the nominal diameter of the reinforcement bar.

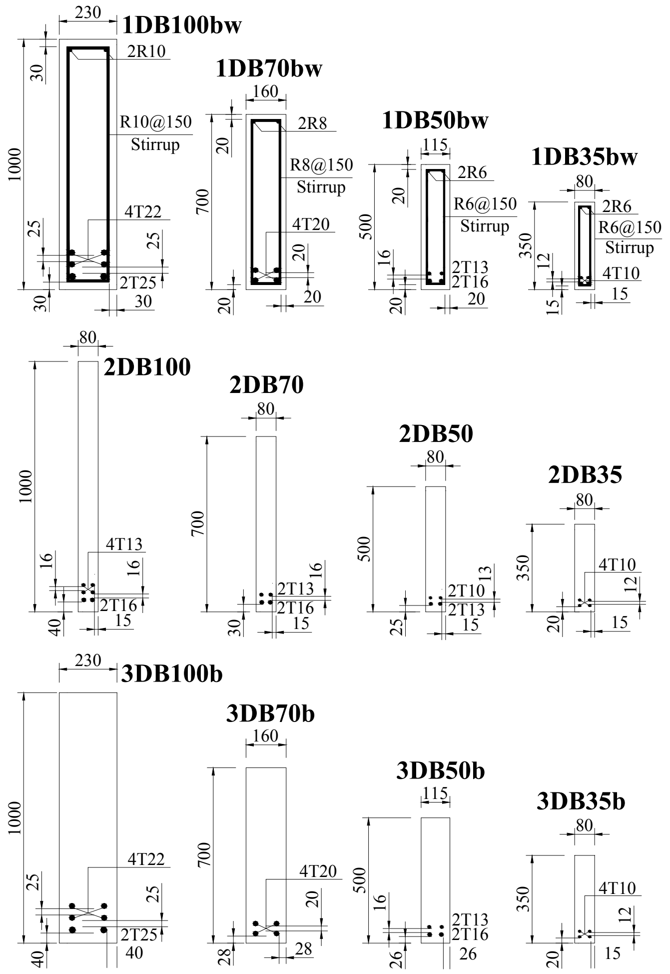

Figure 5.1 Beam cross sections of 3 groups of beams

Note: The number following R or T indicates the nominal diameter of the reinforcement bar.

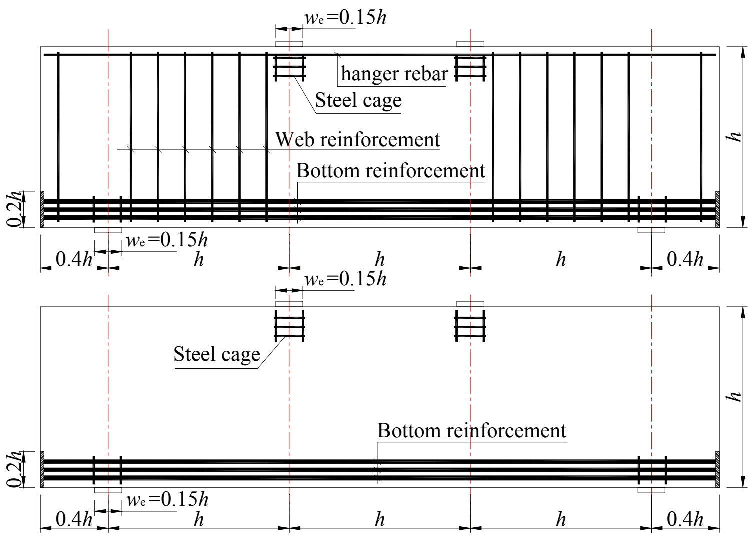

Figure 5.2 Typical reinforcement layout for specimens with and without web rebars

By comparing Group 2 and Group 3 specimens, the effect of beam width and unintended out-of-plane action on beam strength and size effect (if any) can be delineated. Finally, through comparison of Group 1 and Group 2 results, one can investigate if out-of-plane action and web reinforcement play an important role on size effect.

The geometrical properties and reinforcement details of all the specimens are shown in **Figure 5.1** and **Figure 5.2**. All the bottom longitudinal bars were welded to anchorage plates at both ends of the beam. For Group 1 beams, no web reinforcement was provided in the region in between the two loading points. Local reinforcement cages were placed at the locations of loading or support points to guard against premature crushing. Loading and support plate width was kept proportional to the beam height. Specimens were cast using the same batch of concrete.

Chippings of 10 mm size were used instead of normal-size aggregates to prevent segregation of concrete at the bottom of the beam. The concrete cylinder compressive strength f_c' of each beam is given in **Table 5.1**, ranging from 24.8 to 32.4 MPa. The concrete is classified as medium strength. The values of f_c' were obtained from the mean values of three 150 mm x 300 mm concrete cylinders cured under the same conditions and tested on the same day as the specimens.

Two types of reinforcement were used in the beams, namely, deformed high tensile steel (T bar) and plain round mild steel (R bar). T bars were used for main longitudinal reinforcement and R bars for vertical web reinforcement. To obtain the same main reinforcement ratio ρ_s for all beams, six bar sizes were used, i.e. T10, 13, 16, 20, 22 and 25. The web rebars consisted of R6, 8 and 10 bars as stirrups. Tested steel bar properties including yield and ultimate strengths as well as young's modulus are summarised in **Figure 5.1**. These are average values obtained from 3 samples of 600 mm long tensile coupons for each type of steel bar.

5.3.2 Instrumentation and Test Setup

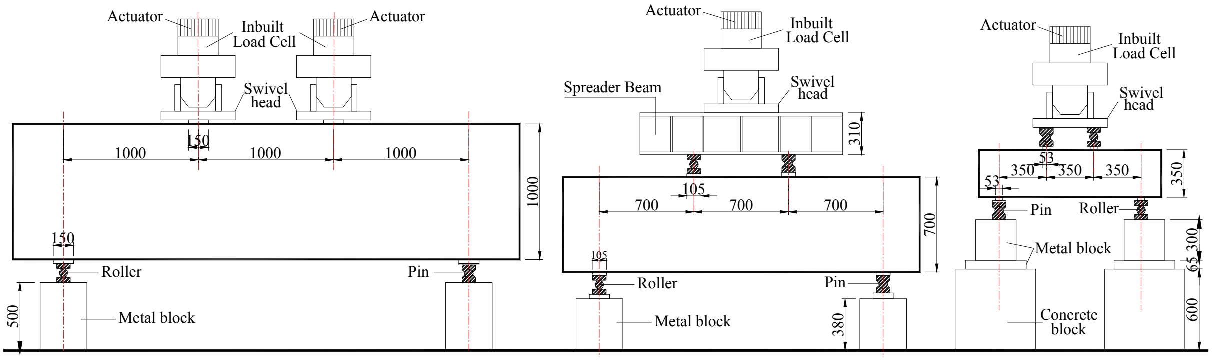

Figure 5.3 Typical test setup for large, medium and small beams4

Typical experimental set-ups are shown in **Figure 5.3** for testing large, medium and small size beams. All the specimens were simply supported. For large beams (h = 1000 mm), the two point-loads were applied by two 100-ton actuators. For medium beams (h = 500, 700 mm), a steel spreader beam was used to effect two equal loads. For small beams (h = 350 mm), the swivel head of the actuator served as a spreader beam. The computer-driven actuator can be toggled between the load- or displacement-control mode. The spreader beam was seated on one pin and one roller support placed on top of the specimen. Loading positions were calibrated with a mini-laser projector to avoid any load eccentricity both in- and out-of-plane of the beams. For specimens 2DB70 and 2DB100, five 25 mm LVDTs were provided along the diagonal strut on each face of the beam to record out-of-plane displacement. Typical configuration of the LVDTs is shown in **Figure 5.4**, indicated by a capital letter "L" followed by a sequence number.

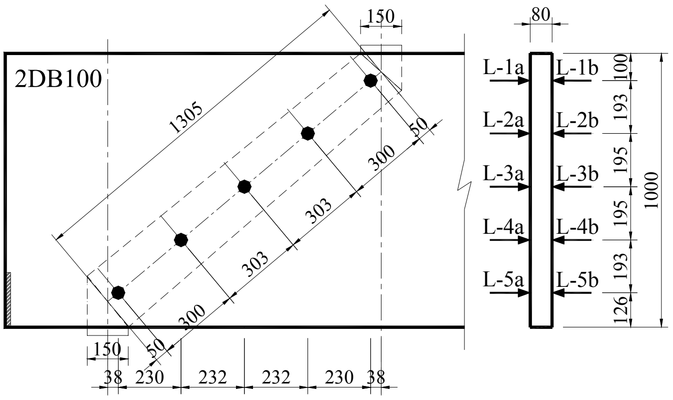

Figure 5.4 Typical LVDT configurations for measuring beam out-of-plane displacement

Load-control mode was first adopted at an increment of 10 kN before any flexural crack was detected on the beam surface. Thereafter, load increment was increased to 20 – 40 kN, depending on the beam capacity, until the total load reached around 75% of predicted failure load from finite element analysis. Then the actuator was toggled to displacement-control mode to prevent the specimen failing in a sudden manner.

5.3 Experimental Results and Discussion

5.3.1 Crack Patterns

The crack patterns of the three groups of specimen at failure are shown in **Figure 5.5**, **Figure 5.6** and **Figure 5.7**, respectively. It is seen that the crack patterns of beams with web reinforcement in Group 1 (**Figure 5.5**) are more extensively developed than their counterparts without web reinforcement in Group 2 and Group 3 (**Figure 5.6** and **Figure 5.7**), exhibiting enhanced shear capacity. The failure crack patterns of the four beams within each group are similar, showing little dependence on the beam size. All specimens fail in shear-compression mode (**Table 5.3**).

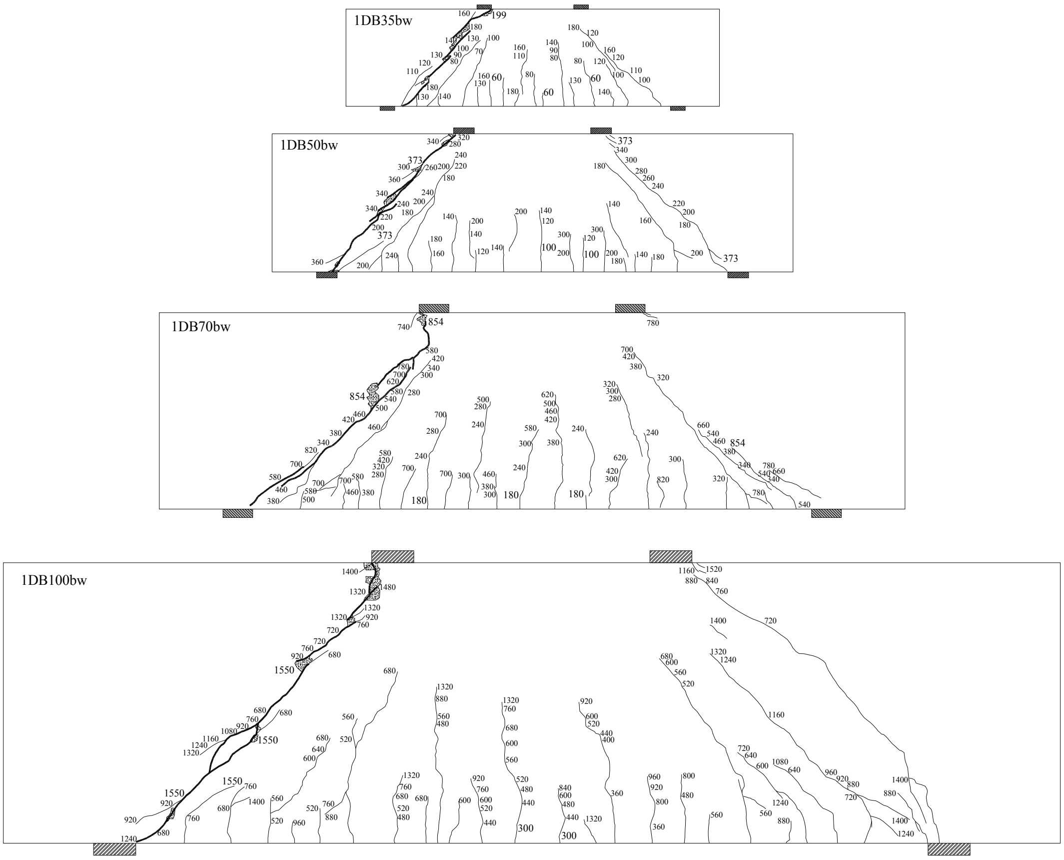

Figure 5.5 Crack patterns for Group 1 specimens

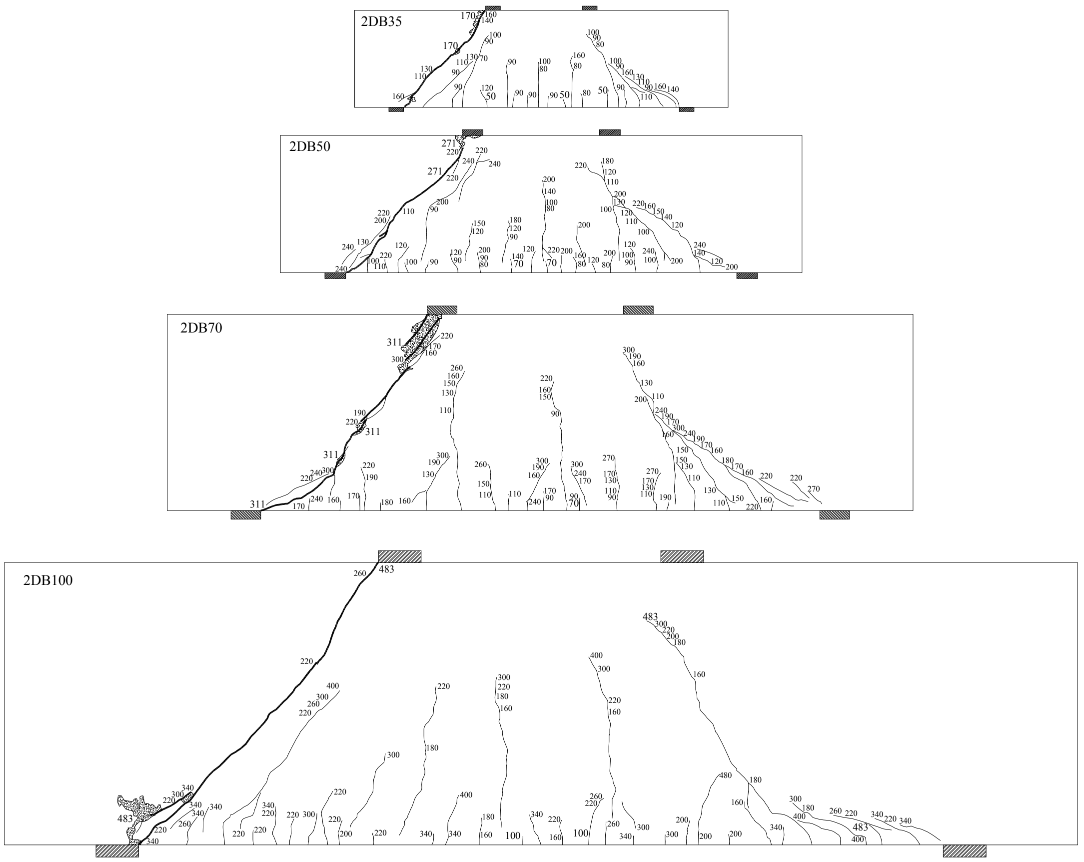

Figure 5.6 Crack patterns for Group 2 specimens

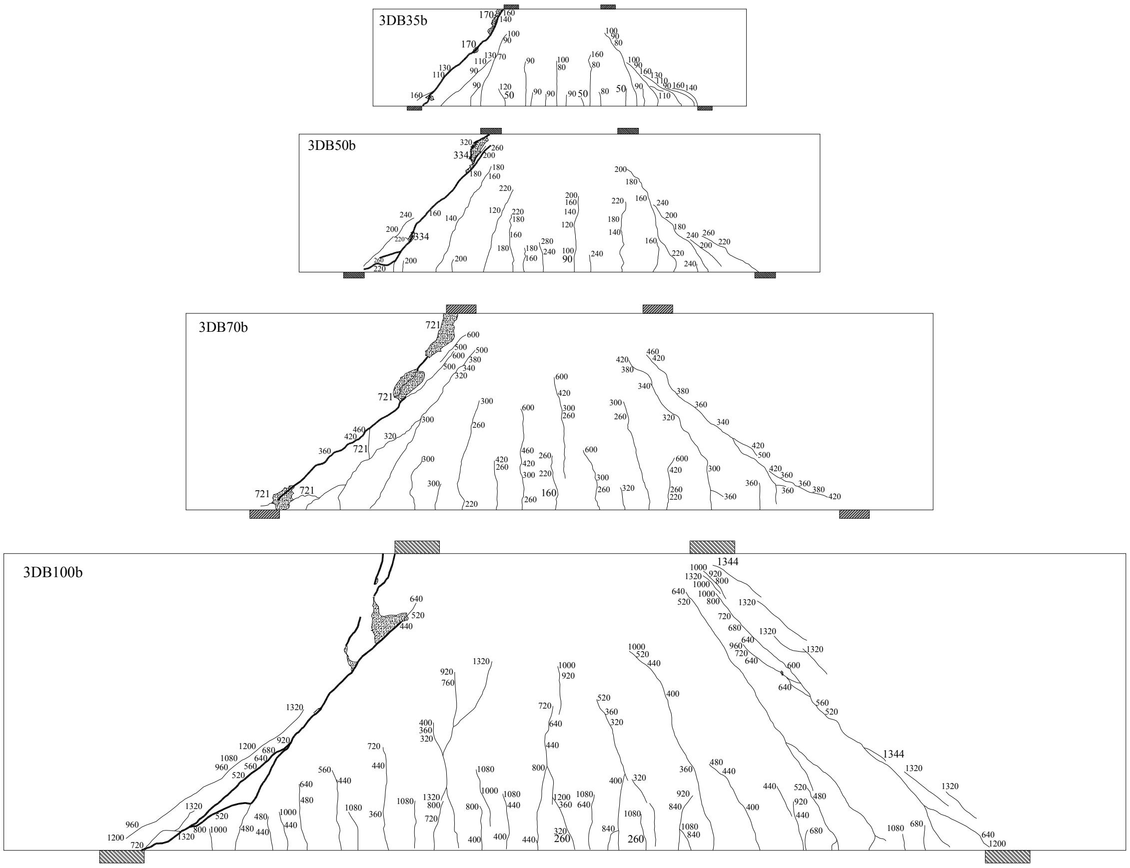

Figure 5.7 Crack patterns for Group 3 specimens

Table 5.3 Summary of experimental results

Beam Designation	Failure Load $2V_n^{exp}$ (kN)	Initial flexural cracking load $2V_{cr}$ (kN)	Initial diagonal crack load $2V_d$ (kN)	Serviceability Load $2V_{ser}$ (kN)	V_d / V_n^{exp}	Failure Mode
1DB35bw	199	60	80	120	0.40	SC
1DB50bw	373	100	160	240	0.43	SC
1DB70bw	854	180	280	460	0.33	SC
1DB100bw	1550	300	680	880	0.44	SC
2DB35	170	50	90	120	0.53	SC
2DB50	271	70	110	160	0.41	SC
2DB70	311	70	160	160	0.51	SC
2DB100	483	100	220	220	0.46	SC
3DB35b	170	50	90	120	0.53	SC
3DB50b	334	90	160	200	0.48	SC
3DB70b	721	160	320	360	0.44	SC
3DB100b	1344	260	440	600	0.33	SC

Note: SC = Shear Compression.

It was argued (Bazant and Kim 1984, Bazant and Kazemi 1991) that size effect induced by energy release would be evidenced by greater crack propagation rates for larger size beams. Contrary to previous observations on shallow beams (Walraven 1978) or deep beams with constant support and loading plate width (Tan and Lu 1999), the propagation rate of diagonal cracks is about the same for different sizes of beams in all three groups, as shown in **Figure 5.8**. All beams in the figure are under the same dimensionless shear stress $v = V/(bdf_c')= 0.10$, represented as equally large and with failure shear span orientated to the left for ease of comparison. Beams on the top left refer to Group 1 beams, those on the top right and on the bottom left refer to Group 2 and 3 beams, respectively.

Generally, flexural cracks are finely distributed in the vicinity of bottom reinforcement, indicating mobilization of bottom longitudinal steel as a tie member. By comparing crack patterns within each group, it is seen that flexural cracks appear to be more developed as the beam size increases, indicating greater energy release in flexural actions.

However, the development of diagonal cracks at failure (left) shear span is found almost uniform within each group, even for those beams without web reinforcement (Group 2 and Group 3). In deep beams, arch action rather than flexure dominates the beam behaviour. The more-or-less uniform propagation rate observed for diagonal cracks among beams of different sizes indicates that size effect is not significant for these specially-designed specimens. It is seen for Group 2 and 3 beams (top right and bottom left in **Figure 5.8**) that the diagonal cracks at failure (left) shear span generally reach the full depth of the beams, regardless of beam size, showing little difference in the propagation rate. Similarly, little difference in the propagation rate of diagonal cracks is observed for Group 1 beams (top left in **Figure 5.8**). However, compared to Group 2 and 3, the diagonal cracks at failure (left) shear span of Group 1 generally do not develop fully across the beam depth, showing the effectiveness of web reinforcement in restraining crack propagation.

On closer examination, the cracking patterns of Group 3 beams with proportionally enlarged dimensions in 3-D are more developed compared to Group 2 beams with constant beam width.

5.3.2 Load-deflection Response

The load-versus-mid-span deflection curves of specimens are plotted in groups and displayed on the left in **Figure 5.9**. The settlements of supports have been excluded from the mid-span deflections of beams. As seen from the figure, the 1000 mm high beams exhibit the steepest gradient of load-deflection curve whereas the 350 mm high beams the gentlest. As *h* increases, the mid-span deflection Δ_{mid} becomes greater. This was observed in all three groups.

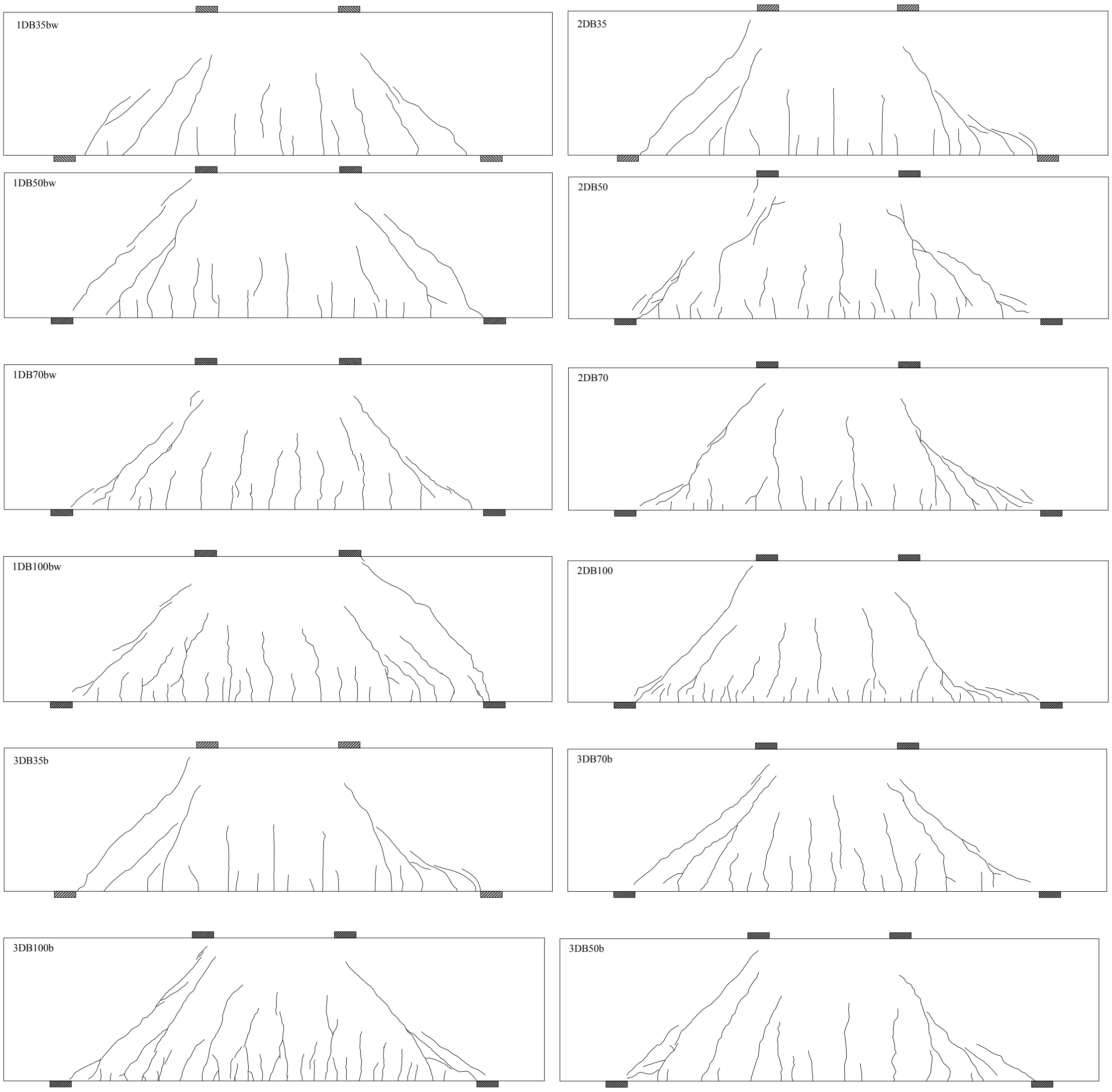

Figure 5.8 Crack development in beams with various heights, represented as equally large, at $v = 0.10$

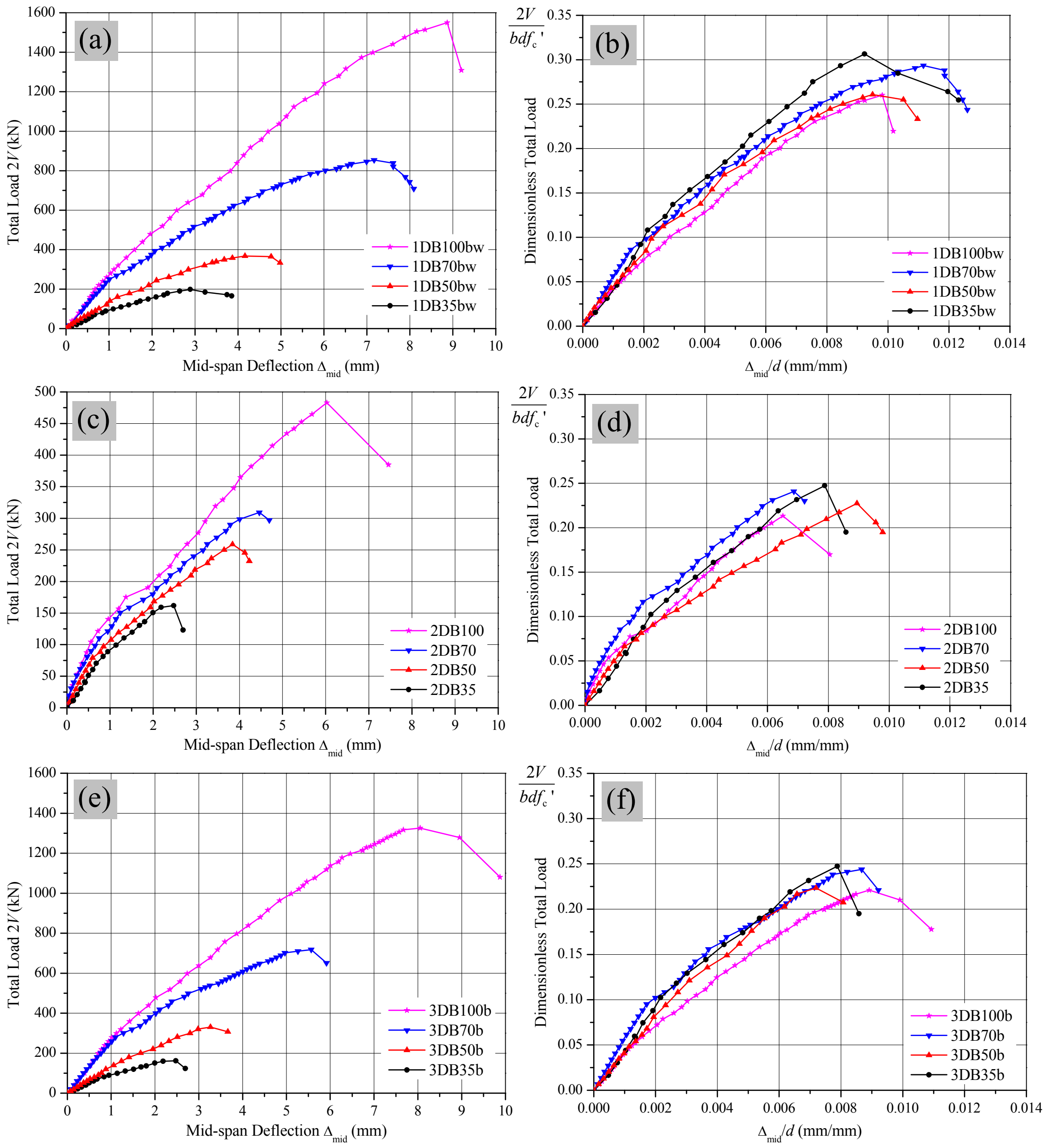

Figure 5.9 Load versus mid-span deflection curves for specimens

For the ease of comparison, normalised load-deflection curves with dimensionless load ($2V/(bdf_c')$) as y-axis and deflection (Δ_{mid}/d) as x-axis are presented on the right in **Figure 5.9**. It is shown that the normalised curves of different beam sizes are comparable to one another within each group. The beams exhibit relatively similar behaviour within each group, regardless of beam height. Comparing Group 1 beams (**Figure 5.9**b) with Group 2 (**Figure 5.9**d), it shows that evenly-spaced web reinforcement further reduces the differences in load-deflection behaviour among beams of different heights.

Furthermore, with web reinforcement, the normalised deflection Δ_{mid}/h at failure increases from 0.008 mm/mm to around 0.011 mm/mm. That is, web reinforcement gives an average improved ductility of 38%. However, web reinforcement has little effect on the beam stiffness itself. Generally, for beams of the same height, there are no observable differences in load-deflection curves between specimens with or without web reinforcement (**Figure 5.9**a, **10**e). Notwithstanding that, web rebars significantly increase the ultimate shear strength for all beams. Comparing Group 2 with Group 3, it shows that beam width significantly influences the beam load-deflection response (**Figure 5.9**c, **10**e). However, based on normalised load-versus-deflection curves, the two groups of beams exhibit comparable dimensionless load-deflection responses (**Figure 5.9**d, **10**f), showing negligible influence of beam width on ultimate strength.

5.3.3 Cracking, Serviceability and Ultimate Beam Strengths

The cracking loads, serviceability loads, ultimate loads and failure modes of all the specimens are summarised in **Table 5.3.** Generally, beams with web reinforcement have a smaller diagonal-cracking-to-failure-load ratio ($V_{\mathrm{d}}/V_{\mathrm{n}}^{\mathrm{exp}}$) averaged around 0.40, comparing to around 0.46 for beams without web reinforcement. It reflects a higher reserve capacity developed in deep beams after diagonal cracking due to the presence of web reinforcement. The dimensionless flexural cracking load $V_{\mathrm{cr}}/(f_{\mathrm{c}}'bh)$ and serviceability load $V_{\mathrm{ser}}/(f_{\mathrm{c}}'b_{\mathrm{w}}h)$ of the beams are plotted together against effective depth d for all three groups of beams in **Figure 5.10**a. Flexural cracking strength decreases as *d* increases, showing a “size effect”. This may be due to a quicker energy release by flexural cracks in larger beams, backed by experimental observation that greater propagation rate of flexural cracks took place in larger beams (**Figure 5.8**). Serviceability limit of cracking (0.3 mm) was reached by widening of diagonal cracks or inclined cracks in the specimens. Beams with web reinforcement (Group 1) have higher serviceability loads than beams with plain concrete web (Group 2 and 3). This is because web rebars resist tensile stresses in cracked concrete and deter the widening of crack width.

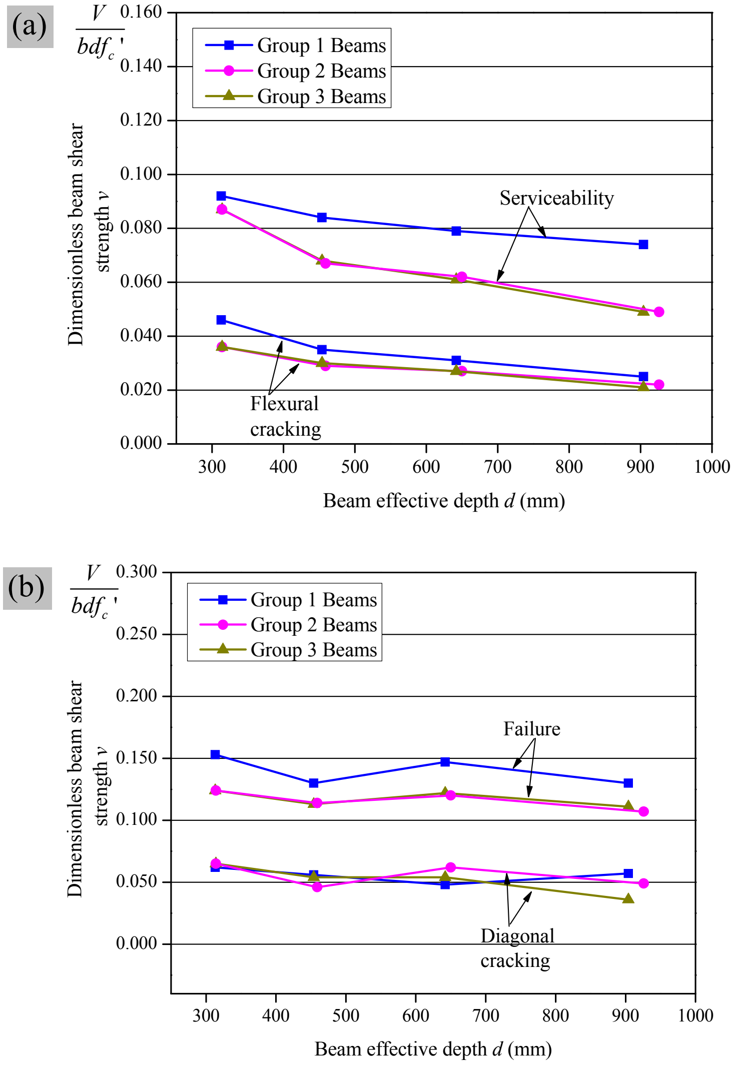

Figure 5.10 Experimental beam shear strengths (a) at flexural cracking and serviceability; (b) at diagonal cracking and failure versus beam effective depth

Moreover, it is clear that Group 1 beams with evenly distributed web reinforcement exhibit less "size effect" in serviceability load when compared to Group 2 and 3 beams without web reinforcement (**Figure 5.10**a). It lends experimental support to the hypothesis that evenly distributed web reinforcement improves the boundary conditions of the diagonal struts (**Figure 2.18**) and mitigates the size effect.

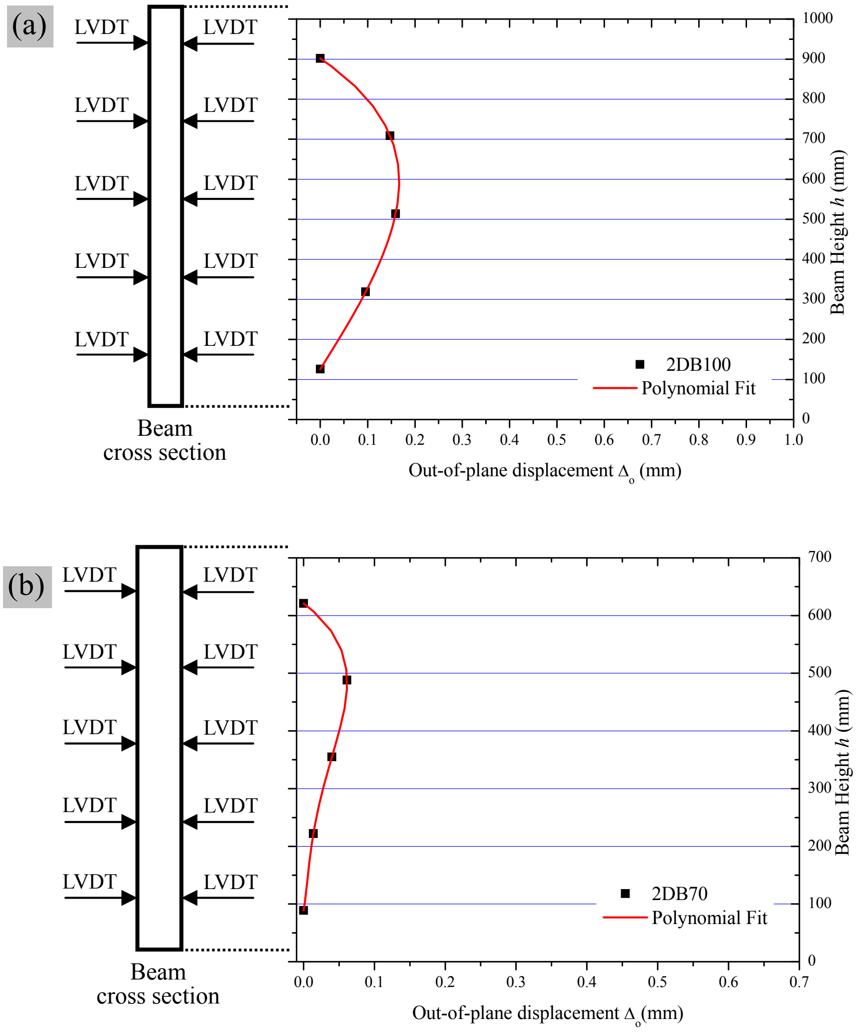

Figure 5.11 Out-of-plane displacement of specimen (a) 2DB100; (b) 2DB70 at failure

The dimensionless diagonal cracking load $V_d/(f_c'b_wh)$ and failure load $V_n^{exp}/(f_c'bh)$ are also plotted against d for all the beams in **Figure 5.10**b. Generally, test results exhibit three almost coincidental flat curves of diagonal cracking strength with increasing *d* for all three groups. This result conforms to previous findings (ACI 318-05, Collins and Kuchma 1999, Tan and Lu 1999) that the diagonal cracking strengths of deep beams are not size-dependent. The presence of web reinforcement does not influence the magnitude of diagonal cracking strength. **Figure 5.10**b shows the curves of ultimate shear strengths versus *d*. Interestingly, all three groups exhibit a flat trend, indicating insignificant "size effect". By configuring the loading and support plate width to be proportional to the beam height, the size effect is significantly mitigated, even for Group 2 beams with no web reinforcement and much higher h/b ratios. Thus, it can be concluded that strut geometry plays a dominant role in mitigating the size effect in ultimate shear strength of deep beams.

Group 1 beams consistently display higher shear strength (20% in average) than beams in Group 2 and 3, showing a significant effect of web reinforcement on enhancing shear strengths of deep beams. Beams of the same height in Group 2 and 3 have nearly the same shear strengths, making the two curves almost indistinguishable in **Figure 5.10**b. This experimentally validates Kani's (1967) conclusion on stocky shallow beams, that "beam width has negligible influence on beam shear strength", is also applicable to deep beams with h/b ratio up to 12.5.

Out-of-plane displacements Δ_o along the diagonal strut (**Figure 5.4**) are measured for specimen 2DB70 (h/b = 8.8) and 2DB100 (h/b = 12.5) and plotted out in **Figure 5.11**. Although specimens were tested with no intended load eccentricity, out-of-plane displacements were still observed in the test, albeit with very small magnitude. This may be due to the heterogeneous nature of concrete and unavoidable error in test setup. The maximum Δ_o/h ratios at beam failure were recorded as 1.7:10000 for 2DB100 and 0.9:10000 for 2DB70, respectively. Applying the strut-and-tie concept (**Figure 2.18**), under the ultimate load, the measured out-of-plane displacement would result in additional bending moment in the strut and increase the maximum compressive stress in diagonal strut up to 0.3 MPa and 0.1 MPa for 2DB100 and 2DB70, respectively. Clearly, such small additional stresses have negligible effect on beam strength compared to f_c' around 30 MPa and can be safely ignored.

Table 5.4 Summary of FEM predictions

Beam Designation	$2V_n^{FEM}$ (proportional plate width)	Predicted Failure Mode (proportional plate width)	$2V_n^{cFEM}$ (constant plate width)	Predicted Failure Mode (constant plate width)	Failure Load $2V_n^{exp}$ (kN)	V_n^{FEM}/V_n^{exp}	V_n^{cFEM}/V_n^{exp}
1DB35bw	184.7	shear	184.7	shear	199	0.93	0.93
1DB50bw	399.2	compression and shear	376.0	compression and shear	373	1.07	1.01
1DB70bw	750.1	compression and shear	701.0	compression and shear	854	0.88	0.82
1DB100bw	1530.0	shear	1260.0	shear	1550	0.99	0.81
2DB35	162.9	shear	162.9	shear	170	0.96	0.96
2DB50	257.1	shear and tension	241.0	shear and tension	271	0.95	0.89
2DB70	298.7	shear	242.4	shear	311	0.96	0.78
2DB100	515.0	shear	336.9	shear	483	1.07	0.70
3DB35b	162.9	shear	162.9	shear	170	0.96	0.96
3DB50b	355.1	shear	308.5	shear	334	1.06	0.92
3DB70b	667.0	shear	590.8	shear	721	0.93	0.82
3DB100b	1350.0	shear	973.4	shear	1344	1.00	0.72
Mean						0.98	0.86
SD						0.061	0.099
COV						0.063	0.115

The finite element analysis is carried out to investigate the effects of loading and support plate on beam shear strength. Two comparison studies are carried out. Firstly the specimens are analysed under proportional loading and support plate widths. The FEM results are shown in the second column of **Table 5.4**, with an average prediction-to-test-result ratio of 0.98 and a COV of 0.063.

The predicted failure modes of the specimens are generally consistent with test results and are summarised in the third column of **Table 5.4.** The FEM-predicted ultimate shear strengths $V_n^{FEM}/(bdf_c')$ are plotted against effective depth d in **Figure 5.12**a, which shows insignificant size effect for all groups (a similar trend in **Figure 5.10**(b) - failure curves). In the second numerical study, all modelling parameters are maintained the same as in the first study, except that the loading and support plate widths are kept constant at 52.5 mm for all specimens. The analysis results show that although the failure modes remain unchanged, the beams exhibit reduced ultimate strengths due to smaller plate size (the fourth and fifth column in **Table 5.4**). Plotting out the FEM (with constant plate width) predicted shear strength $V_n^{cFEM}/(bdf_c')$ against d, it is seen that all three groups exhibit a clearer size effect (**Figure 5.12**b). It indicates that strut geometry, which is determined by the dimensions of loading and support plates and the strut length, will influence ultimate shear strength and lead to apparent size effect. This conclusion has also been confirmed in a recent experimental study (Tan et al 2008).

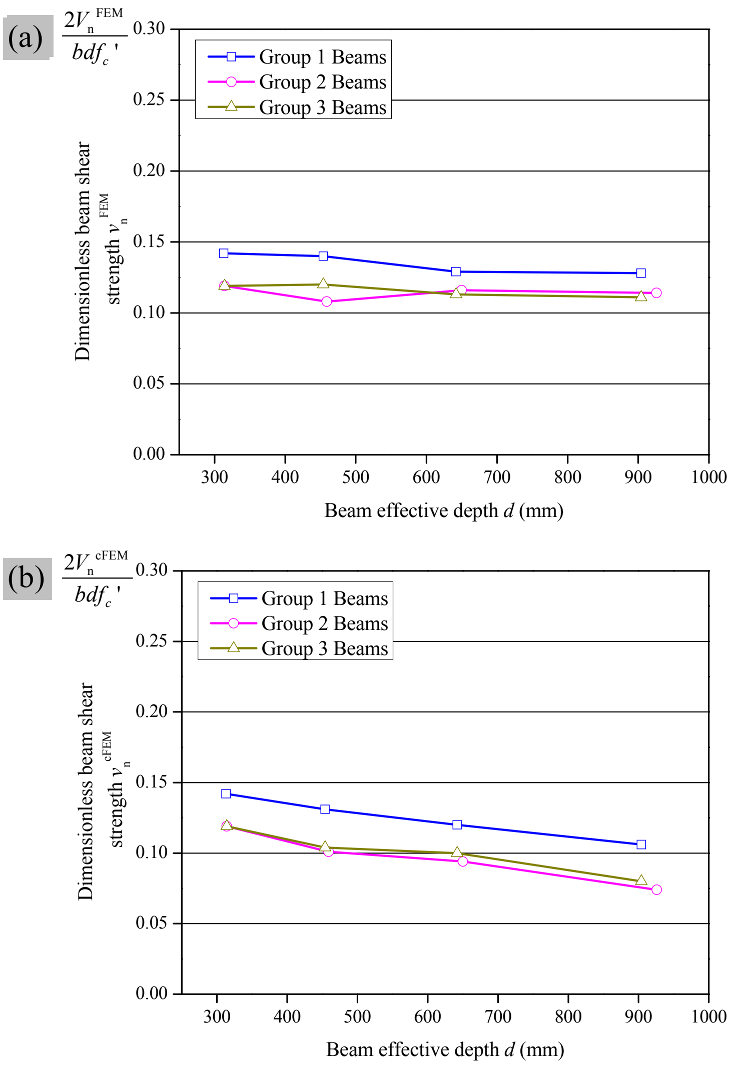

Figure 5.12 FEM-predicted ultimate shear strengths versus beam effective for specimens (a) with proportional plate width; (b) with constant plate width depth

5.4 Verification of Proposed STM

The ultimate shear strengths of 11 specimens (**Table 5.1**) have been evaluated by the original STM (Eq.(2.67)) and the proposed modified STM (Eq.(2.71)). Besides, for comparison purpose, the strut-and-tie method documented in ACI 318-05 and the CSA 23.3-94 approach based on strut-and-tie concept are also used to calculate the shear capacities of these specimens. The comparison results are summarised in **Table 5.5**. The average and coefficient of variation (COV) of prediction-to-experiment-result ratios are also reported in the table. It appears that the ACI 318-05 slightly underestimates the beam strengths whereas original STM slightly overestimates the beam strengths. The CSA 1994 gives best agreement of 0.88 in the mean value and 0.109 in COV. Modified STM gives the mean value of 0.82 and the lowest COV of 0.061. Modified STM improves both the accuracy and consistency in predictions when compared with original STM because the mean value is reduced from 1.06 to 0.82 while COV is 29% lower.

The predicted shear strengths by original STM (V_n^{STM}) and modified STM (V_n^{mSTM}) are plotted together with experimental results (V_n^{exp}) against *d* in the dimensionless coordinate (**Figure 5.13**) for three groups of beams. For Group 1 beams, both models exhibit almost the same trend of predictions as test results (**Figure 5.13**a). Not much improvement is seen on modified model predictions, as the strut geometry and boundary conditions are properly configured for this group of beams. However, the differences in predictions for the two STM models for Group 2 and 3 beams are clearly seen in (**Figure 5.13**b, **14**c), where original model tends to overestimate beam shear strength as *d* increases. Modified model improves the prediction accuracy by taking into account the effects of strut geometry (Eq. (2.69)) and strut boundary conditions (Eq. (2.70)).

Table 5.5 Summary of predictions on beam shear strength

Beam Designation	$2V_n^{exp}$ (kN)	$2V_n^{ACI}$ (kN)	$2V_n^{CSA}$ (kN)	$2V_n^{STM}$ (kN)	$2V_n^{mSTM}$ (kN)	V_n^{ACI}/V_n^{exp}	V_n^{CSA}/V_n^{exp}	V_n^{STM}/V_n^{exp}	V_n^{mSTM}/V_n^{exp}
1DB35bw	199	172	163	187	144	0.86	0.82	0.94	0.72
1DB50bw	373	327	317	407	310	0.88	0.85	1.09	0.83
1DB70bw	854	605	598	786	601	0.71	0.70	0.92	0.70
1DB100bw	1550	1342	1328	1660	1280	0.87	0.86	1.07	0.83

2DB35	170	136	169	177	141	0.80	1.00	1.04	0.83
2DB50	271	162	230	262	210	0.60	0.85	0.97	0.77
2DB70	311	225	248	354	265	0.72	0.80	1.14	0.85
2DB100	483	327	439	547	425	0.68	0.91	1.13	0.88
3DB35b	170	137	169	177	141	0.80	1.00	1.04	0.83
3DB50b	334	263	327	391	304	0.79	0.98	1.17	0.91
3DB70b	721	485	606	752	583	0.67	0.84	1.04	0.81
3DB100b	1344	916	1358	1576	1238	0.68	1.01	1.17	0.92
Mean						0.76	0.88	1.06	0.82
SD						0.091	0.096	0.090	0.050
COV						0.120	0.109	0.085	0.061

Note: V_n^{ACI} = predictions by ACI 318-05 Appendix A; V_n^{CSA} = predictions by CSA 1994 code; V_n^{STM} = predictions by original STM; V_n^{mSTM} = predictions by modified STM.

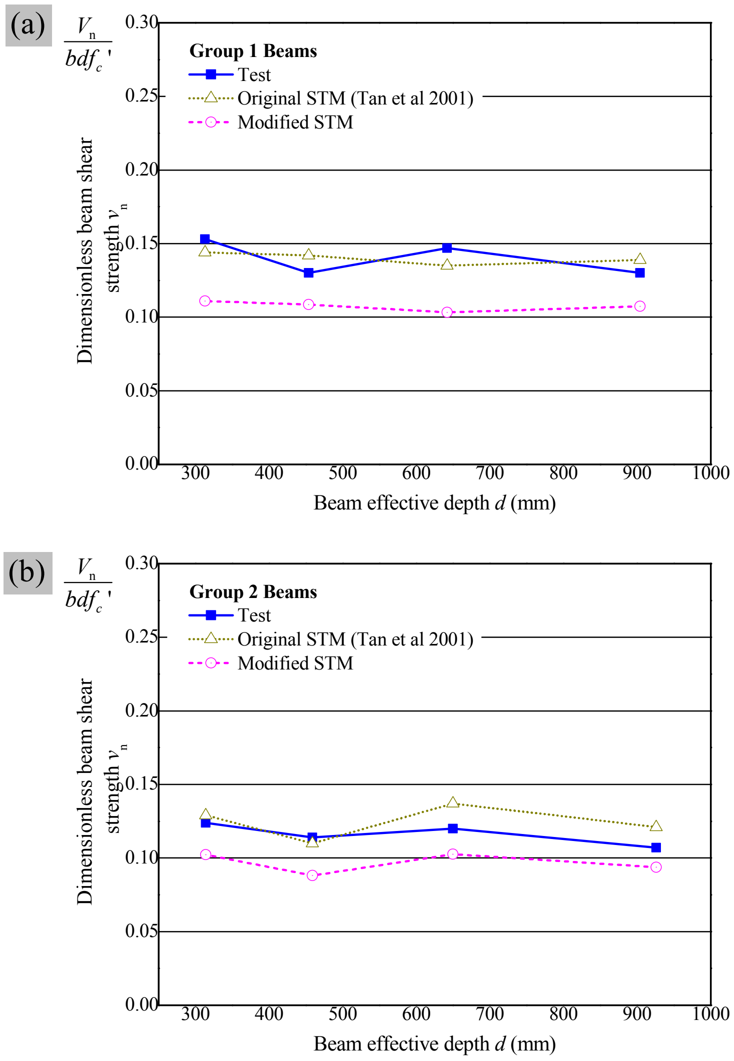

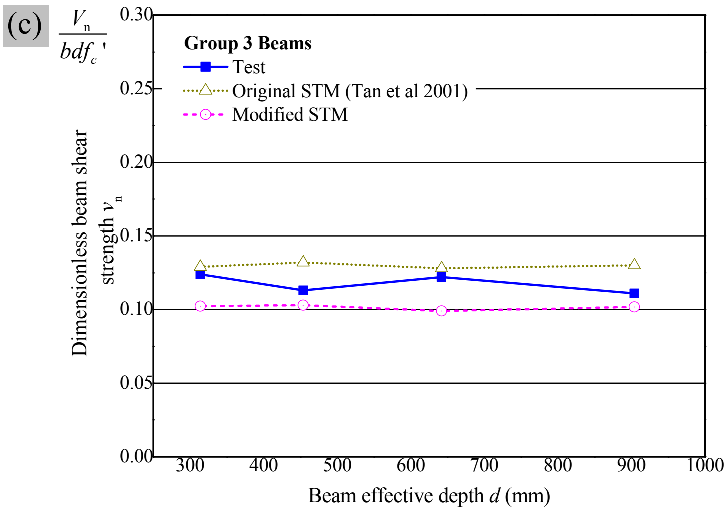

Figure 5.13 Beam shear strength versus beam effective depth for (a) Group 1; (b) Group 2; (c) Group 3 specimens

5.5 Summary

This chapter presented the findings of an experimental programme devised to investigate the size effect in deep beams. Beam width was shown to have negligible influence on shear strength for slender deep beams with *h*/*b* ratio up to 12.5. However, it did have some limited effect on crack development. Unintended out-of-plane actions had minimal effect on shear strengths, under a properly-controlled testing environment.

Interestingly, flexural cracking strengths of deep beams exhibited small degree of “size effect”, which conformed to the observations that larger beams showed greater propagation rate of flexural cracks. However, at the ultimate state, arch action rather than flexure dominated the deep beam behaviour. Thus, the so-called “size effect” in flexure has little effect on shear strength.

The most important conclusions are that the factors that influenced the ultimate strength of a compression member governed the size effect, i.e. strut geometry and boundary condition. No substantial difference was seen in the propagation rate of diagonal cracks among beams of different sizes, indicating insignificant size effect. By properly configuring the dimensions of loading and support plates, the size effect in ultimate shear strength is significantly mitigated, even for beams with higher h/b ratios and plain concrete web. It suggested that properly configured strut geometry played a dominant role in mitigating size effect.

Serviceability strengths of Group 1 beams exhibited much less size effect compared to Group 2 and 3 beams, indicating that evenly distributed web reinforcement also played an important role in mitigating size effect in deep beams.

The proposed modified STM in Chapter 2 incorporating causes of size effect was used to calculate the specimens for the test programme. The modified model yielded better agreement than the original STM (Tan et al 2003) in terms of accuracy and consistency. Through the modified STM and the test programme, the author hoped this work may shed light on the interesting phenomenon of size effect on deep beams.

CHAPTER 6 CONCLUSIONS AND RECOMMENDATIONS

6.1 Conclusions

This research investigated the behaviour and strength of deep beams subjected to various loadings and support conditions and proposed corresponding strut-and-tie models for the deep beams.

Firstly, a modified Strut-and-Tie Model (STM) for SSDBs was developed. It adopted Kupfer's failure criterion and required no empirical stress limits in struts and nodal zones. The model was evaluated using 233 test results collected from the literature. It outperformed the original STM (Tan et al. 2001, 2003) as well as the ACI strut-and-tie approach in predicting shear strength for better accuracy and consistency. The influence of stress distribution factor k on the model predictions was studied numerically and $k = 4$ derived from linear stress distribution assumption was shown sufficiently accurate for predicting the deep beam shear strength. The modified model also embedded a softening effect in concrete compressive strength due to transverse tensile strain, comparable to that obtained from MCFT and Belarbi and Hsu's equations. The modified STM was further extended to predict the ultimate strengths of concrete continuous deep beams (CDBs) for the first time. The predictions of the STM for CDBs including beam strengths and support reactions were in good agreement with a total of 54 test results of concrete CDBs.

Then the STM for CDBs was further developed to calculate the ultimate strength of CDBs subjected to support settlements. The proposed model was evaluated by the author's test programme consisting of six medium-strength RC CDBs with configured

K values ranging from 83 to 436 kN/mm and with or without web reinforcement. The model predictions for support reactions and ultimate beam strengths were in good agreement with test results. The model correctly predicted the critical middle support stiffness K_{cri}, below which the top member of STM transformed from a tension tie to a compression strut, which was backed by experimental observations in strain measurements and crack patterns.

An experimental programme devised to investigate the effects of differential support settlement on the strength and behaviour of CDBs was carried out. Support settlement significantly influenced the cracking behaviour and crack patterns of CDBs. The crack patterns of beams with web reinforcement were more extensively developed than those without. Support settlement significantly reduced the serviceability load and beam stiffness. However, the reduction in ultimate strength was not significant, particularly for beams with web reinforcement. Nevertheless, the failure zone shifted from interior shear span to exterior as the middle support stiffness K fell below critical support stiffness K_{cri}. Web reinforcement significantly enhanced the beam capacity, though it had little effect on beam stiffness. For specimens with K lesser than the critical support stiffness (i.e. $K < K_{\mathrm{cri}}$), the bottom reinforcement yielded at failure whereas the top reinforcement was in compression throughout the test. The exterior shear span reached its shear capacity prior to the interior shear span and led to the failure of the beam. The distribution of support reactions was significantly affected by the middle support stiffness K. As K decreased, the middle support attracted lesser load while the end supports took more, suggesting a considerable redistribution of beam internal forces.

The modified STM for SSDBs was also developed to determine the strengths and the failure modes of the asymmetrically loaded deep beams. The established model for asymmetrically loaded deep beams was found to be a general form, which includes the special cases of single-point and two-equal-point symmetric loading conditions. The geometry of STM was dependent on the configuration of asymmetrical loadings, i.e. Load Inequality (LI) and Load Asymmetry (LA). The model was evaluated by eight specimens tested by the author and six by Leong (2001), with LI ranging from 1 to 6 and LA from 1 to 4. The STM was a reasonable representation of the beam stress trajectory at the ultimate stage backed by the beam crack patterns. The model predictions for ultimate beam strengths were in good agreement with test results. Moreover, the beam failure modes were also correctly predicted by the STM. The prediction accuracy and consistency of the STM were comparable to FEM results.

An experimental programme consisting of 14 SSDBs is conducted to investigate the effects of unequal and unsymmetrical loadings on the strength and behaviour of SSDBs. LI and LA both significantly influenced the cracking behaviour and patterns of deep beams. LI reduced the ultimate total load and beam stiffness, whereas LA enhanced the ultimate total load and beam stiffness. Generally, concrete strains along diagonal strut within the failure shear span reached or nearly reached the peak concrete compressive strain. Concrete strains outside the confines of the diagonal strut were significantly smaller, giving strong support of the strut profile of proposed STM. An interactive relationship was found between tension and compression actions within the failure shear span.

Finally, this thesis investigated the size effect in deep beams. An experimental programme consisting of eleven specimens was carried out. Beam width was found to have negligible influence on shear strength for slender deep beams with h/b ratio up to 12.5. Unintended out-of-plane actions were shown to have minimal effect on shear strengths, under a properly-controlled testing environment. Flexural cracking strengths of deep beams exhibited some degree of "size effect". However, at the ultimate state, arch action rather than flexure dominated the deep beam behaviour. No substantial difference was seen in the propagation rate of diagonal cracks among beams of different sizes, indicating insignificant size effect in arch actions. Thus, the so-called "size effect" in flexure had little effect on shear strength of deep beams. The factors that influenced the ultimate strength of a compression member governed the size effect, i.e. strut geometry and boundary condition.

By properly configuring the dimensions of loading and support plates, size effect in ultimate shear strength was significantly mitigated, even for beams with higher h/b ratios and plain concrete web. It suggested that properly configured strut geometry played a dominant role in mitigating size effect. Evenly distributed web reinforcement was also shown to be an important role in mitigating size effect in deep beams. The author incorporated the modified STM with the causes of size effect, i.e. strut geometry and strut boundary conditions. The incorporated STM yielded good agreement to the test results.

6.2 Recommendations for future work

In this study, a modified strut-and-tie model was proposed and validated by SSDBs subjected to symmetrical and unsymmetrical loadings, CDBs with rigid and spring supports. The modified model was then further used to examine size effects in deep beams with success. The model gave promising results in predicting the failure modes of deep beams for the first time. The simplicity in the model implementation makes it a promising and useful tool for engineers.

However, all the applications of STM in this thesis are RC deep beams under ambient temperature. It would be interesting to explore the applicability of the STM for RC deep beams at elevated temperatures. Material strengths of both concrete and steel will be weakened under elevated temperatures, especially for the steel reinforcement. It needs to be further examined if the interactive relationship between tensile and compressive stresses at nodal zones in the model still remains valid under fire conditions. It is also possible that the failure criterion requires some adjustment for applications in fire. Some experimental programme can be carefully devised to further investigate the required parameters and validate the STM. Extra care should be taken to avoid excessive spalling of concrete under high temperatures. Providing meshing steels near the concrete surface may be useful. Finite element analysis of RC members under elevated temperature could also be carried out to supplement the study so that higher confidence could be secured in the strut-and-tie modelling under elevated temperatures. The application of STM under fire conditions would be a significant step forward and could provide engineers with powerful and efficient tools for designing RC members against fire.

Up to now, research works of strut-and-tie methods are mainly aimed at applications for RC structural members. Whether this powerful and efficient tool can be applied to concrete members externally strengthened with Fibre Reinforced Polymer (FRP) strips remains a question. However, the characteristics of the FRP strip make it ideal for simplification as a tension tie in the strut-and-tie model. The author thinks that this is a worthwhile area to be explored. The failure mechanism of FRP slip and fracture should be carefully studied. A strut-and-tie model incorporating the FRP failure mode can be developed and verified with available test results. An experimental programme is to be conducted. In this programme, a number of RC deep beams with nominal distributing web reinforcement are to be tested to failure with different FRP strip configuration. It would be interesting to investigate how the load path of the member could be changed by introducing external FRP strips. The behaviour of SSDBs strengthened with FRP strips under equal or unequal loadings can be investigated and the applicability of strut-and-tie model will be examined. FEM analysis can also be implemented in this study.

REFERENCES

ACI Committee 318. (1999). Building code requirements for structural concrete (ACI 318-99) and commentary (ACI 318R-99), American Concrete Institute, Farmington Hills, Mich.

ACI Committee 318. (2002). Building code requirements for structural concrete (ACI 318-02) and commentary (ACI 318R-02), American Concrete Institute, Farmington Hills, Mich.

ACI Committee 318. (2005). Building code requirements for structural concrete (ACI 318-05) and commentary (ACI 318R-05), American Concrete Institute, Farmington Hills (MI), 391.

ASCE-ACI Committee 445 (1973). "The shear strength of reinforced concrete members", Journal of Structural Engineering, ASCE, 99, No. 6, pp 1091-1187.

Alshegeir, A. (1992). "Analysis and design of disturbed regions with strut-tie models", PhD thesis, Purdue University, West Lafayette, Ind.

Ashour, A. F. (1997). "Tests of reinforced concrete continuous deep beams", ACI Structural Journal, 94, No. 1, pp 3-12.

An, X., Maekawa, K., and Okamura, H. (1997). "Numerical simulation of size effect in shear strength of RC beams", Journal of Materials, Concrete Structures and Pavement, JSCE, 35, No. 564, pp 297-316.

ASCE-ACI Committee 445 (1998). "Recent approaches to shear design of structural concrete", Journal of Structural Engineering, ASCE, 124, No. 12, pp 1375-1417.

Asin, M. (1999). The behaviour of reinforced concrete continuous deep beams., Delft University Press, Delft.

Ashour, A. F. (2000). "Shear Capacity of Reinforced Concrete Deep Beams", Journal of Structural Engineering, ASCE, 126, No. 9, pp 1045-1052.

Bazant, Z. P., and Kim, J.-K. (1984). "Size effect in shear failure of longitudinally reinforced beams", ACI Journal, 81, No. 5, pp 456-468.

Bazant, Z. P., and Hsu-Huei, S. (1987). "Size effect in diagonal shear failure: influence of aggregate size and stirrups", ACI Materials Journal, 84, No. 4, pp 259-272.

Bazant, Z. P., and Kazemi, M. T. (1991). "Size effect on diagonal shear failure of beams without stirrups", ACI Structural Journal, 88, No. 3, pp 268-276.

Bergmeister, K., Breen, J. E., and Jirsa, J. O. (1991). "Dimensioning of the Nodes and Development of Reinforcement" report IABSE colloquium on structural concrete, Stuttgart, pp 551-556.

Belarbi, A., and Hsu, T. T. C. (1994). "Constitutive laws of concrete in tension and reinforcing bars stiffened by concrete", ACI Structural Journal, 91, No. 4, pp 465-474.

Belarbi, A., and Hsu, T. T. C. (1995). "Constitutive laws of softened concrete in biaxial tension-compression", ACI Structural Journal, 92, No. 5, pp 562-573.

Canadian Standards Association. (1984). Design of concrete structures: Structures design. Canadian Standards Association, Rexdale (ON).

Chemrouk, M. (1988). "Slender concrete deep beams: behaviour, serviceability and strength", PhD Thesis, The University of Newcastle upon Tyne, Newcastle.

Collins, M. P., and Mitchell, D. (1991). Prestressed Concrete Structures, Prentice Hall College Div., Toronto and Montreal, Canada.

CEB-FIP model code 1990. (1993). Design code, Thomas Telford Ltd., London.

Choo, Q. L., and Lim, H. L. (1993). "Design and beaviour of continuous concrete deep beams." BEng. Final year project report, Nanyang Technological University, Singapore.

Canadian Standards Association. (1994). Design of concrete structures: Structures design. Canadian Standards Association, Rexdale (ON).

Collins, M. P., and Kuchma, D. (1999). "How safe are our large, lightly reinforced concrete beams, slabs, and footings", ACI Structural Journal, 96, No. 4, pp 482-490.

Fields, K. L. (1998). "Tension Stiffening Response of High-Strength Reinforced Concrete Tensile Members", MSC Thesis, The University of New Brunswick, German.

Foster, S. J., and Gilbert, R. I. (1998). "Experimental studies on high-strength concrete deep beams." ACI Structural Journal, 95, No. 4, pp 382-390.

Foster, S. J., and Malik, A. R. (2002). "Evaluation of Efficiency Factor Models used in Strut-and-Tie Modeling of Nonflexural Members", Journal of Structural Engineering, ASCE., 128, No. 5, pp 569-577.

Hwang, S. J., Lu, W. Y., and Lee, H. J. (2000). "Shear strength prediction for deep beams", ACI Structural Journal, 97, No. 3, pp 367-376.

Kani, G. N. J. (1967). "How safe are our large reinforced concrete beams", ACI Journal, 64, No. 3, pp 128-141.

Kong, F. K., Robins, P. J., Kirby, D. P., and Short, D. R. (1972). "Deep beams with inclined web reinforcement", ACI Journal, 69, No. 3, pp 172-176.

Kotsovos, M. D. (1983). "Mechanisms of 'shear' failure." Magazine of Concrete Research, 35, No 123, pp 99-106.

Kong, F. K., Garcia, R. C., Paine, J. M., Wong, H. H. A., Tang, C. W. J., and Chemrouk, M. (1986). "Strength and stability of slender concrete deep beams", The Structural Engineer, 64, No. 15, pp 49-56.

Kotsovos, M. D. (1988). "Compressive force path concept: basis for reinforced concrete ultimate limit state design." ACI Structural Journal, 85, No. 1, pp 68-75.

Kong, F. K. (1990). Reinforced Concrete Deep Beams, Van Nostrand Reinhold, New York.

Kotsovos, M. D., and Pavlovic, M. N. (1994). "A possible explanation for size effects in structural concrete", Archives of Civil Engineering, 40, No. 2, pp 243-261.

Kotsovos, M. D., and Pavlovic, M. N. (1997). "Size effects in structural concrete: a numerical experiment", Computers and Structures, 64, No. 1-4, pp 285-295.

Kotsovos, M. D., and Pavlovic, M. N. (2004). "Size effects in beams with small shear span-to-depth ratios", Computers & Structures, 82, No. 2-3, pp 143-56.

Kupfer, H. B. and Gerstle, K. H. (1973). “Behavior of concrete under biaxial stresses”, ASCE Journal of the Engineering Mechanics Division, 99, No. 4, pp 853-866.

Leonhardt, F., and Walther, R. "Deep beams" Deutscher Ausschuss Fur Stahlbeton Bulletin, 178, 1966, Wilhelm Ernst and Sohn (Berlin), pp CIRIA English Translation, Jan. 1970.

Leong, C. L. (2001). "Shear strength predictions of deep beams using FEM, strut-and-tie and design equations", MEng Thesis, Nanyang Technological University, Singapore.

Lertsrisakulrat, T., Watanabe, K., Matsuo, M., and Niwa, J. (2001). "Experimental study on parameters in localization of concrete subjected to compression", Journal of Materials, Concrete Structures and Pavements, JSCE, 50, No. 669, pp 309-321.

Mörsch, E. (1909). Concrete-Steel Construction (English translation by E. P. Goodrich from third [1998] edition of Der Eisenbetonbau), The Engineering News Publishing Company, New York, NY.

Marti, P. (1985). "Basic tools of reinforced concrete beam design." ACI Journal, 82, No. 1, pp 46-56.

MacGregor, J. G. (1988). Reinforced concrete: mechanics and design, Prentice Hall, New Jersey.

Mau, S. T., and Hsu, T. T. C. (1989). "Formula for the shear strength of deep beams", ACI Structural Journal, 86, No. 5, pp 516-523.

Maimba, P. P. (1989). "Effects of support continuity on the behaviour of slender reinforced concrete deep beams", MEng Thesis, The University of Newcastle upon Tyne, Newcastle.

Maekawa, K., Pimanmas, A., and Okamura, H. (2003). Nonlinear mechanics of reinforced concrete, Spon Press, New York.

Nielsen, M. P., Braestrup, M. W., Jensen, B. C., and Bach, F. (1978), Concrete plasticity, beam shear in joints–punching shear, Special publication, Danish Society for Structural Science and Engineering, Technical Univ. of Denmark, Lyngby, 129.

Ove Arup & Partners (1977). The Design of Deep Beams in Reinforced Concrete, Constructional Industry Research and Information Association, CIRIA Guide 2, London.

Oh, J.-K., and Shin, S.-W. (2001). "Shear strength of reinforced high-strength concrete deep beams." ACI Structural Journal,, 98, No. 2, pp 164-173.

Poh, S. P. (1995). "Strength and serviceability of prestressed concrete deep beams", MEng. Thesis, Nanyang Technological University, Singapore.

Reinhardt, H. W. (1981) "Similitude of brittle fracture of structural concrete" Advanced Mechanics of Reinforced Concrete, IABSE Colloquium, Delft, pp 175-184.

Rogowsky, D. M., MacGregor, J. G., and Ong, S. Y. (1986). "Tests of reinforced concrete deep beams." ACI Journal, 83, No. 4, pp 614-623.

Rios, R. D., and Riera, J. D. (2004). "Size effects in the analysis of reinforced concrete structures", Engineering Structures, 26, No. 8, pp 1115-1125.

Russo, G., Somma, G., and Mitri, D. (2005). "Shear Strength Analysis and Prediction for Reinforced Concrete Beams without Stirrups", Journal of Structural Engineering, ASCE, 131, No. 1, pp 66-74.

Smith, K. N., and Vantsiotis, A. S. (1982). "Shear strength of deep beams." ACI Journal, 79, No. 3, pp 201-213.

Subedi, N. K., Vardy, A. E., and Kubota, N. (1986). "Reinforced concrete deep beams - some test results." Magazine of Concrete Research, 38, No. 137, pp 206-219.

Schlaich, J., Schaefer, K., and Jennewein, M. (1987). "Toward a consistent design of structural concrete." PCI J., 32, No. 3, pp 74-150.

Subedi, N. K. (1988). "Reinforced concrete deep beams: a method of analysis." Proceedings of ICE Journal, 85, No. 2, pp 1-30.

Subedi, N. K. (1998). "Reinforced concrete two-span continuous deep beams", Proc. Instn Civ. Engrs Structs & Bldgs, 128, No. 1, pp 12-25.

Shin, S.-W., Lee, K.-S., Moon, J.-I., and Ghosh, S. K. (1999). "Shear strength of reinforced high-strength concrete beams with shear span-to-depth ratios between 1.5 and 2.5", ACI Structural Journal, 96, No. 4, pp 549-556.

Soltani, M., An, X., and Maekawa, K. (2005). "Localized nonlinearity and size-dependent mechanics of in-plane RC element in shear", Engineering Structures, 27, No. 6, pp 891-908.

Tan, K. H., Kong, F. K., Teng, S., and Guan, L. (1995). "High-strength concrete deep beams with effective span and shear span variations." ACI Structural Journal, 92, No. 4, pp 395-405.

Tan, K. H., Kong, F. K., Teng, S., and Weng, L. W. (1997a). "Effect of web reinforcement on high-strength concrete deep beams." ACI Structural Journal, 94, No. 5, pp 572-582.

Tan, K. H., Teng, S., Kong, F. K., and Lu, H. Y. (1997b). "Main tension steel in high strength concrete deep and short beams." ACI Structural Journal, 94, No. 6, pp 752-768.

Tan, K. H., Weng, L. W., and Teng, S. (1997c). "Strut-and-tie model for deep beams subjected to combined top-and-bottom loading", Structural Engineer, 75, No. 13, pp 215-221.

Tan, K. H., and Lu, H. Y. (1999). "Shear behavior of large reinforced concrete deep beams and code comparisons." ACI Structural Journal, 96, No. 5, pp 836-845.

Tan, K. H., Tong, K., and Tang, C. Y. (2001). "Direct strut-and-tie model for prestressed deep beams", Journal of Structural Engineering, ASCE, 127, No. 9, pp 1076-1084.

Tan, K. H., Tang, C. Y., and Tong, K. (2003a). "A direct method for deep beams with web reinforcement", Magazine of Concrete Research, 55, No. 1, pp 53-63.

Tan, K. H., Tong, K., and Tang, C. Y. (2003b). "Consistent strut-and-tie modelling of deep beams with web openings", Magazine of Concrete Research, 55, No. 1, pp 65-75.

Tan, K. H., Cheng, G. H., and Cheong, H. K. (2005). "Size effect in shear strength of large beams -behaviour and finite element modelling", Magazine of Concrete Research, 57, No. 8, pp 497-509.

Tan, K. H., and Cheng, G. H. (2006). "Size effect on shear strength of deep beams: Investigating with strut-and-tie model", Journal of Structural Engineering, 132, No. 5, pp 673-685.

Tan, K. H., Cheng, G. H., and Zhang, N. (2008). "Experiment to mitigate size effect on deep beams", Magazine of Concrete Research, 60, No. 10, pp 709-723.

Tang, C. Y., and Tan, K. H. (2004). "Interactive Mechanical Model for Shear Strength of Deep Beams", Journal of Structural Engineering, ASCE, 130, No. 10, pp 1534-1544.

Tsuchiya, S., Mishima, T., and Maekawa, K. (2002). "Shear Failure and Numerical Performance Evaluation for RC Beam Members Made with High-Strength Materials", Concrete Library International, 40, No., pp 227-252.

Vecchio, F. J., and Collins, M. P. (1986). "The modified compression-field theory for reinforced concrete elements subjected to shear." ACI Journal, 83, No. 2, pp 219-231.

Vecchio, F. J., and Collins, M. P. (1993). "Compression Response of Cracked Reinforced Concrete", Journal of Structural Engineer, ASCE, 119, No. 12, pp 3590-3610.

Walraven, J. C. (1978). "Influence of member depth on the shear strength of lightweight concrete beams without shear reinforcement" Stevin Laboratory Report No. 5-78-4, Delft University of Technology.

Walraven, J., and Lehwalter, N. (1994). "Size effects in short beams loaded in shear", ACI Structural Journal, 91, No. 5, pp 585-593.

Yang, K.-H., Chung, H.-S., Lee, E.-T., and Eun, H.-C. (2003). "Shear characteristics of high-strength concrete deep beams without shear reinforcements", Engineering Structures, 25, No. 10, pp 1343-1352.

Appendix A: Member Forces of STM for CDBs on Rigid Supports

The stress-strain relationship of concrete under compression is taken as linear:

$$\sigma_\mathrm{c} = E_\mathrm{c}\varepsilon_\mathrm{c}$$

where E_c is the modulus of elasticity of concrete in compression and is taken from ACI code ($E_c = 4730\sqrt{f_c'}$, MPa) for normal strength concrete.

The stress-strain relationship of steel in tension is given by:

$$\sigma_\mathrm{s} = E_s\varepsilon_\mathrm{s}$$

The truss members in **Figure 2.8** are internally determinate but externally indeterminate to 1 degree. Releasing the interior reaction force X and applying Crotti-Engesser theorem, the total complementary energy in the truss is:

$$U_\mathrm{c} = \sum\int_V\left(\int \varepsilon \,\mathrm{d}\sigma\right)\mathrm{d}V$$

$$= \frac{\dfrac{\left(P-\dfrac{X}{2}\right)^2 l_\mathrm{e}}{2\sin^2\theta_s\cos\theta_s}}{E_\mathrm{c}A_\mathrm{str4}} + \frac{\dfrac{X^2 l_\mathrm{e}}{8\sin^2\theta_s\cos\theta_s}}{E_\mathrm{c}A_\mathrm{str5}} + \frac{\dfrac{(X-P)^2 l_\mathrm{e}}{2\tan^2\theta_s}}{E_\mathrm{s}A_\mathrm{s1}} + \frac{\dfrac{\left(P-\dfrac{X}{2}\right)^2 l_\mathrm{e}}{\tan^2\theta_s}}{E_\mathrm{s}A_\mathrm{s2}} \quad \text{(A.1)}$$

where l_e is the effective span measured between centres of supports; θ_s is the inclined angle of diagonal strut; E_c and E_s are the elastic modulus of concrete under compression and steel bar under tension, respectively. The terms A_str1, A_str2 and A_str3 are the cross-sectional areas at the ends of the tapered concrete struts (**Figure 2.9**), while A_str4 and A_str5 represent the average cross-sectional areas of the exterior and interior tapered concrete struts, respectively (**Figure 2.8**). They are expressed as follows:

$$A_\mathrm{str1} = b_\mathrm{w}\left(l_\mathrm{c}\cos\theta_s + l_\mathrm{b}\sin\theta_s\right) \quad \text{(A.2)}$$

$$A_\mathrm{str2} = b_\mathrm{w}\left(l_\mathrm{c}\cos\theta_s + l_\mathrm{f}\sin\theta_s\right) \quad \text{(A.3)}$$

$$A_{\mathrm{str3}} = b_{\mathrm{w}}\left(l_{\mathrm{d}}\cos\theta_s + l_{\mathrm{a}}\sin\theta_s\right) \tag{A.4}$$

$$A_{\mathrm{str4}} = \frac{A_{\mathrm{str1}} + A_{\mathrm{str3}}}{2} \tag{A.5}$$

$$A_{\mathrm{str5}} = \frac{A_{\mathrm{str2}} + A_{\mathrm{str3}}}{2} \tag{A.6}$$

$$\theta_s = \arctan\frac{2(h - c_1 - c_2)}{l_{\mathrm{e}}} \tag{A.7}$$

where

l_{a}, l_{b} and l_{f} are the widths of the support and load bearing plates (**Figure 2.7**);

l_{c} and l_{d} are the respective effective depths of the bottom and top nodal zones, $l_{\mathrm{c}}=2c_2$, $l_{\mathrm{d}}=2c_1$ (**Figure 2.9**);

c_1 and c_2 are the distances from the centroid of the top and bottom longitudinal steel bars to the beam top and beam soffit, respectively (**Figure 2.7**).

From the Theorem of Minimum Complementary Potential (TMCP), at the middle support B:

$$\Delta_{\mathrm{B}} = \frac{\partial U_{\mathrm{c}}}{\partial X} = 0 \tag{A.8}$$

Thus, from Eqs. (A.1) and (A.8), an expression for the reaction force X is obtained as follows:

$$X = \frac{2(m + 2n\cos^3\theta_s + 2p\cos^3\theta_s)}{1 + m + 4n\cos^3\theta_s + 2p\cos^3\theta_s}P \quad (\uparrow) \tag{A.9}$$

where m, n, p are the ratios of axial stiffness of truss members:

$$m = \frac{A_{\mathrm{str5}}}{A_{\mathrm{str4}}}; \tag{A.10}$$

$$n = \frac{E_{\mathrm{c}}A_{\mathrm{str5}}}{E_{\mathrm{s}}A_{\mathrm{s1}}}; \tag{A.11}$$

$$p = \frac{E_c A_{\mathrm{str5}}}{E_s A_{\mathrm{s2}}}; \qquad \text{(A.12)}$$

After solving the reaction force *X*, the internal forces of truss members (**Figure 2.8**) is obtained as follows:

$$F_{c1} = \frac{1 + 2n\cos^3\theta_s}{\sin\theta_s(1 + m + 4n\cos^3\theta_s + 2p\cos^3\theta_s)} P \quad \text{(compression)} \qquad \text{(A.13)}$$
$$= A \cdot P$$

$$T_1 = \frac{\cos\theta_s(m + 2p\cos^3\theta_s - 1)}{\sin\theta_s(1 + m + 4n\cos^3\theta_s + 2p\cos^3\theta_s)} P \quad \text{(tension)} \qquad \text{(A.14)}$$
$$= B \cdot P$$

$$T_2 = \frac{\cos\theta_s(1 + 2n\cos^3\theta_s)}{\sin\theta_s(1 + m + 4n\cos^3\theta_s + 2p\cos^3\theta_s)} P \quad \text{(tension)} \qquad \text{(A.15)}$$
$$= C \cdot P$$

$$F_{c2} = \frac{m + 2n\cos^3\theta_s + 2p\cos^3\theta_s}{\sin\theta_s(1 + m + 4n\cos^3\theta_s + 2p\cos^3\theta_s)} P \quad \text{(compression)} \qquad \text{(A.16)}$$
$$= D \cdot P$$

Appendix B: Worked Example on CDB on Rigid Supports

The notation of the beam is BM 5/1.0 (Rogowsky et al., 1986), details of specimens are as follows:

Geometry: $l_e = 2100$ mm, c_1=50 mm, c_2=25 mm, l_c=50 mm, l_d=100 mm, h = 1000 mm, b_w = 200 mm, l_b = 200 mm, l_a= 300 mm, l_f= 400 mm, A_c= 185000 mm^2;

Concrete strength: f_c' = 36.9 N/mm^2, E_c= $3694\sqrt{f_c'}$ = 22439 MPa, f_{sp}= $0.461\sqrt{f_c'}$ = 2.80 MPa;

Longitudinal reinforcement: A_{s1}= 1195 mm^2, A_{s2}= 896 mm^2, f_yA_{s1}= 484 kN, f_yA_{s2}= 363 kN;

Vertical web reinforcement: $A_{sv}f_{yv}$ = 518 kN, θ_w=90°.

Step 1 Determine θ_s from Eqs. (A.7);

$$\theta_s = \arctan\frac{2\left(h-c_1-c_2\right)}{l_e} = \arctan\frac{2\times(1000-50-25)}{2100} = 41.4°$$

Step 2 Determine *m, n, p,* from Eqs. (A.10)~(A.12);

$$A_{str1} = b_w\left(l_c\cos\theta_s + l_b\sin\theta_s\right) = 200\times(50\times0.750+200\times0.661) = 33945\text{ mm}^2$$

$$A_{str2} = b_w\left(l_c\cos\theta_s + l_f\sin\theta_s\right) = 200\times(50\times0.750+400\times0.661) = 60386\text{ mm}^2$$

$$A_{str3} = b_w\left(l_d\cos\theta_s + l_a\sin\theta_s\right) = 200\times(100\times0.750+300\times0.661) = 54669\text{ mm}^2$$

$$A_{str4} = \frac{A_{str1}+A_{str3}}{2} = \frac{33945+54669}{2} = 44307\text{ mm}^2$$

$$A_{str5} = \frac{A_{str2}+A_{str3}}{2} = \frac{60386+54669}{2} = 57528\text{ mm}^2$$

$$m = \frac{A_{str5}}{A_{str4}} = \frac{57528}{44307} = 1.298$$

$$n = \frac{E_cA_{str5}}{E_sA_{s1}} = \frac{22439\times57528}{200000\times1195} = 5.401$$

$$p = \frac{E_{\mathrm{c}} A_{\mathrm{str5}}}{E_{\mathrm{s}} A_{\mathrm{s2}}} = \frac{22439 \times 57528}{200000 \times 896} = 7.204$$

Step 3 Determine *A, B, C, D* from Eqs. (A.13)~(A.16);

$$A = \frac{1 + 2n\cos^3\theta_{\mathrm{s}}}{\sin\theta_{\mathrm{s}}(1 + m + 4n\cos^3\theta_{\mathrm{s}} + 2p\cos^3\theta_{\mathrm{s}})}$$

$$= \frac{1 + 2 \times 5.401 \times 0.422}{0.661 \times (1 + 1.298 + 4 \times 5.401 \times 0.422 + 2 \times 7.204 \times 0.422)} = 0.481$$

$$B = \frac{\cos\theta_s(m + 2p\cos^3\theta_s - 1)}{\sin\theta_s(1 + m + 4n\cos^3\theta_s + 2p\cos^3\theta_s)}$$

$$= \frac{0.750 \times (1.298 + 2 \times 7.204 \times 0.422 - 1)}{0.661 \times (1 + 1.298 + 4 \times 5.401 \times 0.422 + 2 \times 7.204 \times 0.422)} = 0.414$$

$$C = \frac{\cos\theta_s(1 + 2n\cos^3\theta_s)}{\sin\theta_s(1 + m + 4n\cos^3\theta_s + 2p\cos^3\theta_s)}$$

$$= \frac{0.750 \times (1 + 2 \times 5.401 \times 0.422)}{0.661 \times (1 + 1.298 + 4 \times 5.401 \times 0.422 + 2 \times 7.204 \times 0.422)} = 0.360$$

$$D = \frac{m + 2n\cos^3\theta_s + 2p\cos^3\theta_s}{\sin\theta_s(1 + m + 4n\cos^3\theta_s + 2p\cos^3\theta_s)}$$

$$= \frac{1.298 + 2 \times 5.401 \times 0.422 + 2 \times 7.204 \times 0.422}{0.661 \times (1 + 1.298 + 4 \times 5.401 \times 0.422 + 2 \times 7.204 \times 0.422)} = 1.032$$

Step 4 Determine P_{nA}, P_{nB}, and P_{nC} from Eqs. (2.28), (2.31), and (2.34), respectively;

$$f_{\mathrm{ct}} = 0.31\sqrt{f_{\mathrm{c}}'}\left(\frac{\varepsilon_{\mathrm{cr}}}{\varepsilon_1}\right)^{0.4}$$

$$= 0.31 \times \sqrt{36.9} \times \left(\frac{0.00008}{0.002 + 0.004 / \tan^2 41.38^\circ}\right)^{0.4} = 0.31 \text{ MPa}$$

$$T_{1\max} = f_{\mathrm{y}} A_{\mathrm{s1}} = 484 \text{ kN}$$

$$T_{2\max} = f_{\mathrm{y}} A_{\mathrm{s2}} = 363 \text{ kN}$$

$$T_{1\mathrm{a}} = \min(f_{\mathrm{y}} A_{\mathrm{s1}}, \frac{B}{C} T_{2\max}) = 416 \text{ kN}$$

$$T_{2\mathrm{a}} = \min(f_{\mathrm{y}} A_{\mathrm{s2}}, \frac{C}{B} T_{1\max}) = 363 \text{ kN}$$

Nodal zone A:

$$
\begin{aligned}
f_{\mathrm{tA}} &= \frac{4T_{2\max}}{A_{\mathrm{c}}/\sin^2\theta_s} + \frac{A_{\mathrm{sv}} f_{\mathrm{yv}} \sin 2\theta_s}{2A_{\mathrm{c}}} + f_{\mathrm{ct}} \\
&= \frac{4\times 363\times 0.437\times 10^3}{185000} + \frac{518\times 0.992\times 10^3}{2\times 185000} + 0.31 \\
&= 3.43 + 1.39 + 0.31 = 5.13 \text{ MPa}
\end{aligned}
$$

$$
\begin{aligned}
P_{\mathrm{nA}} &= \cfrac{1}{\cfrac{4C\sin^2\theta_s}{f_{\mathrm{tA}} A_{\mathrm{c}}} + \cfrac{(A - C\cos\theta_s)}{f_{\mathrm{c}}' A_{\mathrm{str1}}}} \\
&= \cfrac{1/1000}{\cfrac{4\times 0.360\times 0.437}{5.13\times 185000} + \cfrac{0.481 - 0.360\times 0.750}{36.9\times 33945}} = 1202 \text{ kN}
\end{aligned}
$$

Nodal zone B:

$$
\begin{aligned}
f_{\mathrm{tB}} &= \frac{4T_{2\max} - 2T_{1\mathrm{a}}}{A_{\mathrm{c}}/\sin^2\theta_s} + \frac{A_{\mathrm{sv}} f_{\mathrm{yv}} \sin 2\theta_s}{2A_{\mathrm{c}}} + f_{\mathrm{ct}} \\
&= \frac{\left(4\times 363 - 2\times 416\right)\times 10^3}{185000/0.437} + \frac{518\times 0.992\times 10^3}{2\times 185000} + 0.31 \\
&= 1.46 + 1.39 + 0.31 = 3.16 \text{ MPa}
\end{aligned}
$$

$$
\begin{aligned}
P_{\mathrm{nB}} &= \cfrac{1}{\cfrac{4C - 2B}{f_{\mathrm{tB}} A_{\mathrm{c}}/\sin^2\theta_s} + \cfrac{(D - C\cos\theta_s)}{f_{\mathrm{c}}' A_{\mathrm{str2}}}} \\
&= \cfrac{1/1000}{\cfrac{4\times 0.360 - 2\times 0.414}{3.16\times 185000/0.437} + \cfrac{1.032 - 0.360\times 0.750}{36.9\times 60386}} = 1251 \text{ kN}
\end{aligned}
$$

Nodal zone C:

$$
\begin{aligned}
f_{\mathrm{tC}} &= \frac{4T_{1\max} - 2T_{2\mathrm{a}}}{A_{\mathrm{c}}/\sin^2\theta_s} + \frac{A_{\mathrm{sv}} f_{\mathrm{yv}} \sin 2\theta_s}{2A_{\mathrm{c}}} + f_{\mathrm{ct}} \\
&= \frac{\left(4\times 484 - 2\times 363\right)\times 10^3}{185000/0.437} + \frac{518\times 0.992\times 10^3}{2\times 185000} + 0.31 \\
&= 2.86 + 1.39 + 0.31 = 4.56 \text{ MPa}
\end{aligned}
$$

$$P_{\mathrm{nC}} = \frac{1}{\dfrac{4B-2C}{f_{\mathrm{tC}} A_{\mathrm{c}} / \sin^2\theta_s} + \dfrac{D - B\cos\theta_s}{f_{\mathrm{c}}' A_{\mathrm{str3}}}}$$

$$= \frac{1/1000}{\dfrac{4\times 0.414 - 2\times 0.360}{4.56\times 185000/0.437} + \dfrac{1.032 - 0.414\times 0.750}{36.9\times 54669}} = 1187\ \mathrm{kN}$$

Step 5 Determine the ultimate load P_{n} from Eq. (2.35).

$$\therefore P_{\mathrm{n}} = \mathrm{Min}(P_{\mathrm{nA}}, P_{\mathrm{nB}}, P_{\mathrm{nC}}) = 1187\ \mathrm{kN}$$

Thus the predicted ultimate load of P_{n} is 1187 kN. Total ultimate load is $2P_{\mathrm{n}}$=2374 kN. In this example, the ultimate load $2P_{\mathrm{exp}}$ from experiment was 2559 kN (T1). Thus, the ratio of $P_{\mathrm{n}}/P_{\mathrm{exp}}$ is 0.93.

Appendix C: Middle Support Reaction of STM for CDBs on Spring Supports

The truss members in **Figure 2.13** are internally determinate but externally indeterminate to 1 degree. Releasing the middle support force X and applying Crotti-Engesser theorem, the total complementary energy in the truss is:

$$U_{\mathrm{c}} = \sum \int_V \left(\int \varepsilon \mathrm{d}\sigma \right) \mathrm{d}V$$

$$= \frac{\dfrac{\left(P - \dfrac{X}{2}\right)^2 l_e}{2\sin^2\theta_s \cos\theta_s}}{\mathrm{E}_c A_{str4}} + \frac{\dfrac{X^2 l_e}{8\sin^2\theta_s \cos\theta_s}}{\mathrm{E}_c A_{str5}} + \frac{\dfrac{(X-P)^2 l_e}{2\tan^2\theta_s}}{\mathrm{E}_s A_{s1}} + \frac{\dfrac{\left(P - \dfrac{X}{2}\right)^2 l_e}{\tan^2\theta_s}}{\mathrm{E}_s A_{s2}} + \frac{X^2}{2K} \qquad \text{(C.1)}$$

where the term X is the reaction force of the middle support B; l_{e} is the effective span measured between centres of supports; θ_s is the inclined angle of diagonal strut; E_{c} and E_{s} are the elastic modulus of concrete under compression and steel bar under tension, respectively. The terms A_{str1}, A_{str2} and A_{str3} are the cross-sectional areas at the ends of the tapered concrete struts (**Figure 2.12**), while A_{str4} and A_{str5} represent the average cross-sectional areas of the exterior and interior tapered diagonal struts, respectively (**Figure 2.13**). They are defined in Appendix A.

From the Theorem of Minimum Complementary Potential:

$$\Delta_B = \frac{\partial U_c}{\partial X} = 0 \qquad \text{(C.2)}$$

From Eqs. (C.1) and (C.2), the expression for X is obtained as follows:

$$X = \Gamma \cdot P = \frac{2(m + 2n\cos^3\theta_s + 2p\cos^3\theta_s)}{1 + m + 4n\cos^3\theta_s + 2p\cos^3\theta_s + 2\xi\sin^2\theta_s} \cdot P \quad (\uparrow) \qquad \text{(C.3)}$$

where m, n, p are the ratios of axial stiffness of truss members:

$$m = \frac{A_{\mathrm{str5}}}{A_{\mathrm{str4}}} \tag{C.4}$$

$$n = \frac{E_{\mathrm{c}} A_{\mathrm{str5}}}{E_{\mathrm{s}} A_{\mathrm{s1}}} \tag{C.5}$$

$$p = \frac{E_{\mathrm{c}} A_{\mathrm{str5}}}{E_{\mathrm{s}} A_{\mathrm{s2}}} \tag{C.6}$$

and ξ is the stiffness ratio between interior diagonal strut and the support spring:

$$\xi = \frac{2E_{\mathrm{c}} A_{\mathrm{str5}} \cos\theta_s}{Kl_e} \tag{C.7}$$

For perfectly rigid support, $\xi = 0$. Thus the reaction force X (Eq. (C.3)) is reduced to Eq. (A.9) in Appendix A.

Appendix D: Top Strut Inclination Angle θ in STM for SSDBs under Asymmetrical Loads

From geometry (**Figure 2.15**), the inclination angle of top strut θ, left diagonal strut α and right diagonal strut β are expressed as below:

$$\tan\theta = \frac{\Delta}{b} \tag{D.1}$$

$$\tan\alpha = \frac{d_c}{a} \tag{D.2}$$

$$\tan\beta = \frac{d_c - \Delta}{c} \tag{D.3}$$

The term d_c is the distance from the centroid of bottom longitudinal reinforcement to the centroid of top nodal zone A (**Figure 2.14**). From force equilibrium at node C of bottom tension tie, the following relation between α and β is established:

$$\frac{\tan\alpha}{\tan\beta} = \frac{V_1}{V_2} \tag{D.4}$$

where V_1 and V_2 are the reactions of the left and right supports, respectively (**Figure 2.15**).

Substituting Eqs. (D.2) and (D.3) into Eq. (D.4), the following equation for Δ is obtained

$$\Delta = \frac{(V_1 a - V_2 c)}{V_1 a} d_c \tag{D.5}$$

From the truss static equilibrium, the support reactions is determined from

$$V_1 = \frac{(P_1 + P_2)c + P_1 b}{l_0} \tag{D.6}$$

$$V_2 = \frac{(P_1 + P_2)a + P_2 b}{l_0} \tag{D.7}$$

Substituting Eqs. (D.5), (D.6), and (D.7) into Eq. (D.1), we can define the angle of horizontal strut AB by:

$$\tan\theta = \frac{d_c}{\Pi} \tag{D.8}$$

where Π is a load parameter incorporating the essential dimensions, given by

$$\Pi = \frac{P_1 ab + (P_1 + P_2)ac}{P_1 a - P_2 c} \tag{D.9}$$

Through defining a load inequality (LI) index $n_\mathrm{L} = P_1/P_2$, and a load asymmetry (LA) index $m_\mathrm{L} = c/a$, load parameter Π is rewritten as

$$\Pi = \frac{n_\mathrm{L}}{n_\mathrm{L} - m_\mathrm{L}} l_0 - a \tag{D.10}$$

It should be noted that the value of d_c depends on the sign of Π. When $\Pi > 0$, from **Figure 2.14,** d_c is obtained as

$$d_c = h - d_1 - d_3 \tag{D.11}$$

where d_1 is the distance from beam top to the centroid of nodal zone A (**Figure 2.14**);

d_3 is the distance from beam soffit to the centroid of bottom longitudinal reinforcement (**Figure 2.14**).

However, when $\Pi < 0$, the angle θ is negative as shown in **Figure 2.15(b)**. And d_c is expressed by

$$d_c = h - d_2 - d_3 \tag{D.12}$$

where d_2 is the distance from the beam top to the centroid of nodal zone B (**Figure 2.14**). From geometry, d_1 and d_2 are expressed by the following two equations

$$d_1 = \frac{\tan\theta}{2}\left(\frac{h_e}{\sin\theta} - l_a\right) \tag{D.13}$$

$$d_2 = (b - l_a)\tan\theta + \frac{\tan\theta}{2}\left(\frac{h_e}{\sin\theta} + l_a\right) \tag{D.14}$$

where h_e is the width of the top strut;

l_a is the width of the load plate (**Figure 2.14**).

Substituting Eqs. (D.13) and (D.14) into Eqs. (D.11) and (D.12), and utilizing the geometrical relationship $l_c=h_e/\cos\theta$ (**Figure 2.14**), depending on the sign of Π, d_c is written as below:

$$d_c = \begin{cases} h - d_3 - \dfrac{l_c}{2} + \dfrac{l_a}{2}\tan\theta & (\Pi > 0) \\ \\ h - d_3 - \dfrac{l_c}{2} - \dfrac{l_a}{2}\tan\theta + b\tan\theta & (\Pi > 0) \end{cases} \tag{D.15}$$

Combining Eqs. (D.15), and (D.8), we arrive at:

$$\tan\theta = \begin{cases} \dfrac{h - d_3 - l_c/2}{\Pi - l_a/2} & (\Pi>0) \\ \\ \dfrac{h - d_3 - l_c/2}{\Pi - b + l_a/2} & (\Pi<0) \end{cases} \tag{D.16}$$

where $l_c = h_e/\cos\theta$ is regarded as the equivalent depth of the top nodal zone A (**Figure 2.14**);

Appendix E: Worked Example on SSDB under Asymmetrical Loads

To illustrate the use of proposed strut-and-tie model, the following worked example is included for engineers. Please also refer to **Figure 2.16** for detailed steps in the algorithm.

Beam 0.3/0.9/5P

Geometry: l_0 = 1800 mm, d_3 = 72.5 mm, $l_a = l_b$ = 100 mm, h = 500 mm, b_w = 150 mm, l_d = 145 mm, a = 300 mm, b = 600 mm, c =900 mm; Concrete strength: f_c' = 41.2 N/mm^2; Longitudinal reinforcement: A_s= 796.4 mm^2, f_y= 484 MPa; Vertical web reinforcement: A_w = 157.1 mm^2, f_{yw} = 328 MPa; LI: n_L = 5, LA: m_L = 3.

Step 1 Determine α and θ from Eqs. (D.2) and (D.16), assuming $l_c = l_d$;

$l_c = 2d_3 = 145$ mm ; From Eq. (D.10): $\Pi = \dfrac{5}{5-3} \times 1800 - 300 = 4200 > 0$

From Eq. (D.16): $\tan\theta = \dfrac{500 - 72.5 - 145/2}{4200 - 100/2} = 0.0855 \quad \therefore \theta = 4.89°$

From Eq. (D.15): $d_c = 500 - 72.5 - 145/2 + 100 \times 0.0855/2 = 359.3$ mm

$$\therefore\ a = \arctan\left(\frac{359.3}{300}\right) = 50.14°$$

Step 2 Determine f_t from Eq. (2.56);

$$A_c = 150 \times 359.3 = 53895 \text{ mm}^2;\ f_{cr} = 0.31\sqrt{f_c'} = 0.31 \times \sqrt{41.2} = 1.989 \text{ N/mm}^2$$

$$\varepsilon_1 = \varepsilon_s + (\varepsilon_s + \varepsilon_2)\cot^2 a = 0.0024 + 0.0044 \times \cot^2 50.14° = 0.00550$$

$$f_{ct} = f_{cr}\left(\frac{\varepsilon_{cr}}{\varepsilon_1}\right)^{0.4} = 1.989 \times \left(\frac{0.00008}{0.00550}\right)^{0.4} = 0.37 \text{ N/mm}^2$$

$$f_t = \frac{4 \times 796.4 \times 483.68 \times \sin 50.14°}{53895/\sin 50.14°} + \frac{157.1 \times 328.07 \times \cos 50.14°}{53895/\sin 50.14°} + 0.37$$

$$= 16.85 + 0.47 + 0.37 = 17.7 \text{ N/mm}^2$$

Step 3 Determine V_1 from Eq. (2.55);

$$A_{str} = 150\times\left(145\times\cos 50.14°+100\times\sin 50.14°\right) = 25454 \text{ mm}^2$$

$$V_1 = \frac{1/1000}{\dfrac{4\times\sin 50.14°\times\cos 50.14°}{53895\times 17.682}+\dfrac{\sin 50.14°}{25454\times 41.18}} = 357.5 \text{ kN}$$

Step 4: Determine l_c from Eq. (2.60), and then repeat Step 1 to 3 until satisfactory convergence is achieved;

$$l_c = \frac{357.5\times 1000}{41.2\times 150\times\tan 50.14°\times\cos^2 4.89°} = 48.7 \text{ mm}$$

Repeat Step 1 to 3 for two rounds, it finally arrives at:

$l_c = 46.1$ mm, $A_c = 61400$ mm^2 $\theta = 5.6°$, and $a = 53.8°$

$f_t = 17.1$ N/mm^2; $V_1 = 384.6$ kN

Step 5: Determine the total ultimate load F_u from Eq. (2.57);

$$F_u = \frac{(5+1)\times 1800}{5\times 600+5\times 900+900}\times 384.6 = 494.5 \text{ kN}$$

In this example, the total ultimate load F_{exp} from experiment is 589 kN (**Table 4.2**). Thus the ratio of P_n/P_{exp} is 0.84.

Step 6: Determine the failure mode from Eqs. (2.64) and (2.66).

$$\omega = \frac{4\times 41.2\times 25454\times\cos 53.8^\circ}{61400\times 17.1} = 2.36$$

$$v_t = \frac{1}{1+1/2.36} = 0.70$$

As $v_t < 0.75$, the beam is expected to fail in shear-compression mode, which conforms to experimental observation (**Table 4.3**).

PUBLICATIONS

Journal Publications

- Zhang, N. and Tan, K. H. (2007). "Direct Strut-and-tie Model for Single and Continuous Deep Beams", Engineering Structures, 29, No. 11, pp 2987-3001.
- Zhang, N. and Tan, K. H. (2007). "Size Effect in RC Deep Beams: Experimental Investigation and STM Verification", Engineering Structures, 29, No. 12, pp 3241-3254.
- Zhang, N. and Tan, K. H. (2009). "Single-Span Deep Beams Subjected To Unsymmetrical Loads", Journal of Structural Engineering, ASCE, 135, No. 3, pp 239-252.
- Tan, K. H. Cheng, G. H., and Zhang, N. (2008). “Experiment to Mitigate Size Effect in Deep Beams”. Magazine of Concrete Research, 60, No. 10, pp 709-723.
- Tang, C. Y. Tan, Kang Hai, and Zhang, N. (2006). "Closure to ‘Interactive Mechanical Model for Shear Strength of Deep Beams’ by C. Y. Tang and K. H. Tan." Journal of Structural Engineering, ASCE, 132, No. 5, pp 828-829.
- Zhang, N. and Tan, K. H (submitted). "Effects of Support Settlement on Continuous Deep Beams and STM Modeling", Engineering Structures, 2008 Manuscript.
- Zhang, N. and Tan, K. H (submitted). "Size Effect in Asymmetrically Loaded RC Deep Beams", ACI Structural Journal, 2008 Manuscript.

Conference Proceedings

- **Zhang, N.** and Tan, K. H. (2006). "Modelling Single Span and Continuous Deep Beams using Strut-and-tie Method", Proceedings of the 19th Australasian Conference on the Mechanics of Structures and Materials, Christchurch, New Zealand, pp 731-738.
- **Zhang, N.** and Tan, K. H. (2006). "Behaviour and Strut-and-tie Modelling of Asymmetrically Loaded Deep Beams", Proceedings of the 19th Australasian Conference on the Mechanics of Structures and Materials, Christchurch, New Zealand, pp 739-745.